Point-spread function engineering
for single-molecule localization microscopy in brain slices

Submitted by Lennart Groß
born in Berlin
for the degree Master of Science in Physics
at the Faculty of Physics and Astronomy
University of Würzburg

Würzburg, 03/02/2021

This thesis was conducted at the:

Chair of Biotechnology and Biophysics
Biocenter
University of Würzburg

Examining Board:

1st supervisor: Prof. Dr. Markus Sauer
2nd supervisor: Prof. Dr. Volker Christian Behr

layout edited and spelling corrected on 29/07/2022

Eidesstattliche Versicherung

Hiermit versichere ich, dass ich die vorliegende Arbeit selbstständig verfasst und keine anderen als die angegebenen Quellen und Hilfsmittel benutzt habe, alle Ausführungen, die anderen Schriften wörtlich oder sinngemäß entnommen wurden, kenntlich gemacht sind und die Arbeit in gleicher oder ähnlicher Fassung noch nicht Bestandteil einer Studien- oder Prüfungsleistung war.

Würzburg, 03. Februar 2021

Lennart Groß

Abstract

Single-molecule localization microscopy (SMLM) is the method of choice to study biological specimens on a nanoscale level. Advantages of SMLM imply its superior specificity due to targeted molecular fluorescence labeling and its enhanced tissue preservation compared to electron microscopy, while reaching similar resolution. To reveal the molecular organization of protein structures in brain tissue, SMLM moves to the forefront: Instead of investigating brain slices with a thickness of a few μm, measurements of intact neuronal assemblies (up to 100 μm in each dimension) are required. As proteins are distributed in the whole brain volume and can move along synapses in all directions, this method is promising in revealing arrangements of neuronal protein markers. However, diffraction-limited imaging still required for the localization of the fluorophores is prevented by sample-induced distortion of emission pattern due to optical aberrations in tissue slices from non-superficial planes. In particular, the sample causes wavefront dephasing, which can be described as a summation of Zernike polynomials. To recover an optimal point spread function (PSF), active shaping can be performed by the use of adaptive optics. The aim of this thesis is to establish a setup using a deformable mirror and a wavefront sensor to actively shape the PSF to correct the wavefront phases in a super-resolution microscope setup. Therefore, fluorescence-labeled proteins expressed in different anatomical regions in brain tissue will be used as experiment specimen. Resolution independent imaging depth in slices reaching tens of micrometers is aimed.

This abstract including the aim was accepted by the Faculty of Physics and Astronomy of the University of Würzburg for the preparation of this thesis (23/07/2020).

To evaluate the capabilities of the setup built during the course of this thesis, an artificial sample was created by stacking a murine hippocampal neuron cell monolayer, stained with Alexa Fluor 647 for α-tubulin, on top of a 100 μm murine brain slice. As the latter provides a highly diffusive medium between fluorophores and objective, it induces several optical aberrations, especially spherical aberration and astigmatism. By capturing wavefront as well as point-spread function from 4 μm Fluosphere™ beads with a peak excitation wavelength of 505 nm and 0.1 μm Tetraspeck™ beads with a peak excitation wavelength of 505 nm, respectively, aberrations could be reduced from 521 nm to 116 nm root mean square (rms) wavefront error. Furthermore, adaptive optics revealed Bruchpilot clusters in honeybee brain slices in the calyx of the mushroom body at imaging depths of up to 80 μm, which could not be distinguished in the uncorrected image in this work, by reducing the rms wavefront error from 587 nm to 196 nm. All in all, the the reduction of the rms wavefront error implicates a successful correction of wavefront aberrations, but is still far from participating in neurobiological imaging.

Zusammenfassung

Einzelmolekül-Lokalisationsmikroskopie ist die Methode der Wahl zur Untersuchung biologische Proben im Bereich von Nanometern. Vorteile von Einzelmolekül-Lokalisationsmikroskopie sind vor allem ihre hohe Spezifität von molekularen Farbstoffbindungen sowie die erreichte hohe Auflösung, die vergleichbar ist mit der elektronenmikroskopischen Auflösung, wobei in der Einzelmolekül-Lokalisationsmikroskopie keine Konservierung der Probe vorgenommen werden muss. Vor allem in der Untersuchung der molekulare Organisation von Proteinstrukturen konnte sich die Einzelmolekül-Lokalisationsmikroskopie bewähren. Die Verteilung von Proteinen im gesamten Gehirn, sowie ihre Eigenschaft, sich entlang neuronaler Strukturen zu bewegen, kann mithilfe der Einzelmolekül-Lokalisationsmikroskopie untersucht werden und zu einem besseren Verständnis neuronaler Prozesse beitragen. Proben induzieren optische Aberrationen: Diese Dephasierungen der Wellenfront, welche als Summe von Zernike-Polynomen beschrieben werden kann, verhindert das Erreichen der Auflösungsgrenze. Zur Wiederherstellung einer optimalen Punktspreizfunktion kann die Wellenfront mittels adaptive Optik aktiv geformt werden. Ziel dieser Arbeit ist der Aufbau eines Einzelmolekül-Lokalisationsmikroskopes mit integrierter adaptiver Optik, bestehend aus einem deformierbaren Spiegel und einem Wellenfrontsensor, um aktiv die Wellenfront zu formen und die Dephasierung zu korrigieren. Zu diesem Zweck werden fluoreszenzmarkierte Proteine, welche in verschiedenen Hirnregionen exprimiert werden, als Proben herangezogen. Optimalerweise könnte so in verschiedene Tiefen eine ähnliche Auflösung wie bei einer oberflächlichen Messung erreicht werden.

Das vorliegende Abstract inklusive des genannten Vorhabens wurde von der Fakultät für Physik und Astronomie der Universität Würzburg zur Anfertigung einer Masterarbeit bewilligt (23.07.2020).

Um die Möglichkeites des Setups zu evaluieren, welches im Verlauf dieser Arbeit aufgebaut wurde, wurden artifizielle Proben erstellt, indem eine Einzelzellschicht hippocampaler Neuronen der Maus, in welchen α-tubulin mit Alexa Fluor 647 angefärbt ist, auf einem 100 µm Maushirnschnitt plaziert wurden. Da letzerer ein hochgradig diffuses Medium zwischen dem Objektiv und den Fluorophoren darstellt, induziert es verschiedene optische Aberrationen, vor allem Sphärische Aberration und Astigmatismus. Indem die Wellenfront und die Punktspreizfunktion von 4 µm Fluosphere™ Beads, welche eine maximale Emission bei 505 nm haben, und 0.1 µm Tetraspeck™ Beads, welche eine maximale Emission bei 505 nm zeigen, aufgenommen wurde, konnten die Aberrationen von 521 nm zu 116 nm Quadratmittel des Wellenfrotfehlers reduziert werden. Weiterhin konnten mithilfe der adaptiven Optik Bruchpilot-Anhäufungen in einem Hinrschnitt der Honigbiene in den Calyx der Pilzkörper in einer Messtiefe von 80 µm sichtbar gemacht werden, welche im unkorrigierten Bild nicht sichtbar waren, indem das Quaddratmittel des Wellenfrontfehlers von 587 nm auf 196 nm reduziert wird. Insgesamt zeigt die Reduktion des Quadratmittels des Wellenfrontfehlers eine erfolgreiche Korrektur an, aber ist weit entfernt von einer Mikroskopiertechnik, die eine gewinnbringende Forschung in lebenswissenschaftlichen Bereichen garantiert.

Contents

Chapter 1

Theory

1.1 Lens optics

In this section, [1, 2] is followed to derive the Lensmaker equation.
Assuming we have already derived Snells law

$$n_1 \sin \alpha_1 = n_2 \sin \alpha_2 \tag{1.1}$$

from Fermats principle

$$\text{OPL} = x_1 n_1 + x_2 n_2 \ , \tag{1.2}$$

the image formation at a lens is of interest for this thesis. The equation mostly used in lens design is called Lensmaker equation and can be derived in the following way. First, lets assume a point-like light source S in a medium with refractive index n_{air} at distance d_{air} away from a spherical body with radius R and refractive index n_{glass}. The optical axis defined from the source S to the center C of the body. Lets further assume that $n_{\text{glass}} > n_{\text{air}}$. According to Snells law, a ray hitting the surface at point E is refracted towards the center of the body and intersects at point I under the angle β with the optical axis, at distance d_{glass}. The optical path length (OPL) is then after Fermats principle:

$$\text{OPL} = x_{\text{Air}} n_{\text{Air}} + x_{\text{glass}} n_{\text{glass}} \ , \tag{1.3}$$

with x_{air} and x_{glass} being the path lengths in air and in glass, respectively.
Now, one can make use of the simple geometry drawn here and replace x_{air} and x_{glass}:

$$\begin{aligned}
\text{OPL} = n_{\text{air}} \sqrt{R^2 + (d_{\text{air}} + R)^2 - 2R(d_{\text{air}} + R)\cos\beta} \\
+ n_{\text{glass}} \sqrt{R^2 + (d_{\text{glass}} + R)^2 - 2R(d_{\text{glass}} + R)\cos\beta} \ .
\end{aligned} \tag{1.4}$$

As we are looking for the minimum path length, we use the derivative and set it equal to zero. With R being constant, only $\partial\beta$ is of interest:

$$\frac{\partial \text{OPL}}{\partial \beta} = 0 \tag{1.5}$$

$$\frac{n_{\text{air}} R(d_{\text{air}} + R)\sin\beta}{2x_{\text{air}}} - \frac{n_{\text{glass}} R(d_{\text{glass}} + R)\sin\beta}{2x_{\text{glass}}} = 0 \ . \tag{1.6}$$

This equation can be simplified by removing the $\sin\beta$ and rearranging the variables:

$$\frac{n_{\text{air}}}{x_{\text{air}}} + \frac{n_{\text{glass}}}{x_{\text{glass}}} = \frac{1}{R}\left(\frac{n_{\text{glass}} d_{\text{glass}}}{x_{\text{glass}}} - \frac{n_{\text{air}} d_{\text{air}}}{x_{\text{air}}}\right) \ . \tag{1.7}$$

Now, an approximation is needed to proceed. Assuming a small angle β, also known as paraxial approximation, the distances along the optical axis and along the considered ray can be set approximately equal:

$$d_{\text{air}} \approx x_{\text{air}} \tag{1.8}$$

$$d_{\text{glass}} \approx x_{\text{glass}} \ , \tag{1.9}$$

1

which gives the solution for a single interface with radius R:

$$\frac{n_{\text{air}}}{d_{\text{air}}} + \frac{n_{\text{glass}}}{d_{\text{glass}}} = \frac{n_{\text{glass}} - n_{\text{air}}}{R} \ . \tag{1.10}$$

The equation connects the radius of the sphere to two distances, at which the ray intersects with the optical axis. However, the most common use-case of lenses is to transform rays coming from a point source to rays parallel to the optical axis, which is called collimation, or to focus a collimated beam of light into a single point. Both cases can be investigated by forming the limit of $d_{\text{glass}} \to \infty$ or $d_{\text{air}} \to \infty$:

$$\lim_{d_{\text{glass}} \to \infty} d_{\text{air}} = \frac{n_{\text{air}}}{n_{\text{glass}} - n_{\text{air}}} R = f_{\text{air}} \tag{1.11}$$

$$\lim_{d_{\text{air}} \to \infty} d_{\text{glass}} = \frac{n_{\text{glass}}}{n_{\text{glass}} - n_{\text{air}}} R = f_{\text{glass}} \ . \tag{1.12}$$

The distances derived under the limit are the focal lengths f for a single interface. However, the most simple form of a lens consisting of only one body, a so-called singlet, still consists two interfaces, one at the front of the lens where the ray enters, and one at the back where the ray leaves the lens.

The derivation of the focal lengths of a biconvex lens is analogous for a second surface, and can in detail be followed in [3]. The equation is presented in its final form, the so-called Lensmaker equation:

$$\frac{1}{f_{\text{air}}} = (n_{\text{glass}} - 1) \left(\frac{1}{R_{\text{l}}} - \frac{1}{R_{\text{r}}} \right) \ , \tag{1.13}$$

$$R_{\text{l}} : \quad \text{left lens curvature radius} \tag{1.14}$$

$$R_{\text{r}} : \quad \text{right lens curvature radius} \tag{1.15}$$

assuming $n_{\text{air}} = 1$. The equation is only valid for thin lenses and small angles.

Now, one can directly give an equation for the magnification of a lens using the distances from the lens center to the object on the left d_{l} and the image on the right d_{r}:

$$m = \frac{d_{\text{l}}}{d_{\text{r}}} \ . \tag{1.16}$$

1.1.1 Aberrations in lens optics

This paragraph follows [3].

Paraxial approximation assumes that the rays are sufficiently close to the optical axis, or in other terms, the angle between the ray and the optical axis is small. This approximation implies that

$$\sin \beta \approx \beta \tag{1.17}$$

$$\cos \beta \approx 1 \tag{1.18}$$

and can be written as a cut ($\big|$) in the Taylor series of $\sin \beta$ and $\cos \beta$ behind the first order:

$$\sin \beta = \beta \ \bigg| \ -\frac{\beta^3}{3} + \frac{\beta^5}{5} - \frac{\beta^7}{7} + \dots \tag{1.19}$$

$$\cos \beta = 1 \ \bigg| \ -\frac{\beta^2}{2} + \frac{\beta^4}{4} - \frac{\beta^6}{6} + \dots \tag{1.20}$$

When additional orders are taken into account, a description of optical aberrations which are caused by the geometry of the optic is possible. Optical aberrations can be described up to an infinite order - however, the main five are described here, as higher order aberration do not contribute significantly in most optical systems.

The most prominent one in most applications is **spherical aberration**, which causes rays passing the lens close to its perimeter to be focused further back than rays passing more central. **Coma** is caused when rays hit the surface of the lens at an angle to the optical axis. The rays on the side where the ray comes from are not focused correctly. **Astigmatism** is also caused when the rotational symmetry is broken. The ray bundle in plane with the object and the optical axis is focused closer to the lens than the ray bundle perpendicular to that, causing a three-dimensionally shaped focus. **Field curvature** is the tendency of lenses, to image a flat surface in object space to a spherical surface in image space shaped like the back side of the lens. Field curvature is sometimes called Petzval curvature after Joseph Petzval. Even though the term **distortion** is used generously, it also describes a specific aberration which causes radial gradients of magnification in the image. Negative distortion or Barrel refers to an increased magnification in the center, an effect that is commonly known from fish-eye lenses. The opposite, increased magnification

at the perimeter, is called Pincushion.

In addition to achromatic aberrations resulting from the lens geometry, **chromatic aberration** occurs due to the wavelength dependency of the refractive indices, known as dispersion, and regularly observed for example in rainbows. Chromatic aberration causes the focal length of the lens to depend on the wavelength, forming different image planes for different colors or light. However, chromatic aberration is corrected for in the so called apochromatic objectives (correction for at least three colors) and the achromatic lenses (correction for two colors) used in the setup. Also, as no spatial correlation between different color images is done in this work, the topic is not further investigated here.

In general, achromatic aberrations are more pronounced when using strong refraction, which is caused by lenses of short focal length, and when a large section of the spherical surface of a lens is used, as it happens when the full clear aperture of a lens is used. Therefore, the lenses used in the setup where chosen to be sufficiently large in diameter and and the system was laid out for long path lengths to use long focal length lenses where possible.

1.1.2 Image formation

Up to this point, no attention was given to the finite size of optical components. Every optical component has what is called a clear aperture, which defines the maximum beam width that can pass the component. For a lens, the clear aperture is given naturally by the casing of the lens. However, usually apertures are introduced intentionally into the system to ensure certain optical properties, for example telecentricity, which is described in Section 1.6. If the clear aperture of certain components of an optical system is chosen too small, a darkening effect at the edge of the image can occur, that is known as vignetting. Vignetting happens when peripheral ray bundles are partially blocked by the casing of the lens. The further peripheral the ray bundle travels, the more it is blocked - resulting in the dark transition in the edges of the image.
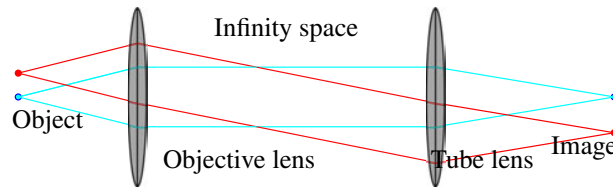
Figure 1.1: Image formation from a telecentric arrangement of objective and tube lens.

In a simple ideal infinity-corrected microscope, two lenses are used to relay the object plane to the image plane. The first lens, the objective itself, picks up the light from an object point in the front focal plane and forms a parallel ray bundle. The second lens, which is called tube lens, focuses the ray bundle and forms the image point one focal length behind it. The limiting aperture of the system is placed in the back focal plane of the objective. When limiting the light paths in the back focal plane, all image points are picked up under the same collecting angle, which is described by the numerical aperture, and therefore contribute equally to the brightness of the image, and no vignetting occurs. (See Figure 1.1) The magnification of such system is defined as the ratio of the focal lengths of the two lenses:

$$M = \frac{f_{\text{tube}}}{f_{\text{obj}}} \ . \tag{1.21}$$

The magnification written on an objective barrel is not referring to the magnification of the objective lens alone, but to the the whole imaging system it is proprietary to. This means, a $60 \times$ objective only creates a $60 \times$ magnification when used in conjunction with the associated tube lens. Therefore, in infinity optics systems, when knowing the focal length of the tube lens, the focal length of any objective lens f_{obj} can be easily calculated:

$$f_{\text{obj}} = \frac{f_{L_T}}{M_{\text{obj}}} \ , \tag{1.22}$$

where f_{L_T} is the focal length of the tube lens (sometimes also referred to as tube length) and M_{obj} is the magnification written on the objective barrel. [4] However, as objectives are composed of many layers of lenses and can not be approximated as thin lenses, the focal length is mostly only useful in theoretical considerations.

1.1.3 Determination of the beam diameters, the needed image magnification and characterization of the beam expanders used in the setup

Figure 1.2: Comparison of magnifying lens arrangements. The first magnifies the image plane and thereby the image itself. The second magnifies the Fourier plane and thereby the beam diameter. Such setup is also known as beam expander.
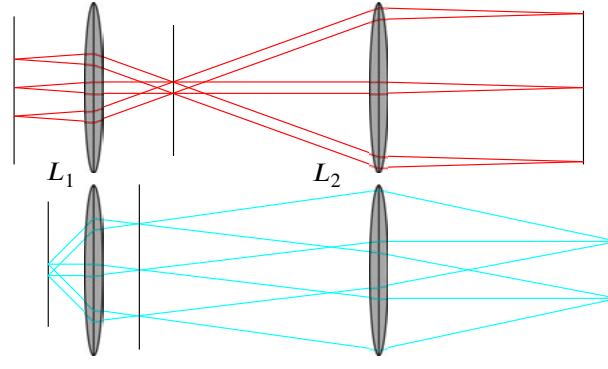
Analogous to the determination of the image magnification, one can also look at the magnification of the beam diameter $\varnothing$ in the Fourier plane. The setup, which is generally termed telescope or relay, is similar to 1.1 and consists of two lenses, here denoted as relay lens L_1 and L_2. Now, we consider parallel rays entering the first lens, as it would be the case if L_1 would be a tube lens. L_1 focuses the parallel beam and forms an image. Usually, one would place a camera here. However, if the space is left empty, the rays diverge from the image plane and hit the second lens L_2 in the same way light from an object hits the objective lens. L_2 then forms again a parallel beam. The setup effectively relays the Fourier plane to another Fourier plane, hence the name, creating an image plane in the middle. In Figure 1.2, one can see that the second lens has a larger focal length and thereby creates a larger beam width at the second Fourier plane. Such setup is also called beam expander, as the beam width is widened. This is useful, as two components, which will be introduced later, are placed in Fourier planes, and the beam width need to match their aperture as good as possible.

Considering the simple geometry drawn in Figure 1.2, the beam magnification of a beam expander can be calculated as:

$$\frac{\varnothing_1}{f_1} = \frac{\varnothing_2}{f_2}$$
$$\text{or}$$
$$\frac{\varnothing_1}{\varnothing_2} = \frac{f_1}{f_2} \ . \tag{1.23}$$

At this point, one can use the constraints of the system such as the intended image magnification of the system and the required beam width to calculate the required image magnifications and beam expansion factors.

It is best to start at the first component, which is the objective. After [5], the beam diameter at the exit pupil (in reference to the emission light) of the objective can be calculated as

$$\varnothing_{\text{obj exit pupil}} = 2 \cdot \text{NA} \cdot f_{\text{obj}} \ , \tag{1.24}$$

where f_{obj} is the focal length of the objective lens.

In case of the Nikon Ti Eclipse Microscope, equipped with a 100×1.49 NA oil immersion (IO) or 1.35 NA silicone oil (SO) objective, the diameter at the exit pupil is therefore

$$\varnothing_{\text{obj exit pupil}}^{\text{IO}} = 2 \cdot 1.49 \cdot \frac{200\,\text{mm}}{100}$$
$$= 5.96\,\text{mm} \ . \tag{1.25}$$

$$\varnothing_{\text{obj exit pupil}}^{\text{SO}} = 2 \cdot 1.35 \cdot \frac{200\,\text{mm}}{100}$$
$$= 5.4\,\text{mm} \ . \tag{1.26}$$

This determines the diameter of the first Fourier plane to be 5.4 mm. In the next Fourier plane, the deformable mirror (DM) will be placed. The aperture of the DM is $\varnothing_{\text{DM}} = 10$ mm [6].

In the following Fourier plane, the WFS will be placed. The WFS has an aperture of $\varnothing_{\text{WFS}} = 7.5$ mm [7].

Usually, microscopes are designed to form an image of a certain size, that matches the size of conventional image

sensors. However, the camera used in the system features a sensor that has a sensor size of $\varnothing_{\mathrm{CAM}} = 22.5$ mm [8], which is about twice as large compared to other camera sensors. Therefore, the system should give an additional $2\times$ magnification of the image. To calculate the required focal lengths of the lenses, the required magnification factors of the relay systems have to be determined. Therefore, the ratio of the beam diameter at the exit pupil of the objective and the sizes of the apertures of the DM, the WFS, and the size of the camera sensor are calculated:

$$\frac{\varnothing_{\mathrm{DM}}}{\varnothing_{\mathrm{obj\ exit\ pupil}}} = 1.678 \tag{1.27}$$

$$\frac{\varnothing_{\mathrm{WFS}}}{\varnothing_{\mathrm{DM}}} = 0.75 \ . \tag{1.28}$$

These ratios should be approximately matched by the ratio of the focal lengths of the chosen lenses.
For the relay system of the DM, the first lens is the tube lens with a fixed focal length of 200 mm. Therefore, the next lens L_1 was chosen to have $f_1 = 300$ mm, giving a magnification of

$$\frac{300\,\mathrm{mm}}{200\,\mathrm{mm}} = 1.5 \approx 1.678 \ , \tag{1.29}$$

which results in a beam diameter of 8.94 mm, only slightly underfilling the aperture. It was of utmost importance to not overfill the pupil. Because the mirror is placed in the Fourier plane, overfilling would not just crop the image, but rather reduce the overall intensity and act as a lowpass filter, removing high spatial frequencies. Therefore, the slight underfill was considered optimal. Next, the beam width needs to be reduced to match the aperture of the WFS. Here, both lenses could be chosen freely. However, to fit the system onto the optical table, the focal lengths were chosen to be $f_{\mathrm{WFS},1} = 300$ mm and $f_{\mathrm{WFS},2} = 250$ mm, giving a ratio of

$$\frac{250\,\mathrm{mm}}{300\,\mathrm{mm}} = 0.83 \approx 0.75 \ , \tag{1.30}$$

which is slightly larger, but compensates for the slight underfill at the DM, resulting in a beam width of 7.45 mm. Next, the $2\times$ magnification at the camera needs to be ensured. The Lens L_1 has already been chosen to have $f_1 = 300$ mm, therefore L_i was chosen to have $f_i = 600$ mm.

1.2 Fourier transformation by lenses and wave optics

The following paragraph follows [1]. In the former section, the planes conjugate to the image planes were called Fourier planes. To understand this terminology, the phase transformation of a thin lens will be derived. In general, the lens causes a phase delay due to its higher refractive index and therefore lower speed of light. However, for a biconvex lens, the phase delay is stronger in the central part where the lens is thicker, and less pronounced peripheral.
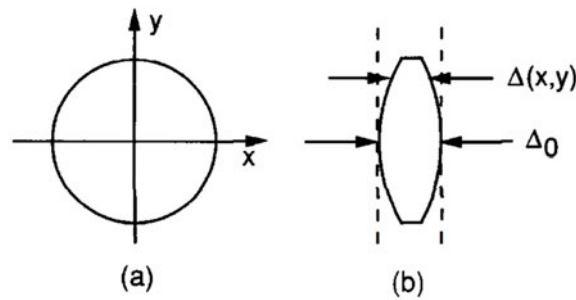
Figure 1.3: Definition of Δ_0 and $\Delta(x, y)$ on a biconvex lens. Image is taken from [1].

Assuming the maximum thickness of the lens is Δ_0 and the thickness depending on the coordinate on the lens is $\Delta(x, y)$. A unity plane wave may pass the lens, denoted by the dotted lines. The phase delay caused by the lens can then be expressed as

$$\phi(x, y) = kn\Delta(x, y) + k(\Delta_0 - \Delta(x, y)) \ , \tag{1.31}$$

with $kn\Delta(x, y)$ being the phase delay caused in the lens and $k(\Delta_0 - \Delta(x, y))$ the normal phase propagation from the dotted line until the wave hits the lens and after the lens leaves the lens to the second dotted line (see Figure 1.3). This transformation can be rewritten in a multiplicative form using complex numbers:

$$t_l(x, y) = \exp\big(ik\Delta_0\big) \exp(ik(n - 1)\Delta(x, y)) \ . \tag{1.32}$$

The meaning of the transformation function $t_l(x, y)$ is the relation of the wave before passing the lens $U_l(x, y)$, which we assume to be 1, and after passing the lens $U'_l(x, y)$ The thickness function can be derived using geometrical considerations which can be followed in [1]. Here, only the solution is given, assuming a paraxial approximation:

$$\Delta(x, y) = \Delta_0 - \frac{x^2 - y^2}{2} \left(\frac{1}{R_1} - \frac{2}{R_2} \right) . \tag{1.33}$$

This can be inserted into (1.32) to yield:

$$t_l(x, y) = \exp(\mathrm{i}kn\Delta_0) \exp\left(-\mathrm{i}k(n-1)\frac{x^2 - y^2}{2} \left(\frac{1}{R_1} - \frac{2}{R_2} \right) \right) . \tag{1.34}$$

Using the Lensmaker equation (1.10), R_1, R_2 and n can be replaced by the focal length f of the lens:

$$t_l(x, y) = \exp\left(-\mathrm{i}\frac{k}{2f}(x^2 + y^2) \right) . \tag{1.35}$$

As the incident wave was assumed to be Unity, the emerging wave can be expressed as

$$U'_l(x, y) = \exp\left(-\mathrm{i}\frac{k}{2f}(x^2 + y^2) \right) , \tag{1.36}$$

which resembles a broad approximation of a spherical wave. This is expected, as a convex lens transforms a planar wave (=collimated beam) into a spherical wave (=focussed beam). One should note that the spherical wavefront is only obtained under paraxial conditions. Otherwise, non-spherical wavefronts are formed, which are covered descriptive in the Section 1.1.1 about aberrations.

Lets drop the unity wave and assume a monochromatic plane wave of amplitude A, normally incident to the lens, which has an intensity distribution $t_A(x, y)$. The disturbance incident to lens surface is thereby

$$U_l(x, y) = At_A(x, y) . \tag{1.37}$$

After passing the lens, the wave writes according to the transformation function:

$$U'_l(x, y) = U_l(x, y) \exp\left(-\mathrm{i}\frac{k}{2f}(x^2 + y^2) \right) . \tag{1.38}$$

To investigate the $U_f(u, v)$ in the back focal plane of the lens, Fresnel's law is used. The equation is derived in [3]. By setting $z = f$:

$$U_f(u, v) = \frac{\exp\left(\mathrm{i}\frac{k}{2f}(u^2 + v^2) \right)}{\mathrm{i}\lambda f} \times \iint_{-\infty}^{\infty} U'_l(x, y) \exp\left(\mathrm{i}\frac{k}{2f}(x^2 + y^2) \right) \exp\left(-\mathrm{i}\frac{2\pi}{\lambda f}(xu + yv) \right) \mathrm{d}x \, \mathrm{d}y . \tag{1.39}$$

Replacing $U'_l(x, y)$ using equation (1.38), the the quadratic terms in the integral cancel and one obtains:

$$U_f(u, v) = \frac{\exp\left(\mathrm{i}\frac{k}{2f}(u^2 + v^2) \right)}{\mathrm{i}\lambda f} \times \iint_{-\infty}^{\infty} U'_l(x, y) \exp\left(-\mathrm{i}\frac{2\pi}{\lambda f}(xu + yv) \right) \mathrm{d}x \, \mathrm{d}y . \tag{1.40}$$

Now, the Fourier spectrum of the wave in the front focal plane and incident to the lens can be written as

$$F_0(f_x, f_y) = \mathcal{F}\{At_a\} \qquad\qquad F_l(f_x, f_y) = \mathcal{F}\{U_l\} . \tag{1.41}$$

Both are related under the assumption of paraxial propagation:

$$F_l(f_x, f_y) = F_0(f_x, f_y) \exp\left(-\mathrm{i}\pi\lambda d(f_x^2 + f_y^2) \right) . \tag{1.42}$$

Inserting this into equation (1.40), one yields:

$$U_f(u, v) = \frac{\exp\left(\mathrm{i}\frac{k}{2f}(u^2 + v^2) \right)}{\mathrm{i}\lambda f} F_l\left(\frac{u}{\lambda f}, \frac{v}{\lambda f} \right) . \tag{1.43}$$

Inserting equation 1.42, one obtains:

$$U_f(u, v) = \frac{\exp\left(\mathrm{i}\frac{k}{2f}\left(1 - \frac{d}{f}(u^2 + v^2) \right) \right)}{\mathrm{i}\lambda f} F_0\left(\frac{u}{\lambda f}, \frac{v}{\lambda f} \right) \tag{1.44}$$

$$= \frac{\exp\left(\mathrm{i}\frac{k}{2f}\left(1 - \frac{d}{f}(u^2 + v^2) \right) \right)}{\mathrm{i}\lambda f} \times \iint_{-\infty}^{\infty} t_a(\xi, \eta) \exp\left(-\mathrm{i}\frac{2\pi}{\lambda f}(\xi u + \eta v) \right) \mathrm{d}\xi \, \mathrm{d}\eta . \tag{1.45}$$

When now assuming $d = f$, the first factor vanishes and leaves the exact equation well known as a Fourier transformation. Thus, under paraxial conditions, a lens performs a two-dimensional Fourier transformation. An image placed in the front focal plane is transformed into the frequency representation of the image in the back focal plane. Thus the name Fourier plane.

In Fourier space, the frequencies increase proportional to the distance to the center. This means, a limiting aperture in the Fourier space, as it is present in most objectives back focal plane, cuts off frequencies above a certain value and thereby directly sets the finite frequency band, that the objective can transfer. Therefore, a definition of a transfer functions in space and frequency domain are needed, which lead to the definition of resolution.

1.2.1 Point spread function, optical transfer function and the diffraction limit

In general, the limiting aperture in the back focal plane can be written as a circle or pupil function $\circ(r)$:

$$\circ(r) = \begin{cases} 1 & : \ r < 1 \\ \frac{1}{2} & : \ r = 1 \\ 0 & : \ \text{else} \ . \end{cases} \tag{1.46}$$

The Fourier transform of these types of functions is well known:

$$\tilde{\circ}(\tilde{r}) = \frac{B_1(2\pi\tilde{r})}{\tilde{r}} \ , \tag{1.47}$$

with B_1 being the first Bessel function.
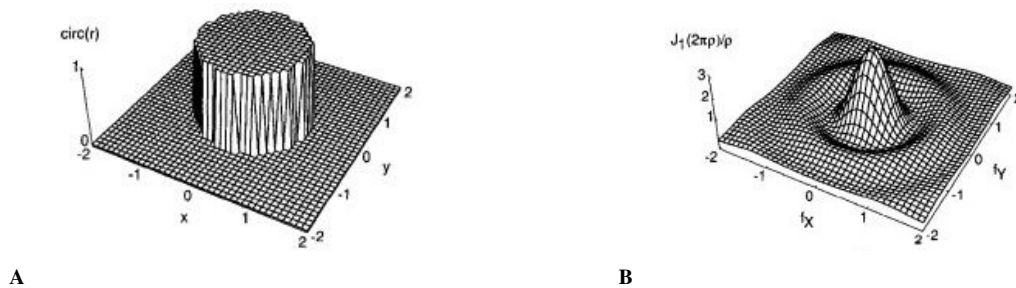
Figure 1.4: A Circle function and **B** Fourier transform of the circle function. The Image is taken from [1]

What this means, is that the transmission function of an optical setup is always modulated by the Bessel function resulting from the limiting aperture in the Fourier domain. This implies, that an given intensity distribution in the object plane, even when imaged by ideal lenses, will always lead to an intensity distribution that is a convolution of the original intensity distribution and a function consisting of Bessel functions, depending on the exact properties of the optical system. For a point-like emitter in the object plane, the distribution in the image plane is called the point spread function (PSF), and is used to characterize optical systems.

This means that when two point sources are sufficiently close together, the resulting PSFs overlap and the individual points are not distinguishable any more. This leads to the definition of the diffraction limit after Rayleigh, also called Rayleigh criterion: Two point-like emitters can be individually resolved, when the main maximum of one PSF overlaps the first minimum on the other PSF.
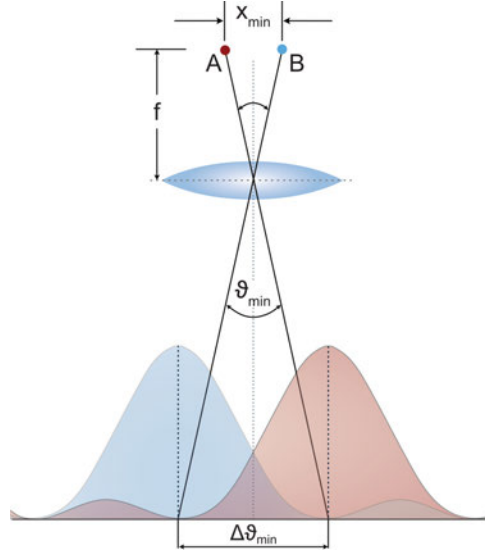
Figure 1.5: Visualisation of the diffraction limit. The maximum of the left PSF overlaps the minimum of the left PSF. Image is taken from [2]

The PSF is defined in image space, as it is the transfer function from the object to the image. When looking at the transfer function for frequencies, one can define the optical transfer function (OTF), which is the Fourier transform of the PSF:

$$OTF(k_x, k_y) = \mathcal{F}\{PSF(x, y)\} \ . \tag{1.48}$$

The OTF describes the frequency band transmission. For a point emitter, the OTF is maximal at $k_x = k_y = 0$ and falls off to both sides, until it reaches zero at the so-called cutoff frequency ω_{lim}, which is the frequency analog to the resolution limit.
One should note that the considerations drawn here are only valid for the far field.

1.2.2 Phase modulation and Zernike polynomials for wavefront representation

To characterize wavefront shapes, Fritz Zernike introduced a set of polynomials. The polynomials are defined in polar coordinates on a unit circle, as most optical devices show a radial symmetry. Using Zernikes approach, a wavefront $W(\rho, \theta)$ can be described, using m as azimuthal and n as radial indices, as:

$$W(\rho, \theta) = \sum_{n,m} c_n^m Z_n^m(\rho, \theta) \ , \tag{1.49}$$

with $Z_n^m(\rho, \theta)$ being the Zernike polynomials, defined as

$$Z_n^m(\rho, \theta) = R_n^m(\rho) \begin{cases} \sin(m\theta) & : m < 0 \\ \cos(m\theta) & : m > 0 \\ 1 & : m = 0 \ . \end{cases} \tag{1.50}$$

The radial factor $R_n^m(\rho)$ is defined as

$$R_n^m(\rho) = \begin{cases} \sum_{l=0}^{(n-m)/2} \frac{(-1)^l (n-l)!}{l!(\frac{1}{2}(n+m)-l)!(\frac{1}{2}(n-m)-l)!} \rho^{n-2l} & : (n-m) \text{ even} \\ 0 & : (n-m) \text{ odd} \ . \end{cases} \tag{1.51}$$

From that point, the Zernike polynomials can be calculated. Even though the definition appears bulky, the Polynomials can be directly linked to the different optical aberrations. For example, Z_2^{-2} describes Astigmatism, whis means, that when a phase-modulating object shaped like the Zernike polynomial is placed in the Fourier plane, it will directly induce the associated aberration. Likewise, if an inversed pattern is applied, an existing aberration can be canceled out. This is the fundamental working principle of the wavefront correction, which will be explained further in Section 1.4.
Different conventions exist to number the Zernike coefficients by a single index. Thorlabs, the provider of the software used for wavefront control, follows ANSI Z80.28-2017 standard [9], which is given for reference:
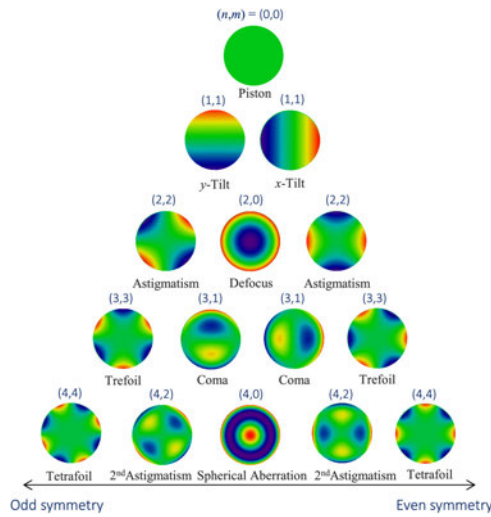
Figure 1.6: Plot of the first 15 Zernike Polynomials. Z1 is just a flat surface, so it is not of interest in adaptive optics (AO). Z2 and Z3 are tip and tilt, which also usually do not need correction in a well-aligned system. Figure is taken from [10].
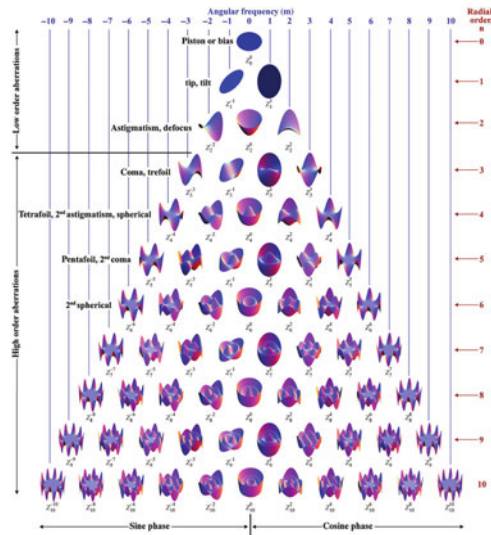
Figure 1.7: Plot of the first 15 Zernike Polynomials. Z1 is just a flat surface, so it is not of interest in adaptive optics (AO). Z2 and Z3 are tip and tilt, which also usually do not need correction in a well-aligned system. Figure is taken from [11].

The polynomials can be plotted on the unit circle. Here, they are grouped such that each line shows the corresponding orthogonal polynomial mirrored to the other side of the pyramid. Mathematically, the Zernike polynomials are orthogonal on the unit circle, meaning that it is possible to individually alter them without influencing others. In practice, only a perfectly aligned system allows to individually change the Zernike numbers. If misalignment is present, the Zernike numbers are linked together. In the system build during this thesis, especially the link between Z5 (defocus) and Z13 (spherical aberration) could not be fully removed and independent correction was possible only to a certain degree.

Often, instead of giving the magnitude of the individual Zernike polynomials, the root mean square wavefront error is reported as the root mean square of the whole wavefront shape captured by the WFS. Usually, the value is given in µm, however, sometimes it is reported in numbers of the wavelength of the captured wavefront. In general, the rms wavefront error gives a good approximation of the average magnitude of the Zernike polynomials.

Interpretation	ANSI Z80.28	Z_n^m
piston	01	Z_0^0
y-tilt	03	Z_1^{-1}
x-tilt	02	Z_1^1
astigmatism	06	Z_2^{-2}
defocus	05	Z_2^0
astigmatism 45°	04	Z_2^2
y-trefoil	07	Z_3^{-3}
y-coma	09	Z_3^{-1}
x-coma	08	Z_3^1
x-trefoil	10	Z_3^3
tetrafoil 45°	11	Z_4^{-4}
2. astigmatism 45°	12	Z_4^{-2}
spherical aberration	13	Z_4^0
2. astigmatism	14	Z_4^2
tetrafoil	15	Z_4^4

Table 1.1: The first 15 Zernike numbers in index and ANSI nomenclature, as well as the physical interpretation. Note that many different nomenclatures exist. [6, 7]

1.3 Single molecule localization and *d*STORM microscopy

As we have discussed in the former sections, an intrinsic physical limit exists on the resolution of an optical system. Applied to the optical components used in the setup, the diffraction limit for 655 nm, the peak emission of Alexa Fluor 647, and the used 100×1.35 NA objective lies at about

$$\frac{\lambda}{2\mathrm{NA}} = 243\,\mathrm{nm}\;. \tag{1.52}$$

which is about the size of large macromolecules, viruses, bacteria, and smaller than most cell types. To increase the resolution, one can try to change the parameters in equation (1.52). For example, in electron microscopy, the much smaller wavelength of fast electrons is in the range of pm, lowering the resolution limit significantly.
Also, objectives up to a NA of 1.49 are available. But as one can not wrap the objective around the object, a natural limit exists here.
However, different approaches were developed to circumvent the diffraction limit using visible light and resolve single molecules, which were therefore termed single molecule localization microscopy (SMLM) techniques. In all SMLM techniques, a property of the fluorophores is used. Fluorophores can go into a non-emissive dark state if they are exposed to high intensity radiation, due to intersystem crossing to a long-lifetime triplet state. However, very few fluorophores at once can spontaneously recover for a short amount of time. The time each fluorophore spends in each state is called duty cycle, and depends on the type of fluorophore as well as on the buffer solution used. Under a continuous illumination, a recorded time lapse would show a blinking behavior, as in every frame only some fluorophores are emitting for a very short time. The advantage is, that it is very unlikely to observe any overlap between the emitters active in each frame, so the PSF of each emitter can be individually fitted to obtain a resolution up to about 30 nm in *d*STORM . The difference between the SMLM techniques is mainly the way they use to deactivate the fluorophores. In *d*STORM a continuous high-intensity widefield illumination is used, often combined with highly inclined angle (HILO) or total internal reflection (TIRF) illumination.

1.4 Deformable mirror

Deformable mirrors are used to shape the wavefront to induce or correct certain wavefront shapes. To fully correct and recover a flat WF, amplitude, polarization and phase informations must be recovered. A deformable mirror can only alter the phase. To do that, a DM introduces an aberration into the optical system by modifying the optical path length (OPL) by a distance equal to twice the mirror surface deformation. Consequently, the phase aberration introduced by the DM varies in the inverse proportion to the wavelength. It may seem, therefore, that the DM provides chromatically dependent correction. However, one should also consider the source of the aberrations in the system. Aberrations induced by the specimen are caused by its refractive index structure, and this structure modifies the OPL. It follows that the phase aberrations from the specimen also scale inversely with wavelength, so

the compensation provided by the DM varies in exactly the same way. Discrepancies could arise if the specimen is dispersive, but this is not common in biological specimens. [12]

1.4.1 Placement of the deformable mirror in a widefield microscope setup

Each light ray emitted in different directions by each fluorophore in the focal plane of the objective travels a unique path, first through the specimen and then trough the optics to the camera. Therefore, all these different light rays experience an individual wavefront aberration, and to perfectly correct the whole image, an individual wavefront correction for every light ray from each fluorophore would be needed.

As this is impossible to realize, one makes use of the back focal plane. In principle, it does not matter whether wavefront sensing and correction are done in image or in Fourier space. The advantage of the Fourier space of a lens is, that the light coming from each fluorophore is distributed over the whole beam diameter. [13] Wavefront sensing and correction in the Fourier plane therefore treats the global or mean aberration, which usually results in a good overall correction. [14]

The DM is placed in the first Fourier plane behind the objectives back focal plane.

1.4.2 Choice of the deformable mirror over a spatial light modulator for fluorescence microscopy

The spatial light modulator (SLM) is a pixel grid, which modulates the phase of a wave passing through each pixel individually. This allows for very fine control of the lights wavefront. However, as known from display technology, only polarized light passes through the grid, which is not a concern in the excitation path, were light modulators are frequently used, but it would lead to a strong dimming in the emission path. Also, the SLMs pixel transparency is highly wavelength dependent. The independence from wavelength and polarization make the DM the superior choice for placement in the emission light path, even though it usually feature much less individually controllable sections. [12] The DM used here features 40 individually controllable segments in addition to three bending arms for tip-tilt control.[6]

1.5 Shack-Hartmann wavefront sensor

In general, one can divide adaptive optics system into active wavefront sensing setups and indirect, image based algorithms. The latter will not be evaluated here.

1.5.1 Structure and working principle of a Shack-Hartmann wavefront sensor

The Shack-Hartman wavefront sensor (WFS) was originally designed by R. Shack and J. F. Hartmann [15], and uses small lenses (lenslets) arranged in a grid array to focus parallel beams onto a CCD-chip. [16, 17, 15] Thereby, the parallel beam is split into a number equal to the number of lenslets in the lens grit array (LGA), and each lens creates a small focus point.
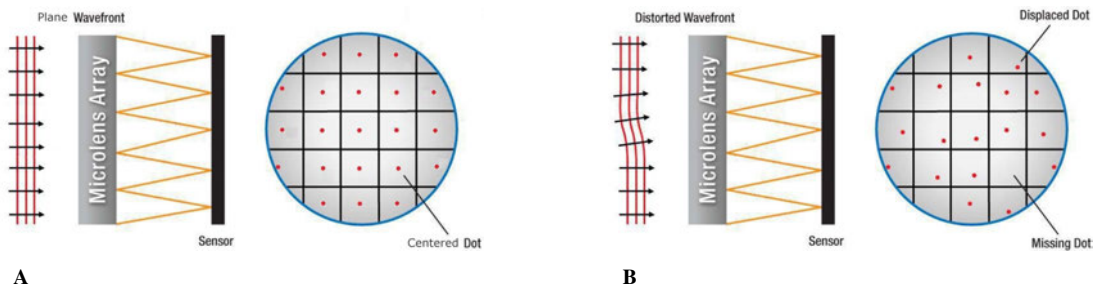
Figure 1.8: Working principle of a Shack-Hartmann wavefront sensor. Adapted from [17]

As shown in Figure 1.8, the CCD chip is divided into one masterpixel for each lens, whereby every masterpixel splits up into many subpixels. Whereas a perfect plane wave would get focused onto the subpixel in the middle of its masterpixel (Figure 1.8A), a distorted wave front would get either defocused or focused onto off-center subpixels (Figure 1.8B). The local deviation of a beam spot δ_i from the center of the corresponding masterpixel i is directly proportional to the local slope of the WF, expressed as the derivative $\partial_{xyz}(\text{WF})$: [18]

$$\delta_i \sim \partial_{xyz}(\text{WF}) \, . \tag{1.53}$$

1.5.2 Positioning of an active wavefront sensor in a widefield microscope setup

As discussed in Section 1.4, the adaptive optics including the WFS will be placed in the Fourier plane. In general, two positions are possible to deflect the beam out of the beam path that leads to the camera - before and after the imaging lens L_i. As stated by [19, 20], converging light reflected by a dichroic filter (DF) induces aberrations, due to the incident angle-dependent translocation relative to the optical axis. Therefore, the dichroic filter should be placed before the imaging lens L_i in a parallel beam section, as shown in Figure 3.3. [21] Because the beam width is small (5.96 mm) at the DM and widens until it reaches L_i, the dichroic filter and the containing cube can be chosen to have apertures of 25 mm only, matching the commercially available standard size, when placed close to the DM. Even though this approach implicates the use of 2 additional lenses ($L_{WFS,1}$ and $L_{WFS,2}$) and does not include L_i in the correction, the error is small compared to the induced aberrations when the DF is placed in the converging beam directly in front of the camera. [19] This setup, using the dichroic filter behind the imaging lens, is shown in Figure 1.9A.
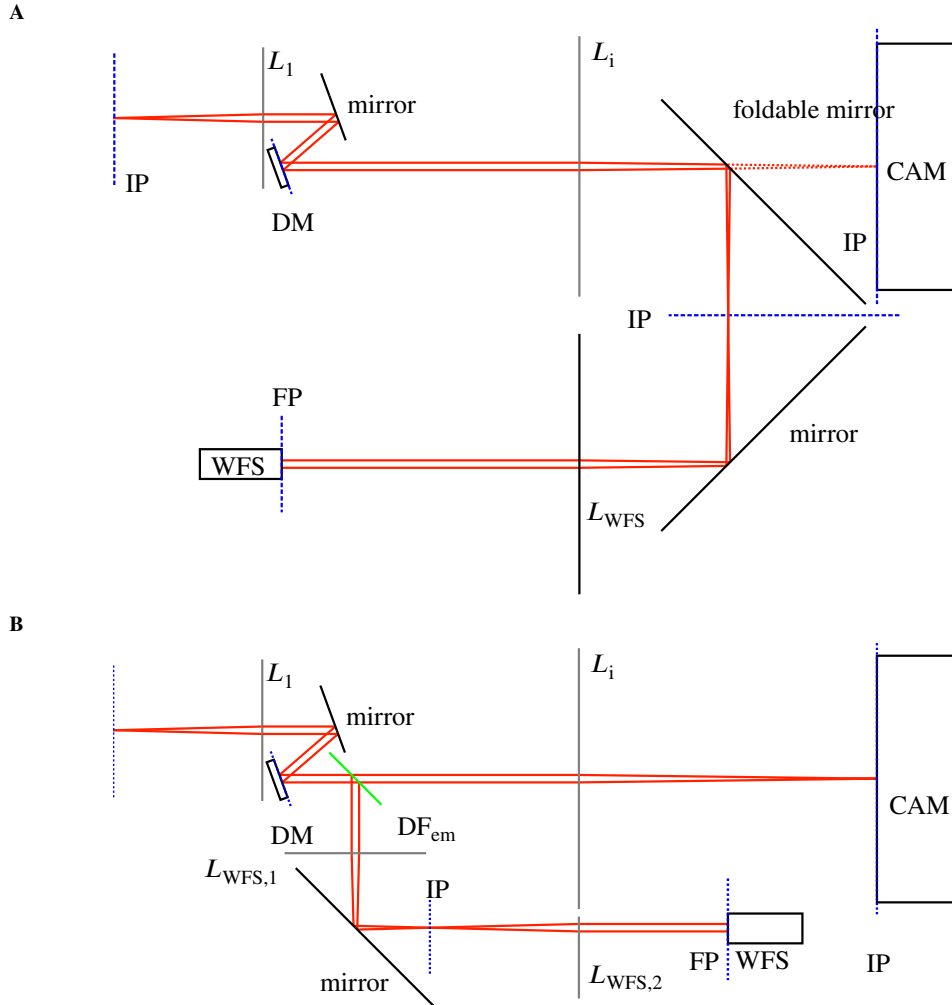
Figure 1.9: Two possible ways to couple light from the detection path to the WFS. **A** The dichroic filter is placed behind the imaging lens. Only one additional lens is needed, and the aberrations from the imaging lens are captured by the WFS. However, the beam splitting does happen in a converging beam and the lens L_{WFS} has to be matched to the 400 mm imaging lens, enlarging the setup significantly. **B** The dichroic filter is placed before the imaging lens. Here, two additional lenses ($L_{WFS,1}$ and $L_{WFS,2}$) are needed to relay the DM to the WFS, and the lens L_1 is not part of the correction path.

1.5.3 Aperture stop in front of the wavefront sensor to restore a defined wavefront

As described briefly in Section 1.5,t he WFS uses microlenses to focus small portions of the beam from the Fourier plane to the underlying image sensor. Every point source in the image plane thereby generates a set of points, one behind each microlens, which is called spotfield image. The location of a spot on its associated masterpixel is then used to calculate the wavefront slope at the area of the microlens. [14]

Having two or more spatially separated emitters in the image plane results in two or more spots on each masterpixel. If the emitters are close and their light undergoes comparable aberration, the spots overlap and therefore still allow for a correct wavefront calculation - however, as the resulting points on the masterpixels are larger, the uncertainty

in the calculation of the location may get larger.

In biological samples which are labeled over a large area, every emitter generates a different spot on each masterpixel. [22] As a result, every masterpixel receives a full image of the sample, rendering a correct localization impossible. [23] In fact, the WFS finds a spot position at the position of highest brightness, but in such case this does not reflect a physical wavefront. Interestingly, the strict execution of the wavefront calculation leads to a strong spherical aberration, which is most probably not physically present. [24] To circumvent this, the wavefront measurement was restricted to a small area of the sample by inserting a small aperture in the image plane in front of the WFS. This cuts off all non-paraxial rays, but also reduced the number of photons reaching the sensor. As the sensitivity of the sensor is finite, a compromise was necessary and found at an opening diameter of around 0.9 mm. [13] It is also possible to use focal illumination for the wavefront correction, reaching higher laser intensities in the correction area. However, it was not feasible to set up a focal illumination in a widefield microscope.

1.5.4   The choice of the lens grid array

As a general rule, the number of lenslets in the WFS should be at least $3\times$ the number of segments of the DM to meet the Nyquist criteria generate a good sampling. [14] As the DM has 40 segments, the WFS lenslet array was chosen to have at least 120 lenslets. In general, more lenslets generate a better resolution of the Zernike coefficients, however, as every lens produces a small image on the masterpixel behind it, the brightness of that image is divided by the number of lenslets in the array, thereby reducing the signal for each masterpixel. As the sensor is dealing with low light levels, the number of lenslets was chosen to be $45 \times 45 = 2025$.

1.6   Telecentricity, its absence in commercial microscopes and the use of a field lens for retrieval

Lenses are usually described by their ability to focus a collimated beam of light into the focal point of the lens, or - in reverse - creating a collimated beam of light when placed one focal length away from a point-like light source. In an infinity-corrected microscope, a point-like light source is picked up by the objective lens and focussed to infinity, meaning the objective creates a collimated beam. The tube lens then focuses the beam again to form an image plane which can be captured by a camera. The space between the objective and the tube lens, where the beam is collimated, is called infinity space.

For a centrally placed point source, as shown in Figure 1.10 in blue, as the rays are parallel, it does not matter how far the objective and the tube lens are apart. The tube lens always creates a central point again. However, the matter changes when a second point source is introduced, which in not located centrally above the objective, as is is common when resolving large samples. In this case, the second lens only focuses the points back to its original relative position, if the two lenses are separated by the sum of their focal lengths. Such setup is called telecentric or 4f-configuration. If you change the focus of such system, the magnification will not change, because the light cones coming from the tube lens and forming the image are parallel.
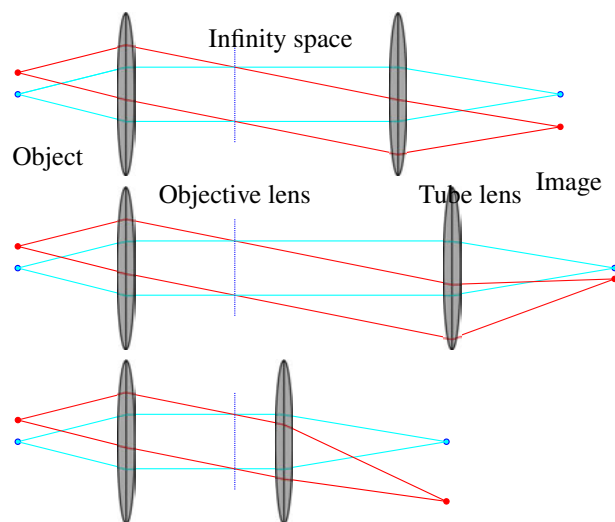

Figure 1.10: The movement of the tube lens relative to the objective causes the image forming light cone to bend inwards or outwards. The upper part resembles a full telecentric configuration, both examples below show only telecentricity on the object side.

If both lenses are moved closer, the cone of light coming from the tube lens to form the off-centered image point

will bend outwards, if moved further apart, it will bend inwards. As a result, the two points are imaged further apart or closer together, which means the image is magnified or demagnified. Both cases represent non-telecentric optics. In non-telecentric setups, a change in focus always results in a change in magnification, because the light cones are not parallel.

One can distinguish between object-side telecentricity, image-side telecentricity, and full or double telecentric systems. In an optical system, the telecentricity depends on the position of the beam limiting aperture stops in the system. Fig. 1.11A shows an true 4f-configuration, which always is double-telecentric. In fig. 1.11B and 1.11C, the infinity space was shortened, such that the system is not a true 4f-configuration any more. Both systems have the exact same measurements and lens positions. By placing the aperture stop at the image side, the system is image-side telecentric, by placing it at the object side, the system is object-side telecentric. Such object-side telecentric systems are used in most of the microscope, including the Nikon Ti-E, where the stop is usually positioned inside the objective barrel. Image-side telecentricity would lead to magnification depending on the distance of the object to the objective, therefore such system is not used.
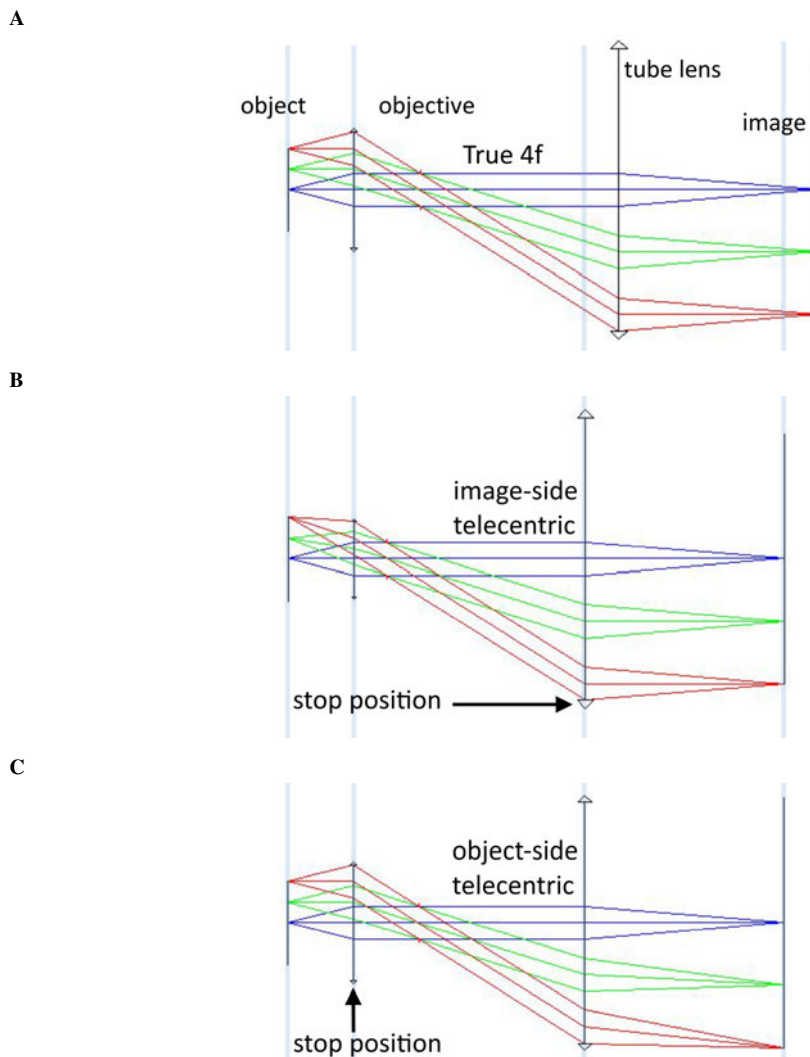
Figure 1.11: Changing the stop position changes the microscope telecentricity. **A** A fully telecentric configuration. **B** Only image-side telecentricity is given. **C** Object-side telecentricity. Figures taken from [25]

In the Nikon Ti Eclipse inverted microscope, used as the microscope's base component in this thesis, the distance between the objective lens and the tube lens, which is called the tube length, is about 5 cm shorter than the sum of the respective focal lengths, 2 mm for the objective (see equation 1.22) and 200 mm for the tube lens. [26] Therefore, the objective and the tube lens do not form a 4f-configuration, and the microscope is not double-telecentric. In general, microscopes only provide telecentricity on the object side. This is archived by placing the stop in the back focal plane of the objective lens, which lies inside the objective barrel. Reasons for omitting the double-telecentricity are basically three-fold: First, the image side telecentricity is not needed, as long as you keep the camera sensor at a defined position, which is standardized and given by a properly mounted camera directly attached to the microscopes ISO C-mount. [27] Second, Nikon uses a 200 mm tube lenses by default [28], which means that

for a double-telecentric configuration, one would need over 400 mm of space between the objective and the image plane at the camera port, which would make the microscope substantially larger, increasing cost and reducing portability. Third, the beam diameter between the objective and the tube lens increases, as shown in Figure 1.13. By decreasing the tube length, a tube lens of smaller diameter can be used, which reduces cost. Note that only the beam width at the tube lens and not the magnification at the following image plane is varied by the position of the tube lens.

However, the lack of image-sided telecentricity introduces two main challenges: First, the ray bundles are not parallel, which means that the beam diameter increases over the whole imaging light path, creating the need to use larger aperture lenses and, because lens diameters are limited, limiting the maximum length of the relay systems. Having short relay systems is possible by using shorter focal length lenses, however, these introduce more spherical aberration and limit the beam diameter sizing possibilities.

Second, while the Fourier plane of a central image point lies at the focal point of the Fourier transforming lens, as one would expect, the Fourier planes of image points more remote from the center are formed further back due to the bended non-central rays. This way the Fourier plane of the whole image is not defined any more. Rather, Fourier planes correspond to concentric rings in the image plane, assuming axially symmetric optics. Therefore, the adaptive optics can in a given position only correct for a certain part of the image.
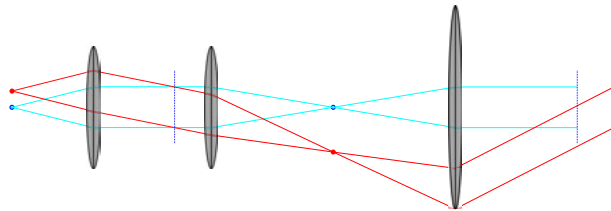
Figure 1.12: By placing the tube lens too close to the objective, the Fourier planes location depends on the location of the conjugate image point.

There are different approaches to solve this problem. The most obvious one would be to place the tube lens further apart from the objective to restore the 4f-configuration. However, the tube lens is custom fitted inside the Nikon Ti-E body and glued in place. Rising the objective lens instead would interfere with the perfect focus system and the xy-stage.

The only viable solution when working with a pre-assembled microscope body is to use an additional lens, a so-called field lens, to correct for the diverging rays. A field lens usually describes a lens placed between the tube lens and the image plane to change the magnification of the system or - in our case - to restore telecentricity on the image side. The field lens bends the light cones inwards and straightens them as if they come from a true 4f-configuration. The drawback to this approach is, that the magnification of the system changes depending on the position of the lens, which is not desirable. A solution is to use the extreme case of a field lens, namely to place the lens directly in the image plane. Usually, this is not possible, as the camera sensor is located at the image plane. However, in our system, the image plane is freely accessible, as the image is relayed to another image plane for the camera. Adding a lens at the image plane does not change the magnification of the system, and a central image point is not affected in any way, but non-central rays are refracted inwards and by choosing an appropriate focal length of the field lens, the telecentricity can restored.

One should note that by placing a lens in the image plane, every impureness, scratch or dirt on the lens surface is imaged directly to the camera, therefore the lens was handled with extra care and kept covered until use. [29]
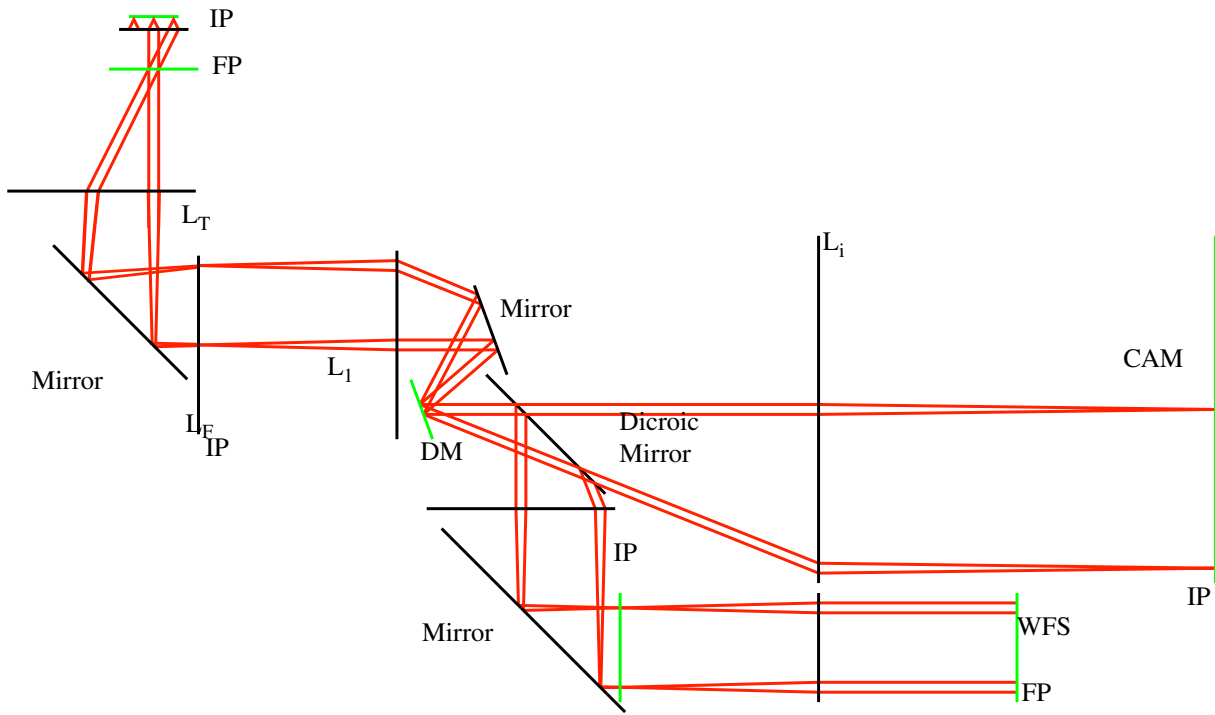
Figure 1.13: Light paths at the Nikon Ti-E. The light cones after the tube lens bend outwards and are corrected by the field lens to restore the image-side telecentricity.

1.7 Optical properties of brain tissue and its implication on the difficulties of optical brain imaging

To motivate the necessity of aberration correction for optical imaging in deep tissue and especially in brain tissue, some optical properties are explored:

When light travels through a medium, it looses intensity depending on the optical properties of the medium μ and the distance z travelled. The Intensity follows the Lambert-Beer law:

$$I(z) = I_0 \exp(-\mu z) \tag{1.54}$$

μ is called the attenuation coefficient. The attenuation is caused by absorption and reflection inside the material caused by spatial heterogeneities of the refractive index. [30] Reflections can be specular, meaning that an incident wave is reflected from a flat surface, [31] or diffuse, when the object is composed of rough surfaces and index gradients. [32]
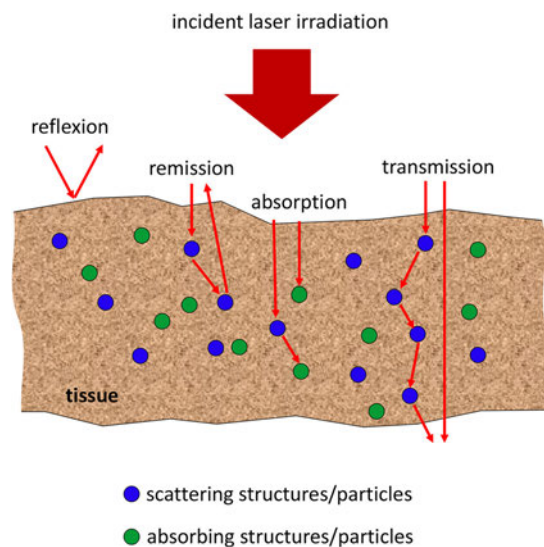
Figure 1.14: Overview of the different possible pathways for a single photon. The figure is taken from [33]

Reflections from such objects are known as elastic scattering. There exist mainly two types of elastic scattering: Mie scattering, which comes from objects comparable or larger than the wavelength of light, and Rayleigh scattering, which is caused by atoms, molecules and objects smaller than the wavelength of light.

One should note, that per definition, Mie scattering is the generic name for scattering by a sphere of any size, both small and large, and the common term Rayleigh scattering refers to the Rayleigh limit of Mie scattering due to particles much smaller than the wavelength of light. [34]
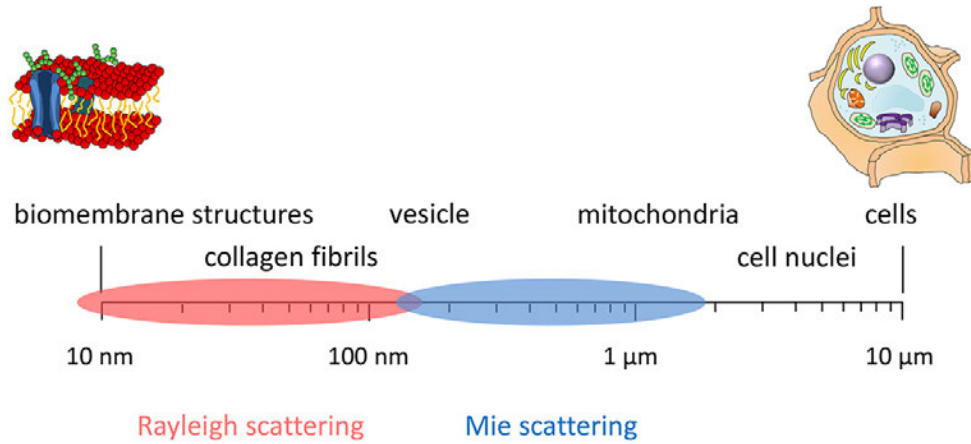
Figure 1.15: Rayleigh and Mie scattering regime, and biological examples on the same scale. The figure is taken from [33]

After these considerations, the attenuation coefficient can be written as the sum of the absorption coefficient and the scattering coefficient:

$$\mu = \mu_a + \mu_s .\tag{1.55}$$

with the scattering coefficient μ_s being the inverse of the mean free path between scattering events, and the absorption coefficient μ_s being the inverse of the mean free path before a photon is absorbed.

Characteristic for different types of materials is the typical angle at which the scattering happens. One can divide the scattering angles at 90° and define two terms: A photon is forward scattered or transmitted, when the deflection angle is smaller than 90°. If it is larger, the photon gets backscattered or remissed. This can be encoded in the scattering anisotropy g, which is the cos of the expected scattering angle. Therefore, the value of g lies in a range of -1 for totally backscattered, 0 for 90° deflection, and 1 for undeflected forward scatter.

In general, Mie scattering is mostly directed forwards, while Rayleigh scattering shows an isotropic distribution. [35]
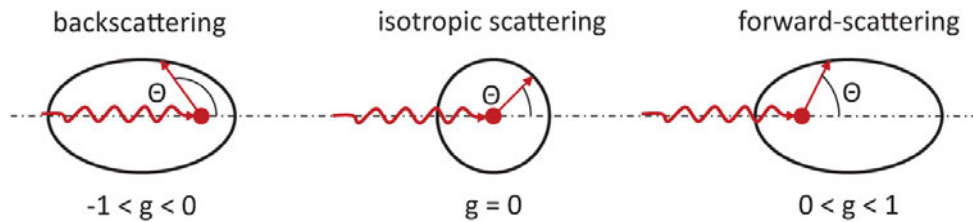
Figure 1.16: Illustration of the probability density for backscattering, isotropic scattering and forward-scattering. The figure is taken from [33]

In literature, two alternative definitions are used to describe the variables presented above: The first is the penetration depth, which is defined as the depth at which the light is attenuated to e^{-1} of its original value. The penetration depth relates to the attenuation coefficient in the following way:

$$p = \frac{1}{\mu} .\tag{1.56}$$

One should be aware that the physical quantities above are sometime defined in terms of field quantities, not power. However, this is not common in biomedical optics. [36]

The other definition found frequently in literature is termed reduced scattering coefficient μ'_s, which combines the scattering coefficient and the scattering anisotropy in one value. The idea is to express the anisotropic scattering probability distribution by a reduced isotropic distribution $(1 - g)$, to which a value of g is added in the direction of the incident beam. [30]

$$\mu'_s = \mu_s(1 - g) .\tag{1.57}$$

17

The reduced scattering coefficient thereby describes the diffusion of photons in a random walk of step size of $1/\mu'_s$ where each step involves isotropic scattering absorption coefficient μ_a, how much light is absorbed over a given propagation length.

As one probably has observed, biological tissue is highly non-transparent. However, when shining with a bright light towards your hand or the eyelid, one can see that a diffuse red shine is penetrating the tissue. This already tells two important properties: First, biological tissue has a high forward scattering coefficient compared to its absorption coefficient. A medium showing this characteristic is often termed as being in the diffuse regime. This way, the light gets highly diffused and thereby looses all image information, but is still able to pass through the tissue. Second, biological tissue is more transparent towards the red side of the optical spectrum, hence the red shine. In fact, all quantities discussed here are highly wavelength dependent, and the far red and near infrared region mark the optical window for tissue imaging between the absorption bands of hemoglobin at 550 nm and water at 1000 nm. [32]

To quantify these statements, some literature reported value ranges are given for grey and white matter, and for skin tissue and water for reference, all at a wavelength of $630 - 640$ nm:

tissue	μ_a [mm^{-1}]	μ_s [mm^{-1}]	g	μ'_s [mm^{-1}]	d [mm]	references
white matter	0.08 - 0.15	38.6 - 40.9	0.84 - 0.97	5.4 - 6.5	0.63 - 0.79	[37, 38]
gray matter	0.14 - 0.2	9 - 47.3	0.5 - 0.9	0.99 - 3.31	0.83 - 4.06	[37, 39]
skin	0.015 - 0.03		0.5-0.7	1 - 1.5		[40]
water	0.3×10^{-3}	0.002×10^{-3}				[41]

Table 1.2: Literature values for the scattering and absorption characteristic of white and gray matter as well as skin tissue and water.

It is immediately obvious, that brain tissue, especially white matter, is characterized by higher values for scattering and absorption compared to all other materials shown here. There are various explanations, which will be summarized here: First, the forward scattering of biological tissue in general and especially in brain white matter tissue implies a significant amount of Mie scattering. Objects large enough to fall into the Mie regime are Axon cross sections, which are highly abundant in white matter tissue. Even though also the cell bodies of the gray matter tissue fulfill the criterion to cause Mie scattering, their larger size implies a lower number in a given tissue volume, therefore reducing the amount of scattering. [32]. The number of mitochondria was shown to be higher in gray matter areas [42]. As mitochondria feature a very large amount of double lipid membrane due to their high surface area, larger amounts of Rayleigh scattering should occur in gray matter and general in brain tissue [43], which is also reflected in the table. A predominant structure in skin tissue is the periodic density of collagen fibers of 70 nm and the spacing between the fibers. Both structures should increase the amount of Rayleight scatter. However, it is still a large forward portion reported for skin tissue, possibly due to a larger amount of scattering from the larger sized nuclei. [34] Interestingly, the absorption coefficient in brain white matter tissue is higher compared to gray matter, despite the darker appearance of gray matter. [37]

In general, brain tissue can be said to be a high scattering medium due to the highly complex and diverse composition of different cell structures, such as axons, dendrides, glia and the whole neuropil, and different media having different refractive indices, such as the fatty tissue of the myelin sheath compared to the aqueous cytoplasma.

1.8 Bruchpilot as one component of active zones

Superresolution microscopy has revolutionized the findings about AZ by enabling to visualize these structures measuring only a few hundred nanometers in diameter. That is why the characterization of AZ components as well as the AZ patterning was subject of intensive investigation in the past decade.
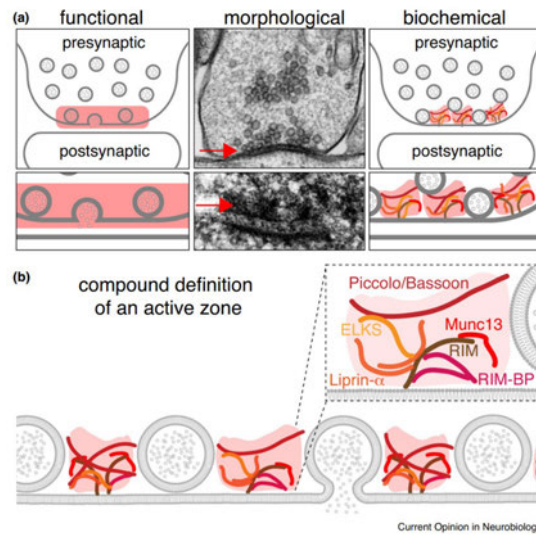
Figure 1.17: Morphology and assembly of prominent proteins in an AZ. Figure taken from [44].

The presynaptic active zones are morphologically characterized (first) in electron microscopy by membrane thickenings close to synaptic vesicle accumulations (see Figure 1.17). They consist of multiple proteins enabling exocytosis to target signals toward postsynaptic receptors. These proteins comprise Munc13, Bassoon/Piccolo (which are assumed to organize the structural formation and maintenance of the AZ), RIM (Rab3a-interacting molecule), Liprin-α, ELKS/CAST/ERC and RIM-BP [44].

Bruchpilot (brp) is a AZ protein homologue to the human AZ protein ELKS/CAST/ERC intensively investigated in drosophila, especially in the *Drosophila melanogaster* neuromuscular junction. [45] Structurally, it is a coiled-coil rich protein of nearly 200 kD [45]. Its position is in the dense projections of the active zones, also called T-bars, oriented with the N terminus closer to the AZ membrane than its C-terminus [46]. The latter resembles multi-functional cytoskeletal proteins. Brp plays a role in clustering Ca_2^+ channels [46]. Mutants of brp show a loss of T-bars at AZs and functional restriction in locomotor activity and stable flight [45]. Thereby, the name Bruchpilot is explained as it stands for "crash pilot".

All in all, the exact regulation of neurotransmitter release is crucial for higher neuronal functions including learning, memory and cognition [45].

Chapter 2

Materials and Methods

2.1 Materials

2.1.1 Nikon Ti Eclipse inverted research microscope

The Nikon Ti-Eclipse (Ti-E) microscope body was chosen, which is an infinity-corrected inverted research microscope. [47] Nikon uses two tube lenses in the body, one at 200 mm, one at 250 mm focal length, which gives (in multiplication with the magnification of the objective) a $1\times$ or $1.5\times$ magnification. The present version has three ports to couple to illumination or detection paths, one on each side and one at the back. A halogen-based fully-configurable lamp is located above the xy-stage. The stage is motorized and allows the use of multiple sample holders. The body features a motorized objective mount with attached perfect focus system (PFS), an infrared-laser-based system which moves the objective in z-direction to correct for axial drift and keeps the focal plane in the sample steady.

Objective and filter turrets are both motorized and software-controlled.

2.1.2 Objectives

objective	manufacturer	magnification	NA	immersion	refractive index	working distance[1]	catalog	location of Fourier plane[2]
APO TIRF	Nikon	100×	1.49	oil	1.52	0.09-0.16	MRD01991	48.0
SR HP Plan APO λ	Nikon	100×	1.35	silicone oil	1.4	0.28-0.31	MRD73950	47.3

Table 2.1: Specifications of the objectives used in the setup

[1] values taken from [48]
[2] above the objective shoulder. [49]

2.1.3 Lasers

name	wavelength	manufacturer	laser power [mW]
gem 640	640	Laserquantum	550
iBeamSmart 488 S HP	488	Toptica	200

Table 2.2: Specifications of the lasers used in the setup

2.1.4 Fluorescent microspheres

short	⌀ [μm]	Ex nm	Em nm	manufacturer	Full name	catalog	reference
FC6	6	505/560/660	515/580/680	ThermoFisher Scientific	FocalCheck™	F14806	[50]
FS4	4	505	515	ThermoFisher Scientific	FluoSpheres™ Sulfate	F8859	[51]
CR1	1	625	645	ThermoFisher Scientific	FluoSpheres™ Carboxylate-Modified Crimson	F8816	[52]
TS01	0.1	360/505/560/660	430/515/580/680	ThermoFisher Scientific	TetraSpeck™	T7279	[53]

Table 2.3: Specifications of the fluorescent microspheres tested for direct wavefront measurements

The excitation and emission spectra of the TS01 and the FS4 beads and the laser lines are plotted in Figure 3.8.

2.1.5 Wavefront sensor and Deformable mirror

name	WFS30-7AR/M
manufacturer	Thorlabs
type	Shack-Hartmann wavefront sensor
microlens array name	MLA 150-7AR
microlens aperture	11.5×7.5 mm
number of microlenses	73×45
microlens pitch	150 µm
microlens diameter	146 µm
sensor type	CMOS
resolution	1936×1216 px
pixel size	5.83 mm^2

Table 2.4: Specifications of the wavefront sensor used in the setup

name	DMP 40/M-P01
manufacturer	Thorlabs
type	piezoelectric deformable mirror
number of actuators	40
coating	protected silver
reflectance (450 – 2000 nm)	> 97.5 %
voltage range per segment	0 – 200 V

Table 2.5: Specifications of the deformable mirror used in the setup

2.1.6 Camera

name	Andor Sona 4.2B-11
manufacturer	Oxford Instruments
sensor type	back-illuminated sCMOS
sensor size	22.5×22.5 mm
resolution	2048×2048 px
pixel size	11 µm
bit depth	16

Table 2.6: Specifications of the camera used in the setup

2.1.7 Filters

function	name	ID	manufacturer	λ cut-on / cut-off [nm]
dichroic	zt405/488/561/640rpc flat	F73-410 T3	Chroma	405/488/561/640
dichroic	T635LPXR	F48-636	Chroma	635
dichroic	BLP01-647R-25	F76-649	Semrock	647

Table 2.7: Specifications of the filters used in the setup

2.1.8 Optics and optomechanics

name	function	manufacturer	focal length [mm]	lens type	diameter [mm]
AC050-008-A-ML	excitation beam	Thorlabs	7.5	achromatic doublet	5
AC508-150A-ML	excitation beam	Thorlabs	150	achromatic doublet	50.8
AC508-750A-ML	field lens	Thorlabs	750	achromatic doublet	50.8
AC254-250-A-ML	WFS relay	Thorlabs	250	achromatic doublet	25.4
AC254-300-A-ML	WFS relay	Thorlabs	300	achromatic doublet	25.4
AC508-300-A-ML	relay lens	Thorlabs	300	achromatic doublet	50.8
AC508-600-A-ML	imaging lens	Thorlabs	600	achromatic doublet	50.8

Table 2.8: Specifications of the lenses used in the setup

name	function	manufacturer	mirror type	reflective band nm	diameter [mm]
BB1-EO2	folding mirror / excitation path	Thorlabs	dielectric mirror	400-750	50.5

Table 2.9: Specifications of the mirrors used in the setup

name	type	function/location	manufacturer
LM2XY/M	XY translation lens mount	excitation path	Thorlabs
KCB2C/M	tip-tilt cage mount	excitation path	Thorlabs
CXY1	XY translation cage mount	WFS beam relay	Thorlabs
SM1D12SZ	iris aperture	WFS aperture	Thorlabs
KC1-T/M	tip-tilt cage mount	WFS mount	Thorlabs
CXY2	XY translation cage mount	imaging lens mount	Thorlabs
SM2M35	lens tube	camera mount	Thorlabs
SM2NFM2	Nikon F-Mount adapter	camera mount	Thorlabs
KM100CP/M	tip-tilt mount	folding mirror mount	Thorlabs
-	50.8 mm to 25.4 mm adapter	folding mirror mount	custom build
B4CRP/M	filter cube rotation platform	beam splitting	Thorlabs
M-460A-XY	XY linear stage	folding mirror and filter cube mount	Newport
KM100PM/M	tip-tilt mount	DM mount	Thorlabs

Table 2.10: Specifications of the optomechanical parts used in the setup.

2.1.9 Other physical components

name	type	specifications	manufacturer
CPS532	Laser pointer	532 nm, 4.6 mW	Thorlabs
SI100	Shearing plate interferometer	5 – 10 mm beam diameter	Thorlabs
PM100D	Digital optical power meter		Thorlabs
S120C	Photodiode power sensor		Thorlabs
M625L4	single-color mounted LED	625 nm, 770 mW	Thorlabs
COP5-A	LED collimation lens		Thorlabs

Table 2.11: Specifications of other components used in the setup

2.1.10 Reagents

reagent	manufacturer	order number
PBS	Sigma-Aldrich	D1408
glutaraldehyde	Sigma-Aldrich	G5882
Triton X-100	ThermoFischer	28314
bovine serum albumin (BSA)	Sigma-Aldrich	A3983
coverglass	Carl Roth	LH23.1
formaldehyde	Sigma-Aldrich	F8775
rabbit anti-α-tubulin	ThermoFischer	A11126
goat anti rabbit Alexa Fluor 647	ThermoFischer	A27040
β-mercaptoethylamine (MEA)	Sigma-Aldrich	M6500
Potassium hydroxide	Sigma-Aldrich	60377
Poly-D-Lysine (PDL)	Sigma-Aldrich	P6407
carbonate-bicarbonate-buffer (CB)		
sodium borohydrate NaBH$_4$		

Table 2.12: Specifications of reagents used in the setup

2.1.11 Biological samples

Three different biological specimens were used in this thesis. The preparation is Primary hippocampal neurons were prepared from C57BL/6 E18 embryos and provided by Dr. Christian Werner.

To introduce the aberrations to the tubulin sample, unstained coronal murine brain slices were placed between the sample and the microscope objective. The unstained brain slices came from male C57BL/6 mice.

The Brp-stained coronal brain tissue samples used in this theses came from worker honeybees (*Apis mellifera*). Brp-stained honeybee brain tissue samples were thankfully provided by the Group of Professor Rösler, Biocenter, University Würzburg.

2.2 Methods

2.2.1 Software used throughout the experiments

During the course of the thesis, several different programs were used for hardware setup and control, but also aiding to create this thesis:

Optic design software   To give an approximate position to where the optical components, meaning lenses, camera, WFS, etc. need to be placed, two different programs were used. First, the freeware `WinLens 3D` [54] from Quioptic was used to explore the lack of telecentricity in the setup and create the idea for the use of a field lens. However, the software does provide some difficulties when trying to analyse custom lens designs such as the tube lens of the Nikon Ti-E. To model the whole microscope setup in software, find the optimal placement and focal length of the field lens and lay out the position of all other components, the more feature-rich optic design software `Zemax Optic Studio` [54] was thankfully provided by the chair.

The objective was approximated with a thin lens having a focal length of 2 mm (see 1.1.3), surrounded by an aperture of 5.96 mm [49]. Two point sources were located in the front focal plane of the lens, one centrally, one at a °6 angle, thereby forming the same rays as a proper objective would. The distance between the objective lens and the tube lens was set to 150 mm. This value is based on caliper measurements $((150 \pm 10)$ mm) of the distance between the nose piece of the microscope, which corresponds to the objective shoulder, and the surface of the tube lens, as well as on values for the location of the back focal plane of the objectives, thankfully provided by Dr. Martin Kiesel [49] from Nikon Corp. Shown in Figure 2.1A, the setup was modeled without the field lens. The diverging rays between L_T and L_1, as well as the back shift of the Fourier plane can be seen. Then, a 750 mm field lens was inserted exactly 200 mm behind the tube lens in the first image plane of the microscope. The lens recovers the telecentricity and moves the Fourier plane back to the focal point of the Fourier transforming lens.
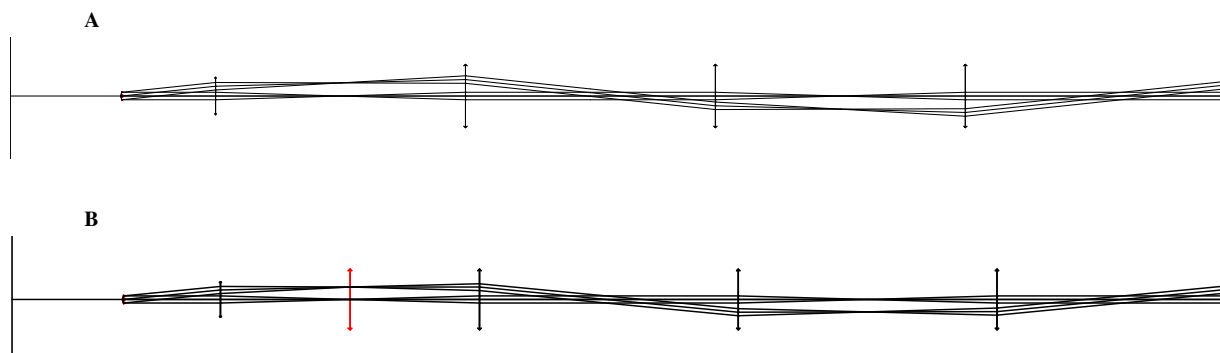
Figure 2.1: Comparison of the setup with field lens and without field lens using ray tracing analysis. **A** The system without field lens. One can see how the beams diverge behind the tube lens, which causes the Fourier plane to form further back for the remote ray bundle. **B** The same setup with the same lenses, but an additional field lens in the first image plane.

The field lens bends the remote ray bundle inwards, thereby moving the Fourier plane back to the focal point of the lens L_1.

As WinLens3D uses ideal lenses to model the beam paths, Zemax Optic Studio was used to model the setup using physical lenses.

Using Zemax, the positioning of the optical components was optimized and then the measurements for the placement of the component on the optical table were derived. [55]

Hardware control   The Nikon Ti-E is controlled by Nikons own `NIS Elements` software. [56] The software manages the microscopes stage, objective and filter turrets, port selection, and it communicates with the Andor SONA camera. The software was used to set up all imaging experiments.

The lasers were controlled by their manufacturer provided software. For the Toptica Photonics Lasers the software is named `iBeam smart` [57], for the Laser Quantum laser the software is called `Remote Laser Control v1.0`. [58] Both programs were used to manage the shutter and laser power output.

The software to control the DM and the WFS were provided by Thorlabs and both used in their latest versions at the time of the experiment, that is Version 3.1 [59] and Version 5.4 [60], respectively.

Writing   The thesis was compiled in the `miktex` distribution of LATEX, using `Sublime Text 3` as the text editor software. [61]

Figures   All graphs including the wavefront plots, histograms and scatter plots were plotted using the open-source command-line tool `Gnuplot 5.0 patchlevel 4`. [62] Gnuplot was integrated into the LATEX code to match the document font using the `gnuplottex` package. Post-processing of the camera images including stacks and timelapses were performed using the `FiJi` distribution of `ImageJ 1.53c` [63] For the *d*STORM image, the open-source deconvolution software `rapidSTORM 3` was used. [64] Two-dimensional sketches were drawn as vector graphics in `Inkscape 0.92.5` and exported as eps file plus latex code for the annotations. [65] The figures were integrated using the `epstopdf` package. The three-dimensional sketch of the artificial Tubulin sample was drawn in Paint3D.

2.2.2   Sample preparations

α-tubulin immuno-staining of primary murine hippocampal neuron cell culture   The preparation of the brains was done by Dr. Christian Werner and is documented in [66]. Two buffer solutions were prepared: CB1 buffer consists of 0.3 % glutaraldehyde (GA), 0.25 % Triton X-100 in CB-buffer. CB2 contains 2 % GA in CB. First, the cells were permeabilized for 60 s using the CB1 buffer. The buffer was then exchanged with the CB2 buffer for fixation for 10 min. The fixation was stopped by washing the cells 3 × in PBS. To reduce background, the cells were then submerged in 0.1 % sodium borohydrate $NaBH_4$ for 7 min. Afterwards the cells were washed again 3 × in PBS. In the next step, unspecific binding was prevented by blocking with 5 % bovine serum albumin (BSA) for 30 min.

For staining, the primary antibody was diluted at $10\,\mu g\,mL^{-1}$ in 5 % BSA and pipetted on parafilm. The cover glass was then placed on the drop with the cells facing down for 60 min at room temperature. After that, the cells were washed 3 × with PBS. For the primary antibody, a rabbit anti-α-tubulin was used.

The secondary antibody was applied in the exact same way and concentration as the primary antibody. Here, a goat anti rabbit Alexa Fluor 647 antibody was used.

Last, a post fixation step is done with 4 % formaldehyde in PBS for 10 min and then washed 1 × with PBS before imaging.

Samples were stored on PDL-coated 18 mm round cover slips at 4° for up to 7 days.

Bruchpilot immuno-staining of honeybee brain tissue sections   For the preparation and staining procedure with anti-BRP antibody, see [46]. Samples were stored at 4° for up to 7 days.

Preparation of murine brain tissue sections   The brains were cryo-cut in the coronal plane to $100\,\mu m$ thickness. The preparation of the brains is documented in [66]. Brain slices were stored at $-80°$ on PDL-coated 18 mm round cover slips until use.

Switching buffer   The switching buffer solution for the *d*STORM image consists of 100 mmol β-mercaptoethylamine (MEA) in PBS, adjusted to PH 7.5 using potassium hydroxide (KOH).

Artificial brain slice sample preparation   To act as an diffusion layer, a $100\,\mu m$ murine brain slice was mounted on a $(170 \pm 5)\,\mu m$ high-precision cover glass. On top of the slice, a bead solution was pipetted containing 100 nm TS01 beads and $4\,\mu m$ FS4 beads. To let the beads settle, the sample was placed at 4° for 30 min. Then, a α-tubulin stained hippocampal neuron culture was mounted directly on top of the slice and covered with another cover glass. The sample shows the following structure:
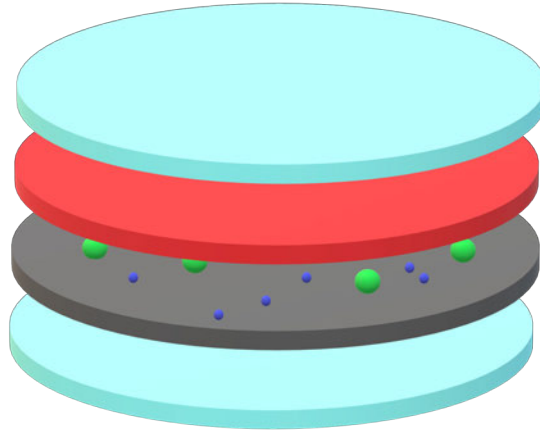
Figure 2.2: Structure of the sample. The top and bottom layers shown in light blue are coverglass. The tubulin-stained cell hippocampal culture is shown in red. The dark grey layer is the unstained brain slice. Large 4 μm FS4 beads (green) and smaller 100 nm TS01 beads (dark blue) sit between the cell culture and the brain slice.

Using this approach, the light coming from the fluorophores at the tubulin straints must travel through the 100 μm murine brain slice to reach the objective. The brain tissue acts as a diffusion layer and causes aberration due to the internal density variations.

2.2.3 Microscope calibrations

Determination of the camera pixel size   After the setup has reached its final form (Figure 3.12, the theoretical pixel size was verified experimentally. A 400 LP/mm line grating was placed on the stage and illuminated by the halogen lamp. The image was then Fourier transformed to determine the frequency with the highest magnitude, $f[\mathrm{px}^{-1}] = 0.0217\,\mathrm{px}^{-1}$. (px: pixel) The inverse of $f[\mathrm{px}^{-1}]^{-1} = b[\mathrm{px}] = 46.05\,\mathrm{px}$ was then compared to the $b[\mathrm{nm}] = 2500\,\mathrm{nm}$ resulting from the 400 LP/mm line spacing.

$$\mathrm{pixelsize} = \frac{2500\,\mathrm{nm}}{46.05\,\mathrm{px}}$$
$$= 54.3\,\mathrm{nm\,px}^{-1} \ . \tag{2.1}$$

This value was used throughout the experiment.

To verify the calculation, the pixel size was estimated using the size and resolution of the camera sensor. The sensor has a $22.5\,\mathrm{mm} \times 22.5\,\mathrm{mm}$ sensor size and a resolution of $2048\,\mathrm{px} \times 2048\,\mathrm{px}$. Taking the $100\times$ magnification of the objective and the $2\times$ magnification of the image relay into consideration, an optimally filled full frame image in image space captures a field of view (FOV) in object space of $112.5\,\mu\mathrm{m}$. This translates to a pixel size of

$$\mathrm{pixelsize}_{\mathrm{estimated}} = \frac{112.5\,\mu\mathrm{m}}{2048\,\mathrm{px}}$$
$$= 54.9\,\mathrm{nm\,px}^{-1} \ , \tag{2.2}$$

nearly matching the experimentally determined pixel size.

Calibration of the Zernike numbers of a captured wavefront for the calculation of feedback parameters for the deformable mirror   To obtain the parameters γ_i, the Zernike coefficients of TS01 beads were measured by the WFS. The same coefficients were then manipulated on the DM until the WFS showed a fully flat WF. The coefficients of the WFS before the correction were then compared to the coefficients of the DM after the correction to derive the individual γ_i:

$$\gamma_i = \frac{Z_{\mathrm{WFS}}^i}{Z_{\mathrm{DM}}^i} \ , \tag{2.3}$$

i standing for the Zernike numbers. The parameters were averaged after measuring and manually correcting ten individual beads. The following table shows the set obtained and the resulting γ_i:

Zernike number	Z_{WFS}	Z_{DM}	γ_i
4	0.05	-0.08	-0.625
5	0.55	-0.18	-3.06
6	0.01	0.03	0.33
7	0.05	-0.03	-1.67
8	0.07	0.01	7.00
9	0.23	0.35	0.66
10	0.01	-0.03	-0.33
11	0.01	0.01	1.00
12	0.03	0.01	3.00
13	0.19	-0.54	-0.35
14	0.06	-0.01	-6.00
15	0.02	0.01	2.00

Table 2.13: Example of the individual γ_i obtained for the manual correction of the PSF in Figure 3.13

Z2 and Z3 represent tip and tilt, which was not corrected for.

2.2.4 Correction procedure

To correct the image, first a 4 μm FS4 bead was focused using the 488 nm laser only and moved to a predefined location to the left of the frame to pass the aperture in the image plane in front of the WFS. Usually, the beads are bright enough to see the image of the bead on the aperture. The aperture blocks all light coming from other sources (eg. another bead) but the chosen bead thereby ensures a defined wavefront. To find the optimal focal point, the wavefront of the FS4 beads was measured and the focus was moved until the defocus shown by the WFS was minimized. The wavefront including the Zernike numbers was captured.

Next, the Zernike polynomials measured by the WFS were translated to the arbitrary scale of the Zernike polynomials on the DM using the equation given in 2.2.3. The individual parameters γ_i were derived empirically and depend on the beam paths in the system and the exact position and orientation of all the optical components as well as the DM and the WFS. The Thorlabs Deformable Mirror Software features an automatic determination of the individual parameters, [59] however, by the time of finishing the last experiments, the control loop determination did not return any values. In the next step, the scaled Zernike coefficients were applied to the DM to correct the image. After the first correction step, the TS01 beads should be visible to enable further manual correction. Finally, the manual step is introduced to further increase the correction by first minimizing the residual Zernike coefficients on the WFS by eye. Mainly Z8 and Z9 (coma) as well as Z7 and Z10 (trefoil) can be used to make the PSF symmetrical in the xy-plane, while Z5 (defocus) and Z13 (spherical aberration) as well as Z6 (astigmatism) can improve the symmetry in the z-direction. In a perfectly aligned system, all Zernike Polynomials would be independent from each other. However, when the optical system is not optimally aligned, coefficients encoding partially similar patterns (eg. defocus and spherical aberration) can not be controlled independent from each other. Therefore, in a last step, the image was magnified and the residual coefficients were distributed until the image appeared to have the maximum sharpness and contrast. However, the last change was not significant and often not distinguishable from the image without the manual distribution.

Chapter 3

Results and Discussion

The work was divided into three different phases. In the first section (3.1), the adaptive optics system was quantified. Then, (3.2), a widefield illumination microscope was built around the DM and the WFS. In general, the result of this work is focused on the developmental stages of the microscope and adaptive optics system. However, two examples (Section 3.3), are presented to give an approximate reference point for the abilities of the system in a scientific use-case.

3.1 Pretesting of the Wavefront Sensor and the Deformable Mirror

Both, WFS and DM were tested to ensure critical operation parameters were met and the feedback loop was functional.

3.1.1 Test of the low light capabilities of the WFS for integration in fluorescent microscopes

LED illumination To test the ability of the WFS to operate in low-light conditions, a test setup was build using an 770 mW 625 nm LED as a light source together with a collimator lens L_K and two 1:1 beam expanders ($f_{L_1} = f_{L_2} = f_{L_3} = f_{L_4} = 100$ mm), as shown in Figure 3.1A.
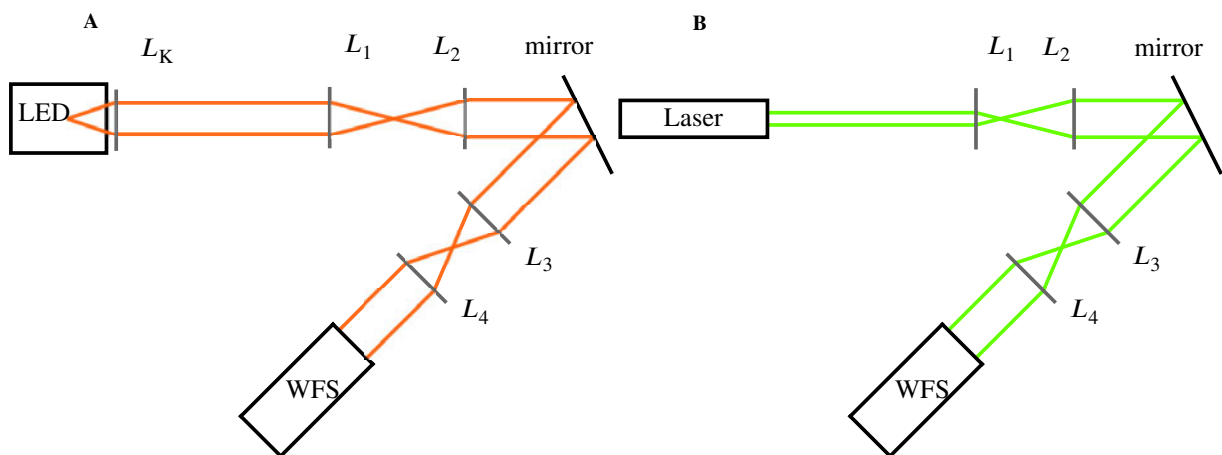

Figure 3.1: Temporary setups to directly illuminate the WFS to test its sensitivity. **A** A 625 nm 770 mW LED together with a collimating lens L_K is used as a light source. **B** The LED and collimator is replaced by a 532 nm 4.6 mW laser to test a different source type and reduce the beam power.

The light of the LED was dimmed continuously with continuous optical density (OD) filter wheels, which were placed directly in front of the WFS, and the light level at which the sensor could not capture a stable image was determined. When dimming the light, the camera increased the frame time automatically to increase the photon count. At an integration time of around 1 s for the lowest light level tested, the centroid detection failed and the wavefront was not calculated correctly. The OD of 4 was recorded. Following the conversion from OD to transmission T

from [3]

$$T = 10^{-\mathrm{OD}} \ , \tag{3.1}$$

the image disappeared at a transmission of $T = 10^{-(2+2+2+2)} = 10^{-8}$. This translates to a beam power of

$$I_{\mathrm{LED}} = 10^{-8} \times 770\,\mathrm{mW} = 7.7\,\mathrm{nW} \ , \tag{3.2}$$

not accounting for losses at the lenses. The typical transmission of lenses made of N-BK7 glass (exclusively used) is over 90 %. Given the small number of optical elements used in the temporary setups, loss at the lenses is assumed to not change the magnitude of the results.

Using a power meter for reference, the beam power was measured to be approximately 5 nW. No exact number is given, because the value reaches the lower sensitivity limit of the unit of 1 nW and a highly fluctuating output was encountered. The value of 5 nW was calculated as the mean value of 5 measurements.

Laser illumination The same experiment was repeated using a 4.6 mW 532 nm laser pointer using a 3:5 ($f_{L_1} = 60\,\mathrm{mm}$, $f_{L_2} = 100\,\mathrm{mm}$) and a 1:1 ($f_{L_3} = f_{L_4} = 100\,\mathrm{mm}$) beam expander and the same filter wheels, as shown in Figure 3.1B. Here, the image disappeared after three OD2 filters, resulting in a transmission of $T = 10^{-(2+2+2)} = 10^{-6}$. The power at the sensor was therefore calculated to be

$$I_{\mathrm{laser\ pointer}} = 10^{-6} \times 4.6\,\mathrm{mW} = 4.6\,\mathrm{nW} \ . \tag{3.3}$$

Again, the power output was checked with the power meter, measuring approximately 3.5 nW. Again an average of 5 measurements was used.

The power was translated to photon count, assuming the Energy $E_{\gamma@640\,\mathrm{nm}}$ of a single photon at a wavelength of 640 nm is

$$E_{\gamma@640\,\mathrm{nm}} = \frac{hc}{\lambda} \tag{3.4}$$

$$= 3.104 \times 10^{-19}\,\mathrm{J} \ . \tag{3.5}$$

Therefore:

$$5\,\mathrm{nW} = 5 \times 10^{-9}\,\mathrm{W} \tag{3.6}$$

$$\approx 1.6 \times 10^{10}\,\frac{\mathrm{E}_{\gamma@640\,\mathrm{nm}}}{\mathrm{s}} \ . \tag{3.7}$$

This indicates that the WFS is capable of detecting approximately 1.6×10^{10} photons per second as the lower level. For comparison, the expected scale of radiant flux of an immuno-labeled sample must be estimated. It depends on the number of exciting photons from the excitation light, the number of fluorophores available at the sample, which depend on the labeling procedure and the target quality, the properties of the fluorophore, namely the chance to absorb an exciting photon, which is called molar extinction, and the ratio of the absorbed to emitted photons of each fluorophore, which is called quantum yield. [67]. Derived solely from the length of the list of parameters, one can imagine that the radiant flux of a sample is highly variable depending of the scientific question, and can not easily be estimated. [67]. However, using random samples used for dSTORM applications, the photon count at the camera was evaluated and found to be consistently some orders of magnitude higher than the limit of the WFS. However, the nearly flat wavefront coming from a single point-like light sources is not fully comparable to an aberrated wavefront emerging from multiple sources on a biological sample. Also, the camera used in the setup is theoretically capable of single-photon detection [8], which is clearly out of range for wavefront correction using the investigated WFS.

3.1.2 Pretesting the deformable mirror for beam collimation and focusing characteristics

The DM was tested to ensure that the surface is flat and does not induce any aberration coming from an intrinsic shape in its resting position. For the mirror to be in the resting position, a voltage of 200 V is applied to all segments via software. [6] A laser beam was expanded by two lenses ($f_1 = 25\,\mathrm{mm}$, $f_2 = 200\,\mathrm{mm}$) and limited by an aperture stop to cut off edge effects from the lenses and meet the aperture diameter of the DM. Collimation was checked carefully using a shearing plate interferometer. The expanded beam was pointed directly to the DM in a small angle, [68] and the reflection was again measured with the shearing plate interferometer.
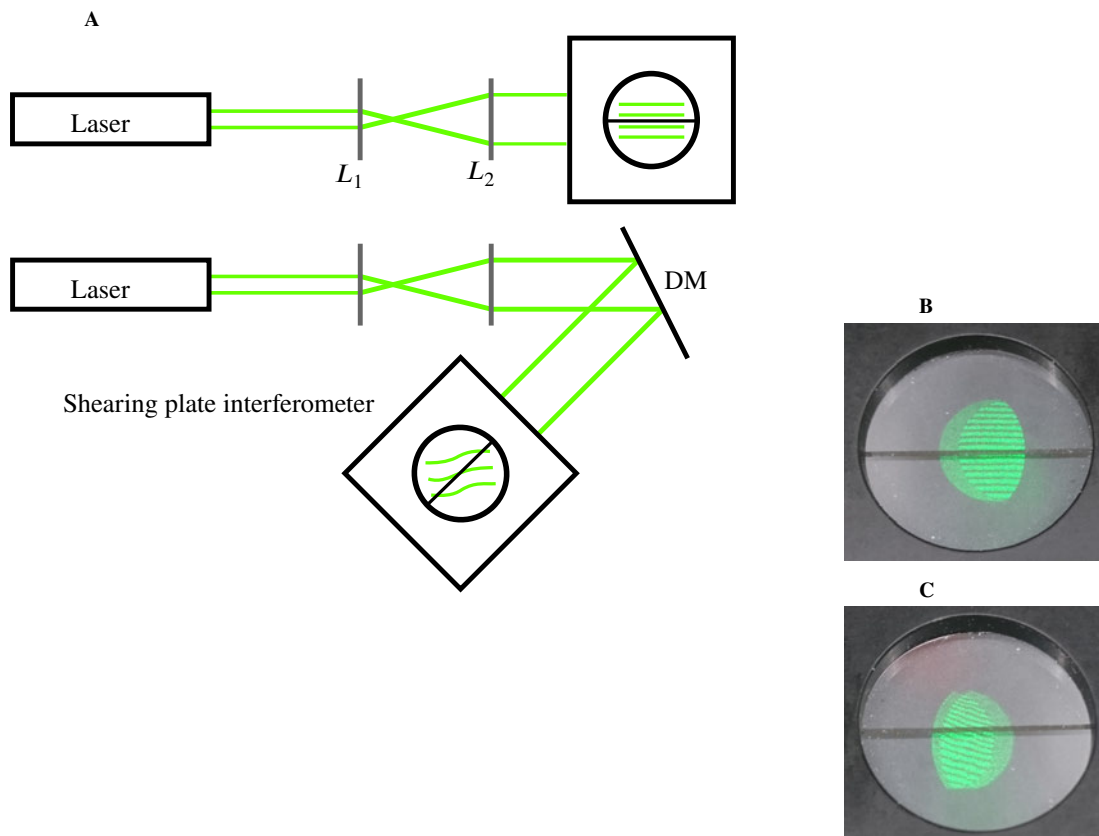
Figure 3.2: A 532 nm Laser, 1:8 beam expander and shearing plate interferometer. The laser wavelength is not critical, as the DM is a reflective element and therefore its operation is not spectrally dependent. **B** Shearing plate interferometer after the beam expander and after the DM.

Figure 3.2 shows that the DM slightly collimates the light. This should not happen, as these mirrors are usually factory calibrated to have a plain surface at 200 V. A possible explanation would be creeping of the piezoelectric elements, because the mirror in its off-state is in a concave shape. As such, creeping was reduced by a full voltage sweep before every measurement. [6] Even though the he unevenness could not be removed, it was compensated for and made fully operational by moving the subsystem of Fourier transforming lens and DM closer to the microscope body, such that the DM has a diverging incoming and a collimated outgoing beam. [69]

The wavefront was also measured with the FWS and found to be flat ($r = 0.02$) when removing the defocus. One should note, that the laser wavelength is not critical for the result, as the DM is a reflective rather that refractive element and therefore its operation is not spectrally dependent.

3.1.3 Integration of the DM and WFS into the *d*STORM setup for direct laser light wavefront correction

Both, the DM and the WFS were then placed in the existing *d*STORM microscope, as described in sections 1.4.1,1.5.2. The objective was removed and a dielectric broadband mirror was screwed into the objective mount. By expanding a laser, a parallel beam was fed into the microscope body and was reflected by the mirror, replicating the emission light coming from a single emitter above the objective. The emission filter was removed to enable the laser to be passed through to the imaging ports. In addition to the mirror in the objective mount, a foldable mirror was used in front of the imaging lens to direct the light onto a beam expander and subsequently onto the WFS. The setup is sketched in Figure 3.3.
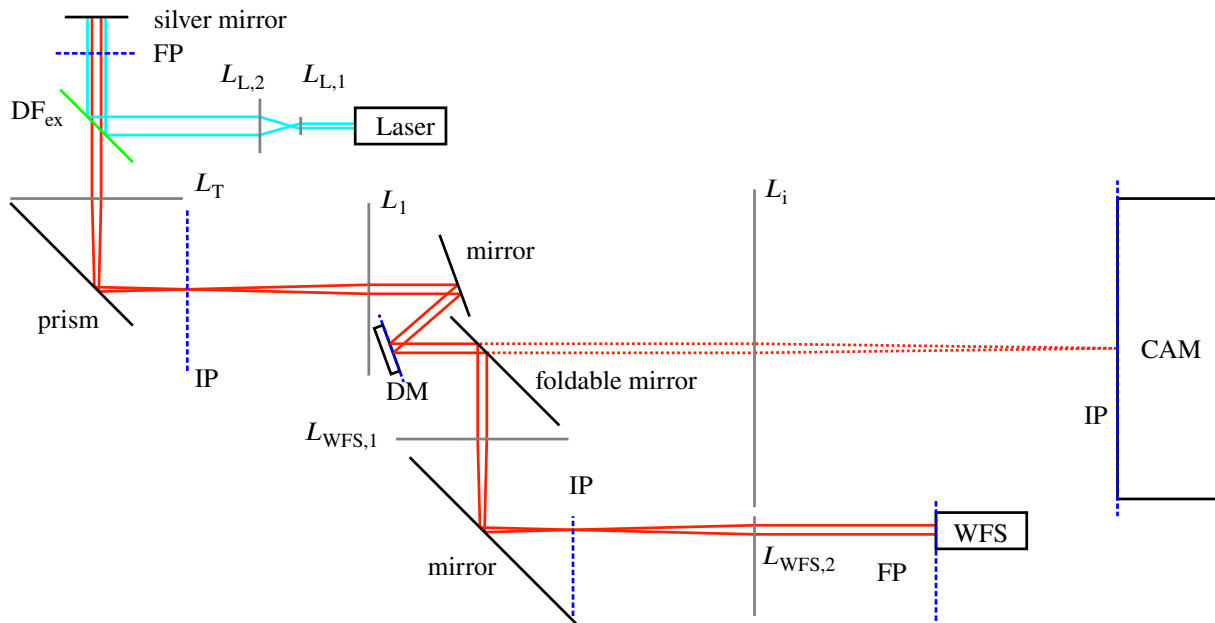
Figure 3.3: WFS placement and beam paths in the microscope. Mirror to imitate the objective. The dichroic filter is placed before the imaging lens in a parallel beam section. To create a Fourier plane for the WFS, two additional lenses are needed. Also, the aberrations created by the imaging lens are not captured by the WFS.

One should note, that the light paths coming from the mirror are similar to the light coming from a single point source in the center of the focal plane of an objective. Sources located remote from the center are not replicated, because in an objective the rays would be refracted inwards, meeting at the FP of the objective, while the mirror does reflect all beams parallel and straight downwards.

V:/LennartAfter successful mounting and aligning of WFS and DM in the Fourier planes, the automatic determination of the control parameters of the DM was used to find the feedback loop coefficients. The program cycles through various Zernike patterns and receives the variations in the wavefront from the WFS. By doing so, the DM can calculate the connection between the applied stroke and the effect it has on the wavefront to set values for the control parameter. Leaving the mirror flat, Figure 3.4B and 3.4A was recorded. Then, the feedback loop was turned on. After a few seconds, the mirror pattern stabilized and a nearly flat wavefront was received from the WFS, as shown in Figures 3.4D and 3.4C.
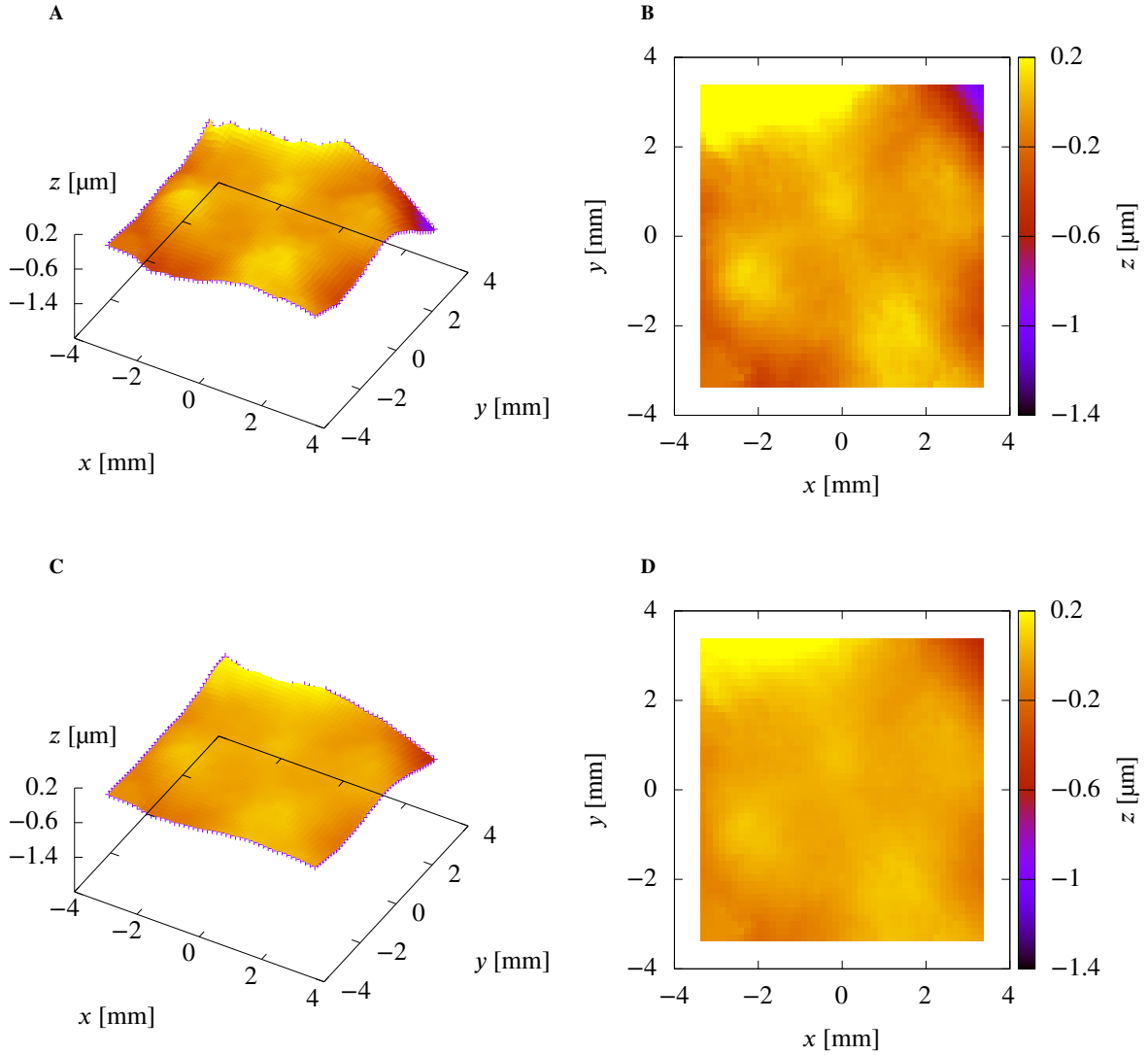
Figure 3.4: The WFS is illuminated directly by the expanded laser, which is reflected from a mirror mounted on the sample stage. **A, B** DM loop turned off, the mirror surface is nearly flat. The wavefront at the sensor is spherical with a quadrupole shape. The rms wavefront error is $r = 0.12\,\mu\text{m}$ **C, D** DM loop turned on, the DM creates primarily an opposing spherical aberration and an astigmatism to correct for the aberrations. The rms wavefront error is decreased to $r = 0.04\,\mu\text{m}$. In both cases, a 488 nm laser at an effective power of 1 mW was used for illumination.

3.2 Building a wavefront corrected widefield illumination setup for *d*STORM

As the correction succeeded using of the simulated fluorescence from the mirror, measurements of fluorescent probes were aimed. The microscope was returned to its original structure by replacing the mirror with an objective lens and changing the collimated illumination back to focus onto the back focal plane of the chosen objective.

3.2.1 Choosing the optimal objective lens and immersion fluid for low spherical aberration

The objective plays a crucial role in the performance of the microscope, as it determines the magnification of the system and the field of view. Especially for *d*STORM , the numerical aperture NA of the objective determines the number of photons which the objective can collect as well as the diameter of the beam at the objectives exit pupil. Two different approaches are possible when choosing the immersion fluid. First, a standard immersion oil enables the use of a 1.49 NA objective, yielding the highest photon count, but the refractive index of the immersion oil $n_{\text{IO}} = 1.518$ differs significantly from the refractive index of biological samples $n_{\text{sample}} \approx n_{\text{water}} = 1.333$. Together with the large photon detection angle it induces strong, mainly spherical aberration. [70] Second, the refractive index of silicone oil $n_{\text{SO}} = 1.35$ matches the index of the aqueous sample, but objectives using silicone oil only reach a NA of 1.35, leading to reduced photon count, which is a crucial factor, determining the number of

localizations for SMLM. The choice was made before assembling the adaptive optics setup, because the difference in the NA does change the size of the beam at the objective exit pupil (see equation 1.24), and therefore changes the beam width in the Fourier planes.

Two different objectives were tested, a 100×1.49 NA APO TIRF oil immersion and a 100×1.33 NA SR HP Plan APO silicone oil objective. As a sample, a $1\,\mu m$ crimson fluorescent bead (CR1) was embedded in low-melt agarose at a depth of about $17\,\mu m$ and illuminated by a $640\,nm$ laser.

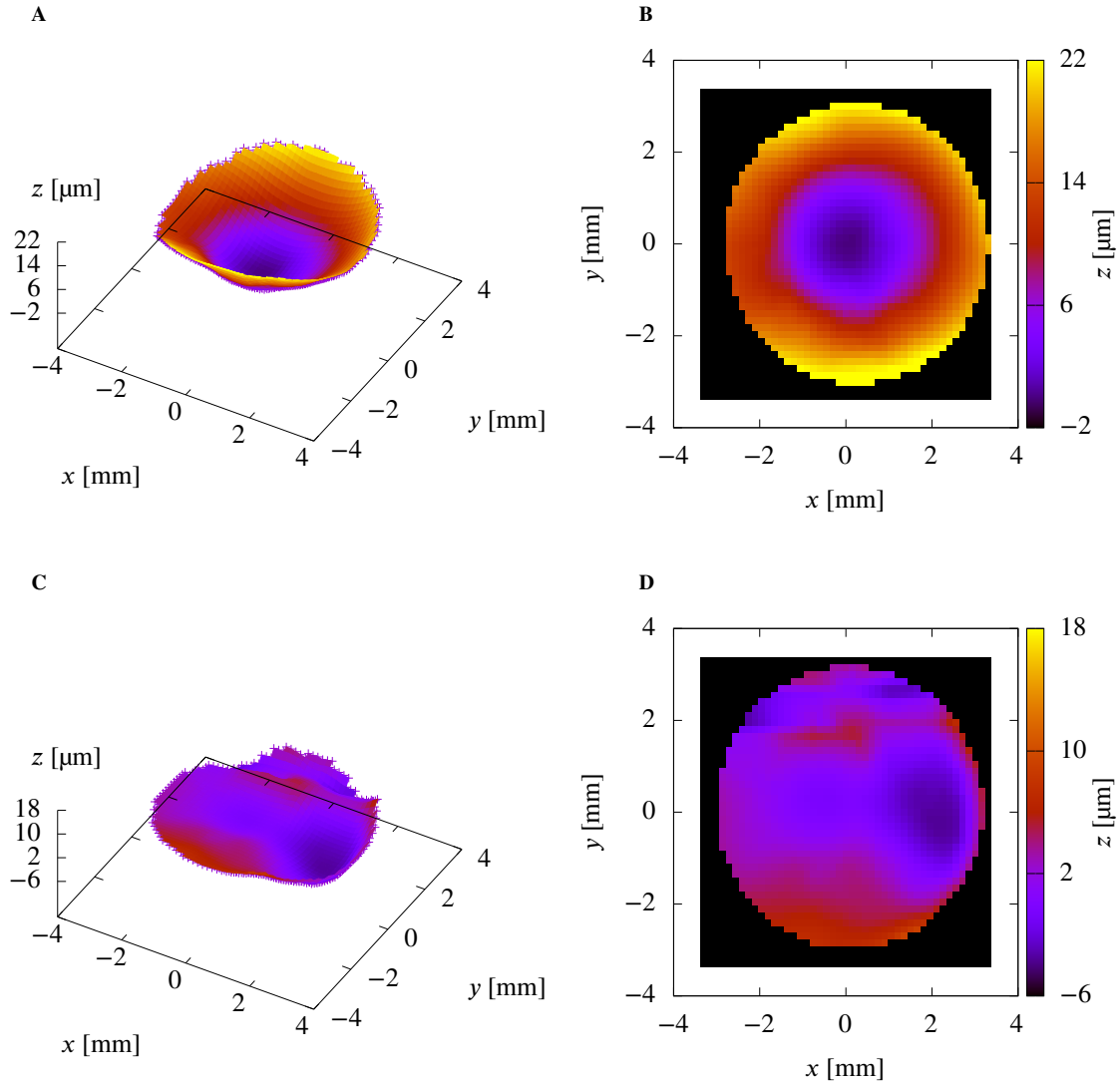**Figure 3.5:** A $1\,\mu m$ crimson fluorescent bead (CR1) was embedded in low-melt agarose at a depth of about $17\,\mu m$ and illuminated by a $640\,nm$ laser. **A, B** 100×1.49 NA APO TIRF oil immersion objective. A strong spherical aberration is present. **C, D** 100×1.33 NA SR HP Plan APO silicone oil objective. Nearly no spherical aberration is present, the wavefront is overall more flat, indicating less optical aberrations.

One can see that the silicon oil objective significantly reduces the spherical aberration induced by the normal oil immersion objective. Therefore, the setup was build around the silicon oil objective.

3.2.2 Restoring image-side telecentricity of the Nikon Ti-E by a $750\,mm$ field lens in the image plane

The field lens was integrated into the system to restore the telecentricity, as discussed in Section 1.6. The effect of the field lens is especially pronounced when looking at the power distribution in the Fourier plane. The WFS therefore acted as a camera with the resolution of the LGA.
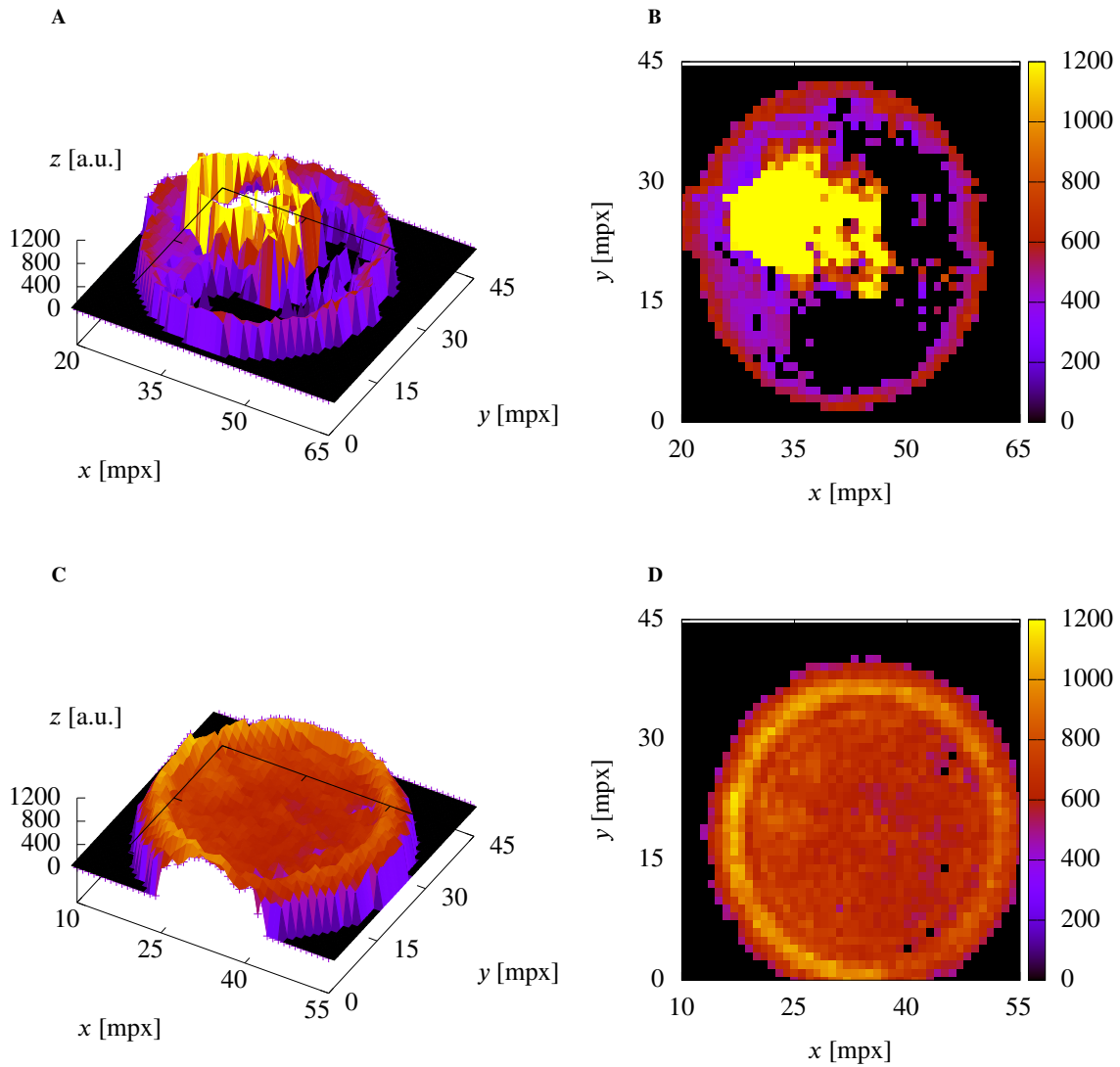
Figure 3.6: Power distribution at the wavefront sensor. *x* and *y* axis show the masterpixel (mpx) of the WFS, which correspond to the lenslets of the LGA. **A** No field lens is used. The beam power reaching the sensor is highly inhomogeneous featuring spots where nearly no light reaches the sensor, and a distinct area of high power-density in the center. **B** By inserting the field lens, the beam spot is now significantly more homogeneous

The power distribution in the Fourier plane was significantly improved by the field lens. Likely contributing to the inhomogeneous distribution is the divergence of the overall beam through the relay systems, enhanced by the fact that the WFS is furthest component measured from the object. [71]

3.2.3   Aperture in image plane in front of the WFS

To verify the considerations made in Section 1.5.3, an adjustable aperture stop was placed in the image plane to block all rays coming from remote image points.
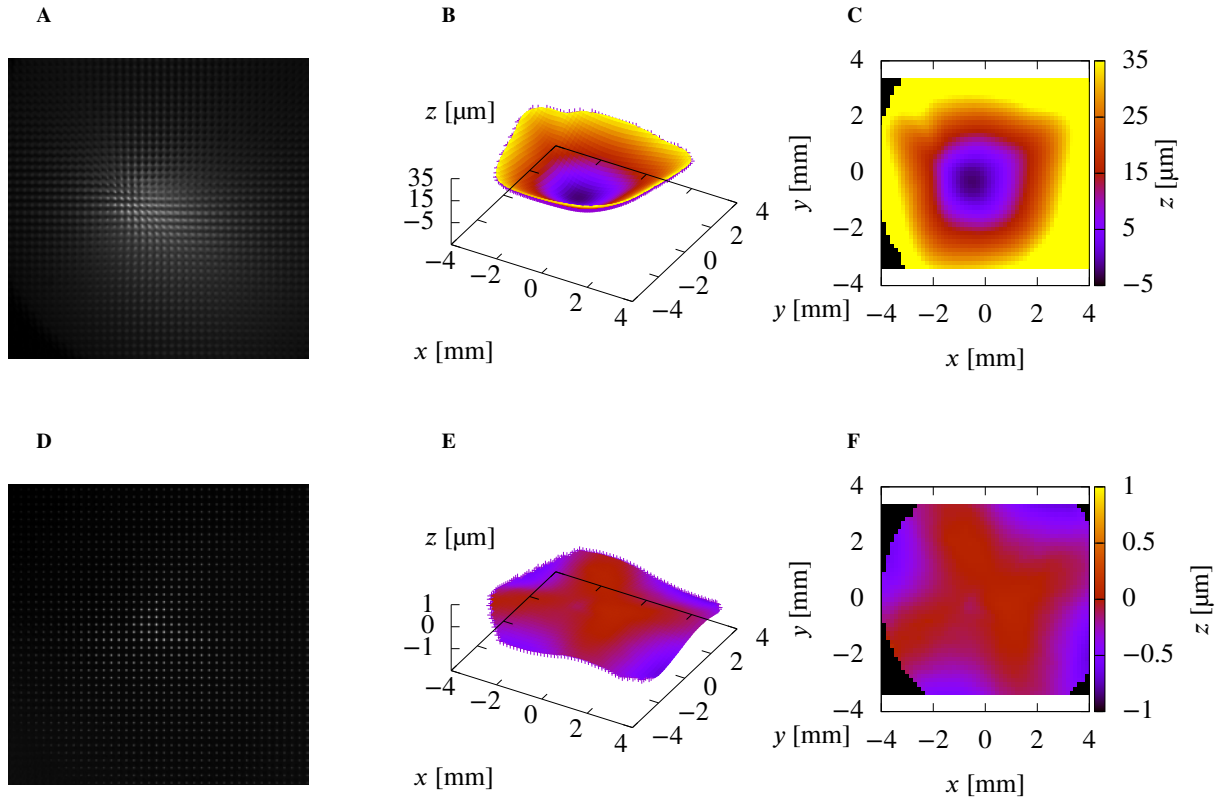
Figure 3.7: A Spotfield image of a green chroma slide, widefield illuminated by a 488 nm laser with clear aperture in the image planes. The slide provides an emissive plane, equivalent to an infinite number of point-like emitters. As a result, the spots on the sensor are washed out and can hardly be distinguished from the neighboring spots. A spot localization is highly inaccurate. **B, C** Accompanying wavefront measurement. Strong spherical aberration can be seen. **D** Spotfield image of the same sample and illumination, but with added aperture in the image plane in front of the WFS. The contrast was increased to enhance the brightness of the spots. The spots are distinct and clearly visible. **C, D** Corresponding wavefront. The spherical aberration is not visible any more. Note the difference in z scale.

Reducing the image plane to a point results in a distinct high-contrast spotfield image, as seen in 3.7. However, considering that most of the beam is blocked by the aperture, the photon count is highly reduced. The aperture was adjusted until the maximum opening was found, that still resulted in distinct spots. The opening was chosen to be around $d_{aperture} = 0.9\,\text{mm}$, which was found sufficient in every measurement conducted. The aperture causes the wavefront to become nearly flat, only showing the same quadrupol pattern as already observed from the test setup using the direct laser illumination. For lower light applications, a larger aperture diameter should be chosen to ensure enough light for the spot detection.

3.2.4 Fluorescent beads as guide stars for a spectral separation of imaging and wavefront control

The light coming from the fluorophores is many orders of magnitude dimmer than the excitation laser, and even when using the full available laser power of 50 mW, which results in fast bleaching, the fluorescence intensity is still not sufficient for the detector of the WFS. Even though a more sensitive camera may be able to capture a sufficient signal, an approach originally coming from astronomy [72, 73] has been used successfully: The use of guide stars. [74, 70, 75, 76] In a standard microscope, the scattered illumination light is measured directly. In contrast, in a fluorescence microscopy setup, emitted light from fluorophores is measured, while the illumination light is used only for excitation and all scattered residue is subsequently filtered out before the camera. Depending on the dye, only small amounts of light are emitted and therefore highly sensitive cameras are needed for detection. Because the WFS does not feature a high-QE sensor [7], the fluorescence light itself was found to be not sufficient for stable wavefront measurements.

A solution to this problem was introduced by [77] for confocal and subsequently [78] for widefield illumination. Both groups injected fluorescent microspheres into the sample, which are densely loaded with a bright fluorescent dye. The microspheres are placed in the area of interest and a dye is chosen which differs in wavelength from the dye which labels the structure of interest. Then, two matching excitation lasers are used to illuminate the microspheres

and the labeled sample. By choosing different emission wavelengths for the dyes, a dichroic filter can be used to direct the light from the microspheres onto the WFS for correction, while the fluorescence from the sample itself passes onto the camera for imaging.
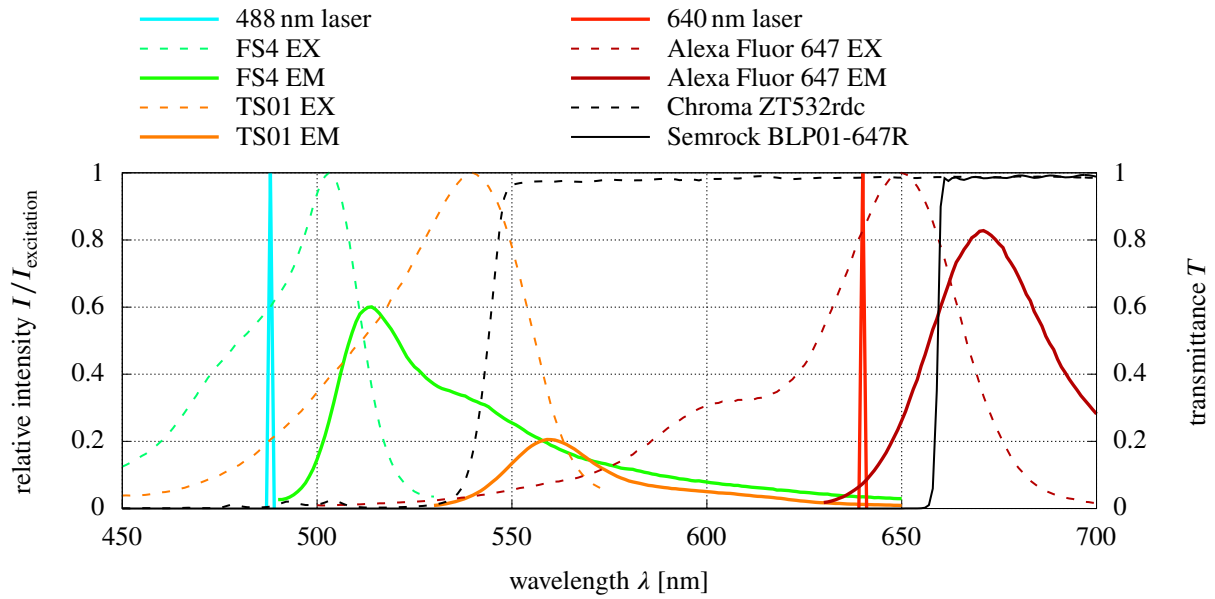

Figure 3.8: Spectra of the beads, the dye and the laser used. For the intensity I, the excitation (EX) maximum of both the Alexa Fluor 647 dye and the microspheres is set to 1, and the emission (EM) is normalized to the respective excitation with the corresponding laser. The crosstalk was considered negligible. The laser intensity maximum is also set to 1. The overlaid transmission curve T of the dichroic filter shows that a the emission spectra of the beads and the dye are clearly separated.
The green spectrum of TS01 was not provided by the manufacturer, only the peak excitation and emission wavelengths are given as shown in table 2.3.
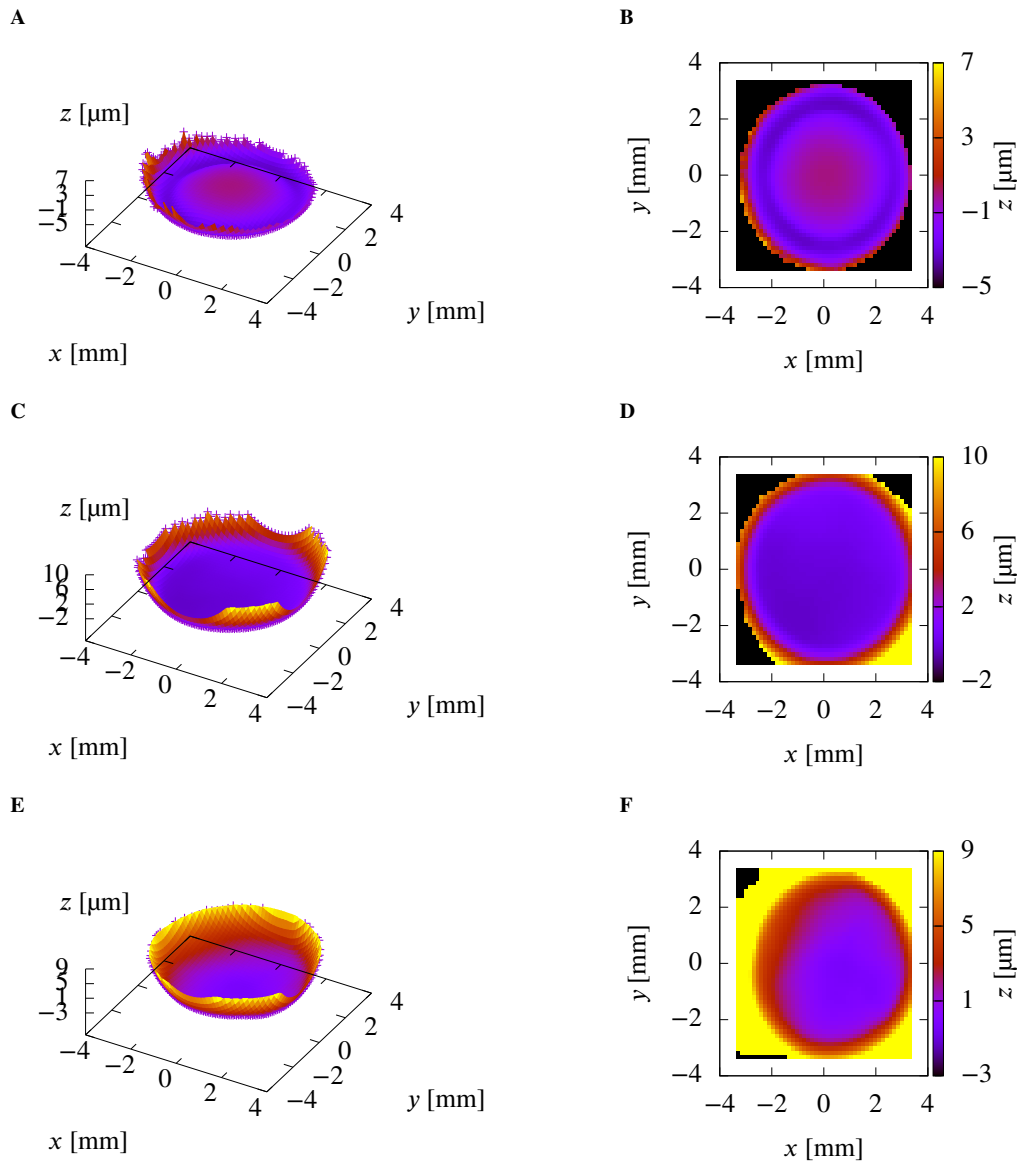Data was taken from [51, 53, 79, 80, 81]

Figure 3.9: Wavefront of 3 different microspheres. **A, B** Wavefront of a 1 μm FC6 bead. **C, D** Wavefront of a 1 μm FS4 bead. For both wavefront, the beads were illuminated by a 488 nm laser. **E, F** Wavefront of a 1 μm CR1 bead. The bead was illuminated by a 640 nm laser. Both lasers were set to 10 mW output power. The size of the wavefront image is approximately the same for all spheres, because it depends on the diameter of the Fourier plane, which is set by the optics and is independent of the size of the object itself. The zero-point of the z axis varies due to automatic scaling of the image in the software. Extended black surfaces were not captured by the sensor. Reasons are either over- or underexposure, or, most likely in this case, too much slope in the wavefront, which causes the spot to leave the masterpixel. Extended yellow surfaces were captured by the sensor, but lie outside the chosen z range. The same range was chosen for all figures to ensure comparability.

To find a suitable guide star for the WFS, several beads in different sizes were tested. In general, larger beads generate brighter, but also more extended spots in the spotfield image. Therefore a compromise is necessary. The 1 μm CR1 as well as the 4 μm FS4 beads were used extensively - however, for the biological samples presented later the higher brightness of the FS4 beads was found superior. Also, the chromatic separation of the CR1 beads from the Alexa Fluor 674 emission was found more difficult, as shown by the high overlap of the respective emission spectra. As later also the PSF of the system was needed for correction, TS01 beads were used. However, these beads are not sufficiently bright to also act as guide stars.

3.2.5 Mechanical adjustment considerations

The following part could have been placed in the Methods section of this work. Nevertheless, during the course of the thesis I found myself faced with several concepts regarding system layout, adjustment and stability, which are presented as a personal result in the following sections.

Modularity   In general, a modular approach to alignment was followed as suggested by [69, 68, 82]. Therefore, modules were either 1) taken as manufacturer-assembled components, e.g. the body of the Nikon Ti-E microscope with its fixed tube lens, prism and objective placement, or 2) components were pre-aligned outside of the system and then integrated as a whole, e.g. in form of cage rod pre-assemblies.

Mirror alignment   In general, two mirrors are needed to align a laser beam. The first determines the position at which the laser is reflected from the second mirror, thereby determining the laser source point. The second mirror then changes the angle at which the laser is reflected. When changing these two parameters, the source point and the angle, the laser beam can be moved in all possible degrees of freedom. When all mirrors are aligned and the laser beam follows the desired path, the lenses and cameras can be aligned.

Lens and camera alignment   One can devide between three alignment steps: Lateral, axial and rotational alignment. For lateral alignment, a small laser beam is used, and components are moved until the laser hits the component exacly centrally. For this purpose, alignment plates where used, which feature a crosshair printed on the front and a small bore in the center. With the plate attached to the component, the laser can only pass if the component is laterally aligned.
Axial alignment depends on the purpose of the lens being used. In this setup, all lenses were mounted such that they are distanced by the sum of their focal length to maintain a 4f-configuration. By using Cage systems where possible, the lenses could be moved axially without significantly changing the lateral position.
Last, to ensure the lens surface is placed exactly perpendicular to the beam, the back reflection was tracked as described in [69].

3.2.6   Adjustment of the excitation path

The excitation light in general has the purpose of illuminating the samples fluorophores to induce their emission. For a widefield configuration, a even illumination of the whole sample plane is considered optimal. To achieve this, the laser must be focused onto the back focal plane of the objective. The objective then collimates that light and forms a parallel beam, which ideally fills the whole front lens aperture of the objective. Due to the collimated beam having a gaussian intensity profile, a slight overfill is desirable to flatten the gaussian curve and providing a wider area of even illumination. However, overfilling the front lens aperture and thereby cutting of parts of the beam results in a loss of intensity. Alternatively, a top-hat beam shaper could be implemented to archive a flat intensity profile and homogeneous illumination. [29]

Modules   The first fixed units are the laser blocks, which are mounted on the laser table. A mirrors and a longpass filter for each laser are used to align all lasers and direct them to the second unit, the TIRF rail. Here, all lenses are mounted to focus the light onto the back focal plane of the objective. Two different systems are used, which focus the light at different angles, to change the size of the illuminated field of view at the sample plane. The rail is mounted in a way such that the whole rail can be moved along the optical axis and perpendicular to the microscope back port, to move the laser beam to the side of the objectives back pupil and thereby changing from epi-illumination to the HILO and TIRF modes. Last, two additional mirrors are used to reflect the laser from the TIRF rail down and into the third module, the back port of the Nikon Ti-E microscope body.

Alignment process   First, the mirror and corresponding longpass filter on the laser table are used to center the ray on two fixed targets on both ends of the TIRF rail. A lens tube is threaded into an empty thread of the nose piece, which features a phosphorescent target with cross hair. Then, the mirrors between the TIRF rail and the microscope body are changed until the beam hits the crosshair centrally. Then, the lenses with longer focal lengths (above 100 mm) are inserted at their approximate positions. Due to their low focusing power, they do not alter the spot size considerably and therefore can be aligned individually until the laser is central on the crosshair again. Then, the the lenses with the smaller focal lengths are inserted at their approximate position. All lenses are folded away apart from a corresponding pair. As the corresponding pairs are designed to focus onto the back focal plane, the spot on the crosshair at that position is again clearly visible. The smaller lens is then adjusted until the spot is central again. This was repeated for all lens pairs. At this point, all lenses are central on the TIRF rail.
Next, the mirrors between the TIRF rail and the microscope body are adjusted. Even though the beam has been aligned to the phosphorescent crosshair already, the angle at which it hits the crosshair is still arbitrary. To align the laser to the optical axis of the objectives, all lenses are folded away, and a long lens tube is mounted in an empty thread of the microscopes nose piece. The lens tube featured two alignment targets: A frosted glass with a 1 mm central bore on the bottom, approximately at the height of the back focal plane of the objective, and a phosphorescent screen with crosshair at the top. The mirrors are adjusted until the laser passes through the hole in the frosted plate and hits the crosshair centrally.
For the final adjustment, a corresponding lens pair on the TIRF rail is folded in place and the objective is used.

The smaller lens is moved until the light is collimated by the objective. This is checked by the spot size on a paper tissue directly above the objective and on the ceiling, which should be of the same size for a collimated beam. To fine-adjust the position of the smaller lens, a fluorescent slide is mounted in the sample plane and a Bertrand lens is inserted into the eye piece. The Bertrand lens enables direct observation of the back focal plane of the objective. (FIgure 3.11A) In the back focal plane, the limiting aperture is placed, which can be seen as a bright circular edge. Then, the smaller lens is moved until the spot at the back focal plane is minimal.

During the adjustment, the FoV above the objective was not always fully illuminated. This can be changed by changing the angle at which the excitation light is focused onto the back focal plane of the objective. A larger angle will produce a larger beam diameter above the objective. To increase the angle, the last lens on the TIRF rail must be moved closer to the microscopes back port. However, between the Lens and the back port, two 2 inch right-angle mirrors are needed, as the beam diameter is more than the standard 25 mm diameter for optical components. This led to many iterations of the design of the TIRF rail, which each increased the FoV at the camera. The iterations are shown in Figure 3.10. The iterations should not be solely interpreted as stepwise improvements, but rather show that different FOV and subsequently different power densities in the FOV are achievable.
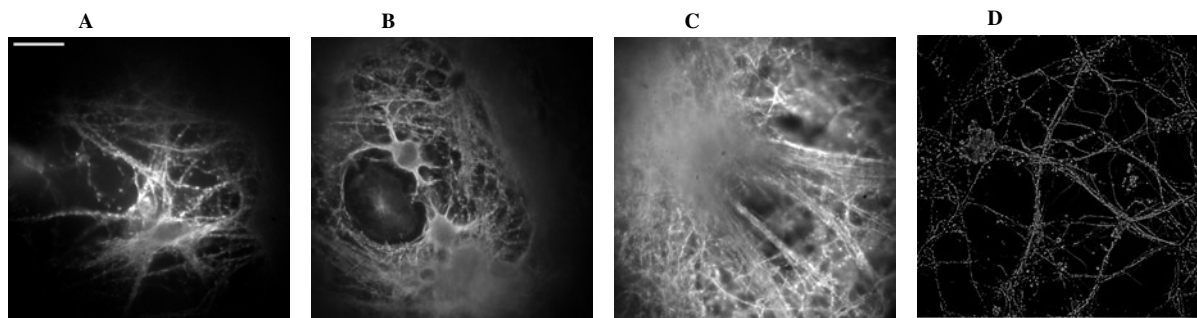

Figure 3.10: Iterations in the illumination path: Hippocampal neurons in cell culture, stained with α-Tubulin. Scale bar for all images is 20 µm **A** Initial illumination condition. **B** Preliminary condition. **C** Final condition. **D** Reconstructed dSTORM image under final illumination conditions.

3.2.7 Adjustment of the emission path

The emission path serves the purpose to relay the image to an additional image plane to create an accessible Fourier plane for the DM. Further, an additional Fourier plane needs to be created for the WFS, and the path must be coupled into the detection light path.

Modules   In the emission path, the camera and imaging lens L_1 were pre-assembled, as well as the relay system for the WFS, including the WFS itself.

Alignment process   First, all components were placed at the approximate distances taken from the setup modeled in Zemax Optic Studio. The objective was removed and a mirror was placed above the nose piece. The filter cube was removed, and all lenses were removed from the excitation path. The mirror was then aligned until the ray was reflected back into the laser. To avoid damage, the beam power was reduced. Next, a beam expander was installed in the excitation path, using a 25 mm and a 200 mm lens, to create a collimated beam with a diameter of approximately 10 mm. This is beneficial, because collimation can be checked easily with a shearing plate interferometer, or using the WFS. This beam is focused by the tube lens into the first image plane, where L_F is placed, by looking for the smallest focus point reflected from the lens body. L_1 is then moved, until again a collimated beam is formed. Then, a periscope is build to circumvent the tube lens in the microscope body. The beam is reflected out of the excitation path behind the beam expander, and reflected back into the emission path behind L_F. This way, L_1 directly receives the collimated beam and focuses it into the Fourier plane, where the DM is placed. The DM is moved until the smallest focus point is visible on the mirror surface. Then, L_i is moved until again a collimated beam is created. Next, the objective was put back into the nose piece, and a line grating was placed onto the objective. Using the eye piece and the microscope's build in halogen lamp, the stage with the grating was moved into focus. Then, the excitation was switched to the side port to relay the image to the camera. The camera was then moved until the grating was in focus as well, assuring seamless transition between the eye piece and the camera later. (Figure 3.11B)

At this point, the camera and the objective are aligned to each other, and traditional, non-adaptive optics (AO) imaging would be possible. Next, the DM needs to be further aligned. Because the 300 mm focal length of L_1 gives a stretched focus point, the focus point on the DM does not provide a precise measure for placement. To readjust the placement, a Bertrand lens was inserted in front of the camera. A 400 mm lens was used. The lens was moved until

the Fourier transform of the line grating was sharply visible on the camera. (Figure 3.11C) The Bertrand lens then relays the Fourier planes onto the camera. The placement of the Bertrand lens was further improved by using the halogen lamp and a frosted plate on the stage to see the back focal plane of the objective on the camera. (Figure 3.11D)

Now, objective, camera and Bertrand lens are aligned to each other, but still not the DM.

Then, the line grating was removed and a fluorescent slide was placed on the objective to create a light source. A hair was fixed to the surface of the DM. (Figure 3.11E) The DM was then moved and found focused when hair and the reflection of the hair were equally well focused on the camera, telling that the optimal focus lies between both, where the mirror surface should be. (Figures 3.11F, 3.11G) Importantly, due to the movement of the DM, the beam path between L_1 and the DM has now changed, disturbing the relay to the objectives back focal plane. The Back focal plane is not visible on the camera any more. Consequentially, the Bertrand lens is moved. However, it is not possible to focus both, DM and back focal plane, at the same time, so a focal point in between both was used. Then, the DM is moved again until the hair is focused in the eye-piece. (Figure 3.11H) This iterative process of moving the DM and the BL was repeated around ten times, until re-positioning of the BL showed both DM and objectives back focal plane sharply visible on the camera.
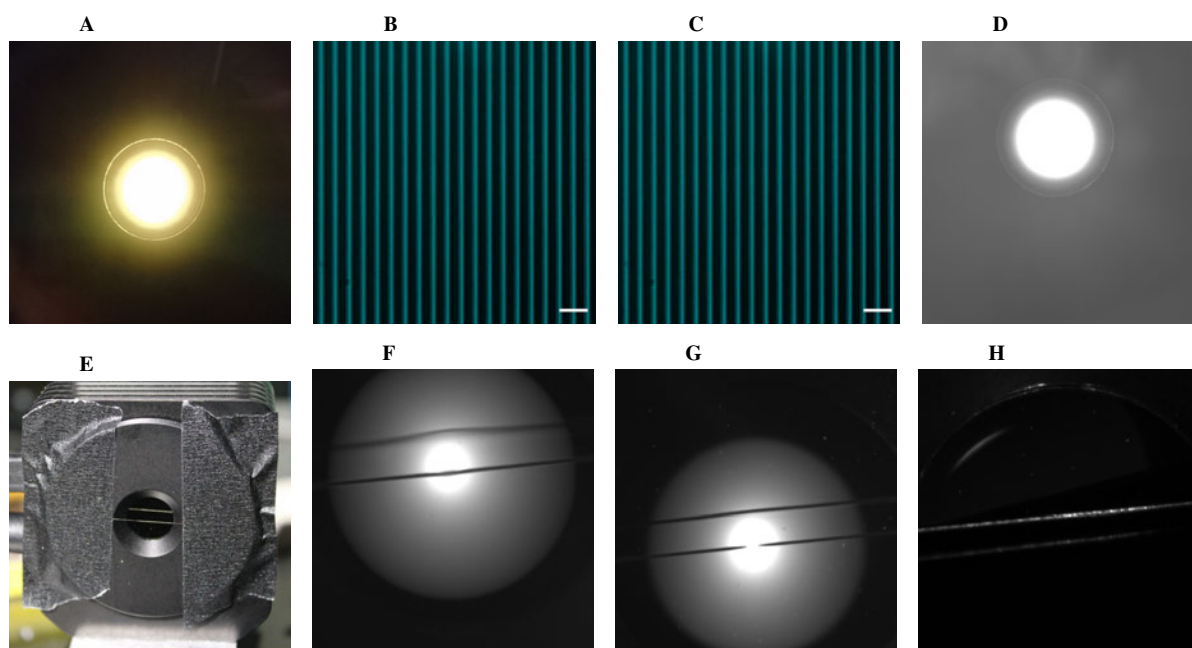

Figure 3.11: Images taken during different stages of the alignment process.

3.3 Imaging

In this section, two samples will be imaged to frame the microscopes ability to correct for specimen-induced aberrations. The setup used for imaging is shown in its final form in Figure 3.12.
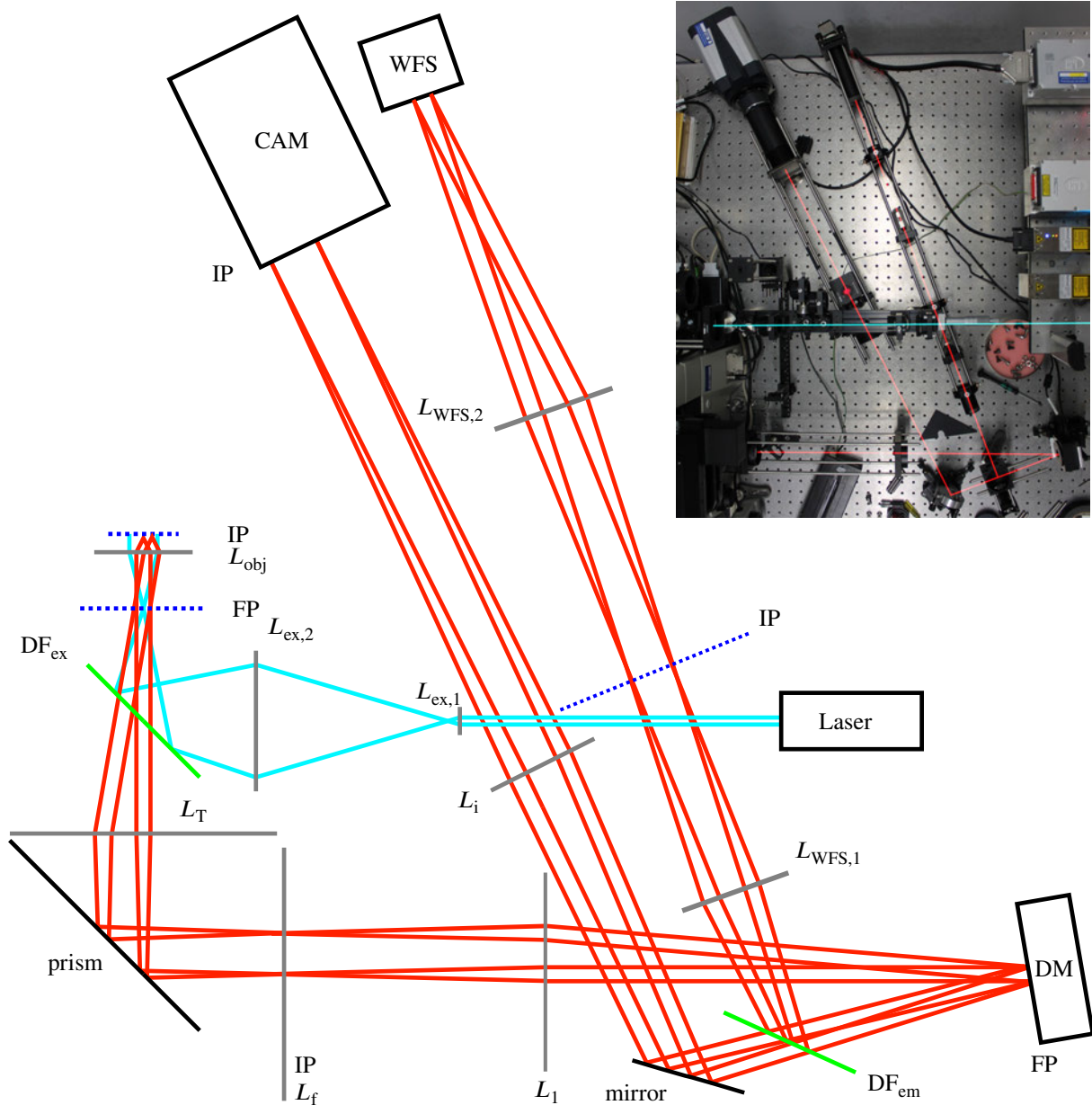
Figure 3.12: Schematic of the light paths of the adaptive optics microscope setup with DM and WFS in its final form. The excitation path from the laser to the specimen is shown in light blue. The emission path from the specimen to the camera (CAM) and to the WFS is shown in red. Fourier planes (FP) and image planes (IP) are marked with dotted dark blue lines if they do not coincide with a component. Lenses are marked in gray, mirrors and reflective prisms are shown in black. Dichroic filters (DF) are marked in green. The objective and the magnification of the lenses is not to scale.

Lenses $L_{ex,1}$ and $L_{ex,2}$ focus the excitation onto the back focal plane of the objective. The objective lens collimates the light and provides a widefield illumination of the sample.

Only two excitation beam paths coming from a centered point source and one off-centered point source are shown. The diverging collimated beams coming from the objective lens L_{obj} pass the infinity space in the microscope body, get focused by the tube lens L_T and reflected out of the housing of the Nikon Ti-E by the internal prism. At the first image plane, a field lens L_f is placed to correct for the non-telecentric placement of the tube lens and to provide a defined Fourier plane for the DM. The light from the DM is split by the dichroic filter at 640 nm. The red side of the spectrum is focused onto the camera, while the blue part is focused and collimated again by the lenses $L_{WFS,1}$ and $L_{WFS,2}$ to create another Fourier plane for the WFS.

Insert: Photograph of the setup based on a Nikon Ti-E inverted microscope and Thorlabs DM and WFS. The excitation light path (light blue) and emission light path (red) are drawn. Later, the system was fully covered in black foam board to block stray light.

3.3.1 Hippocampal Neurons

An artificial sample was created by placing a hippocampal neuron cell culture on top of an unstained 100 μm murine brain slice. The brain slice acts as a diffusion layer, inducing aberrations, to challenge the correction mechanism. The correction procedure described in Section 2.2.4 was followed to obtain the images shown. First, the uncorrected

image is presented, followed by the images obtained during the two correction steps.
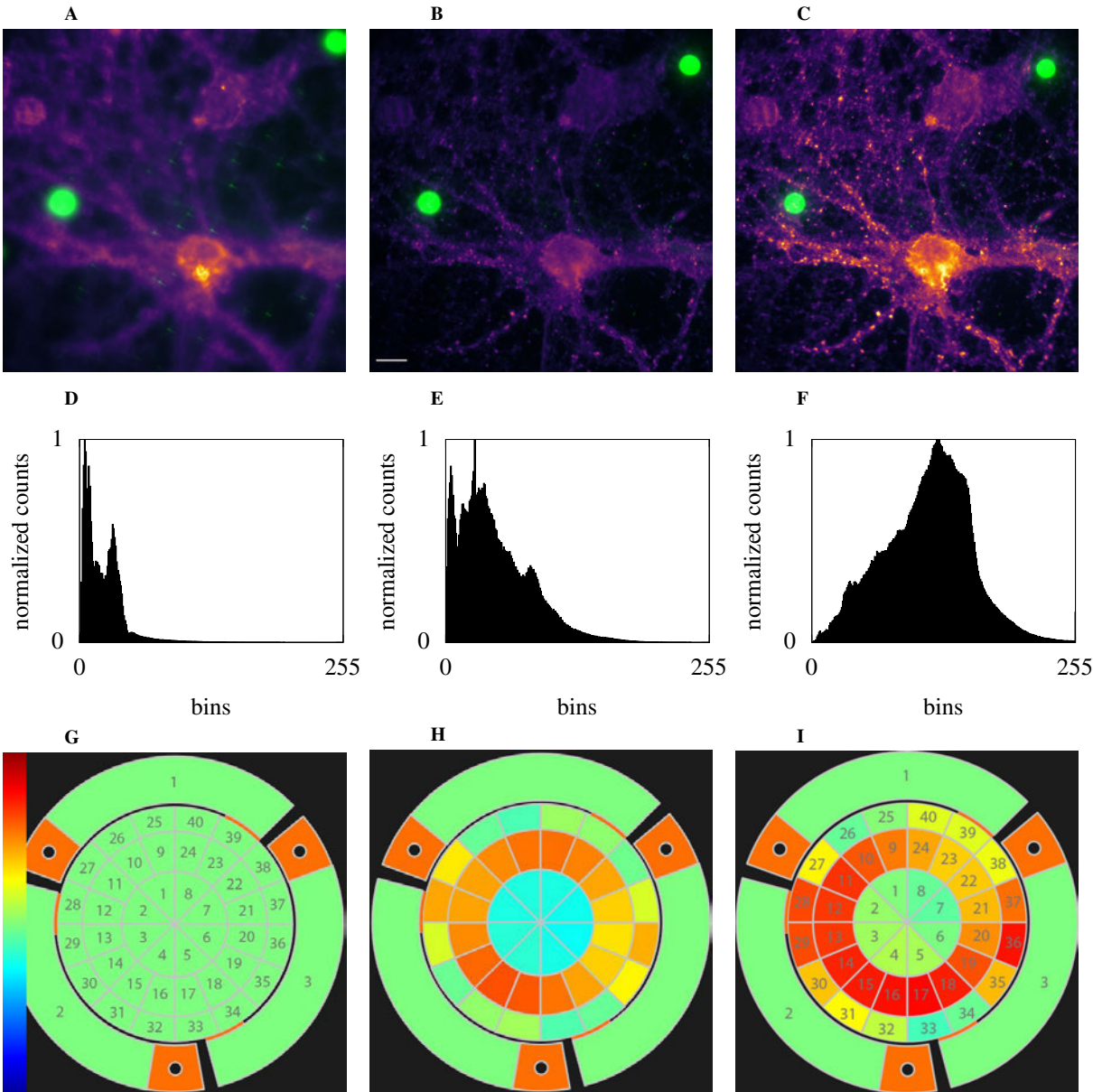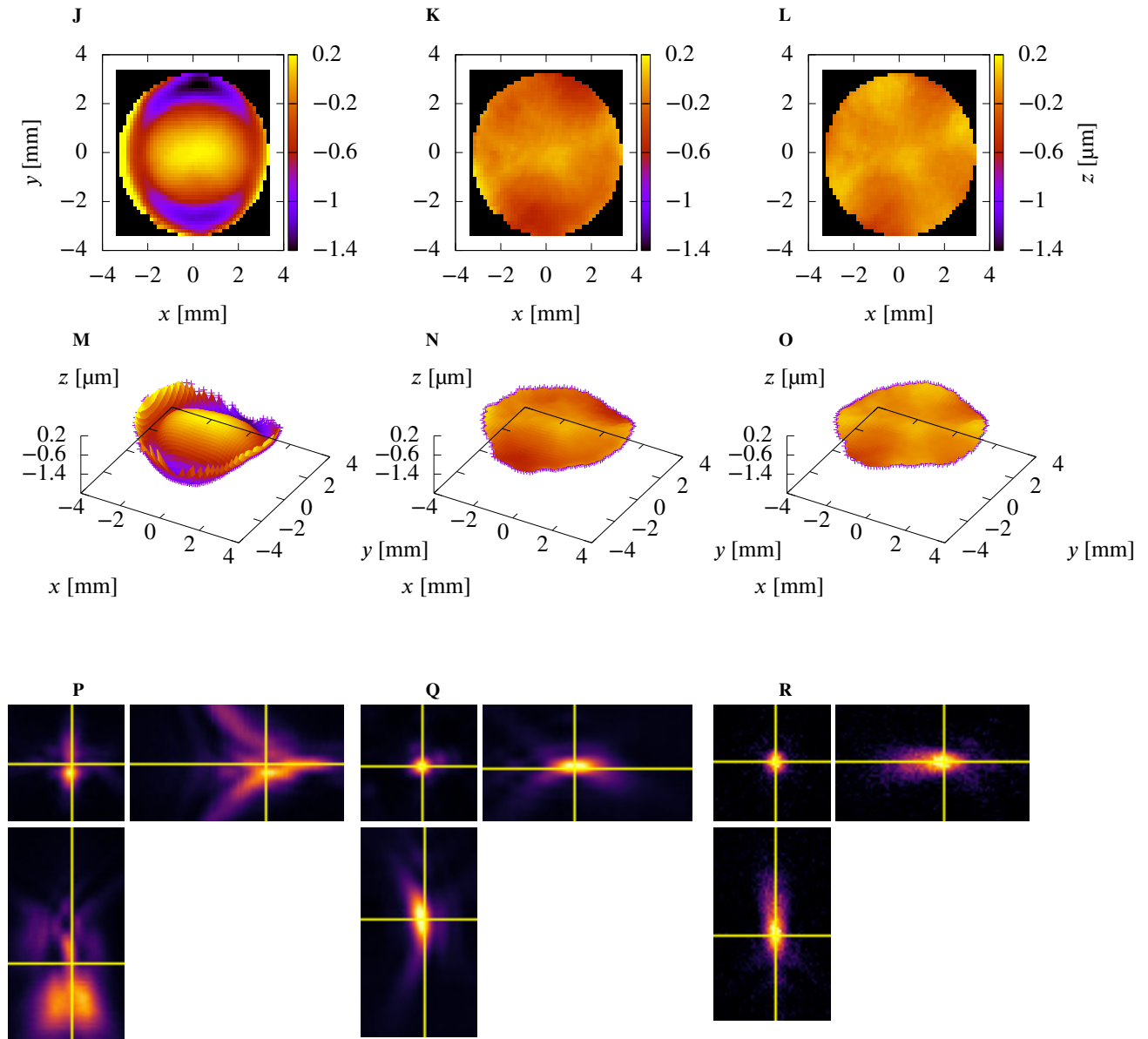
Figure 3.13: Widefield image of a murine hippocampal neuron cell culture. α-Tubulin was immuno-stained with Alexa Fluor 647. The cell is imaged through a sagittal 100 μm thick unstained murine brain slice, using a 100× silicone oil objective with additional 2× magnification from the image relay. Between the cell and the slice, 100 nm TS01 beads and 4 μm FS4 beads were placed and are shown in green. The cell was illuminated by a 640 nm laser, the beads were illuminated by 488 nm. The two colors were imaged sequentially, first in red, and overlaid in post. The Figures 3.13A, D, G, J, M, P show the uncorrected version of the image, in Figure 3.13B, E, H, K, N, Q, the wavefront was corrected solely by the values derived from the wavefront measurement, whereas Figures 3.13C, F, I, L, O, R, were corrected by optimizing the PSF of the TS01 beads manually. To make all pictures visible, brightness was adjusted for 3.13A, but kept the same for 3.13B and 3.13C. Scale bar given in 3.13B counts for all three images and is 10 μm. Histograms are given for comparability, which are normalized to their individual maximum. The voltage pattern from the DM is presented in Figures 3.13G - 3.13I. The scale is given as an inlay in Figure 3.13G, ranging from 0 V (blue) to 200 V (red). In the resting position in Figure 3.13G, 100 V is applied to each segment to give a flat surface. In Figures 3.13J - 3.13O, the wavefront captured from a single FS4 bead is plotted for each correction step in 2D and 3D. The scale bar shown in the 2D graphs also applies to the 3D graphs. Figure 3.13P - 3.13R show the PSF of a single TS01 bead for each correction step, which was captured as a stack of 91 planes. Scale bar in Figure 3.13Q is 2 μm and counts for all images. The square image represents the XY-plane, whereas the rectangular images show the projection to the XZ and the YZ plane, respectively. The planes are marked by yellow lines in each image. Brightness was adjusted for each correction step to show the features of the PSFs.

In Figure 3.13A, the optimal focus point was found by minimizing defocus on the WFS. To ensure that the correction of the adaptive optics system is not due to a correction of the focal plane, the perfect focus system was used to keep the objective steady, and the defocus was checked on the WFS throughout the experiment. It was found to not contribute in any meaningful way, as it never exceeded 10 % of the leading aberrations.

In 3.13A - 3.13C, the hippocampal neuron cell culture and the beads are shown, as captured by the camera. For the

cells, a multi-color LUT was chosen to enhance detail. The increase in sharpness and brightness from the correction process on the cell culture is clearly noticeable, revealing more detail and more clear edges in the wavefront derived and the manual corrected versions. Note, that in Figure 3.13A the brightness was increased in post compared to 3.13B and 3.13C, because it would not be visible otherwise.

Directly below, the corresponding histograms are plotted to show the brightness increase. One can see, that the correction solely derived from the WFS does not increase the brightness as well as the manual correction. Instead, mostly the image sharpness and contrast is increased.

Figures 3.13G - 3.13I are screenshots from the mirror pattern applied in the two correction steps. One can see a spherical aberration as well as some astigmatism, both of which are the leading aberrations in deep tissue imaging [74, 70, 75, 83]. Manually correcting the PSF of the TS01 bead (3.13I) mostly just increased the stroke in every segment, and did not introduce a new pattern. This means, that the correction derived only from the wavefront measurement does extract the right aberration distribution, but the translation to the stroke of the segments of the DM, which were determined as the γ_i in Section 2.2.3 is off for certain factors. Especially spherical aberration found to be residual in the solely wavefront corrected image. As these factors were determined by hand, the shortfall of the solely wavefront derived correction can most probably be improved by automating the communication between the WFS and the DM.

In Figures 3.13J - 3.13O, the wavefronts captured by the WFS from a single FS4 bead are plotted in a two-dimensional projection and for better visualization as a 3D-plot. The pattern mostly resembles the mentioned aberrations. Spherical aberration causes the curved center and the raised edges. The second most pronounced aberration is astigmatism, encoded in the lowered upper and lower part and the raised right and left of the wavefront. Interestingly, the pattern looks very similar to a pattern simulated by Siemons et al [83] for a HiLyte Fluor 647 tubulin sample at a depth of 17 μm, also showing the combination of spherical aberration and astigmatism in about the same relative magnitude of 2 λ. The observed pattern can be translated to the DM pattern easily, showing the simple connection between the wavefront slope and the stroke of the individual DM segments.

Figures 3.13P - 3.13R show the orthogonal projections of the PSF of the TS01 bead used for the manual correction. In the uncorrected PSF in Figure 3.13P, the astigmatism is clearly visible, as both the XZ and the YZ projection show a broadening on the other side of the PSF, respectively. [76] The strong tails in the XZ-projection (horizontal format) are mainly caused by the spherical aberration.

Interestingly, in Figure 3.13Q, the PSF still shows some asymmetry, and the spherical aberration correction seem to have overshot an optimal correction. However, the intensity is much more centralized and and the astigmatism is nearly not visible any more.

Because the PSF in Figure 3.13R was manually corrected, nearly no residual aberration can be derived by eye. As discussed in Section 2.2.3, the Zernike coefficients can only be altered individually and therefore enable full reduction of the sample induced aberrations, if the system is correctly aligned. Here, one can assume that some misalignment is still present in the optical paths of the microscope, as the wavefront derived correction failed to reliably remove spherical aberration and a small residual spherical aberration is still present and can be seen as the two tails diverging from the optical axis. The residual spherical aberration in Figure 3.13R was approximated to around 215 nm rms wavefront error.

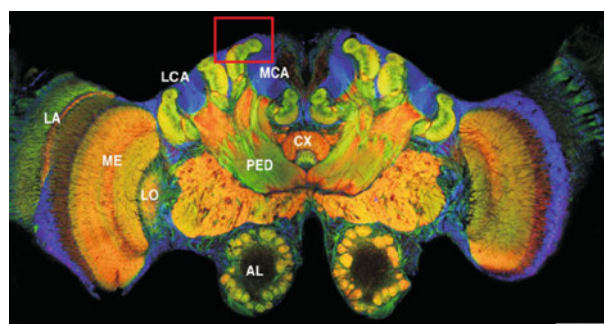### 3.3.2 Honeybee brain slice

Figure 3.14: An overview is given of the honeybee brain, taken from [84]. The slice is labeled in red against synapsin, in green against f-actin-phalloidin in blue against Hoechst, which is not of further interest. To show possible locations of the FOV in Figure 3.15, the area is marked as a red box. Inside the box, the mushroom body calyx is labelled green.
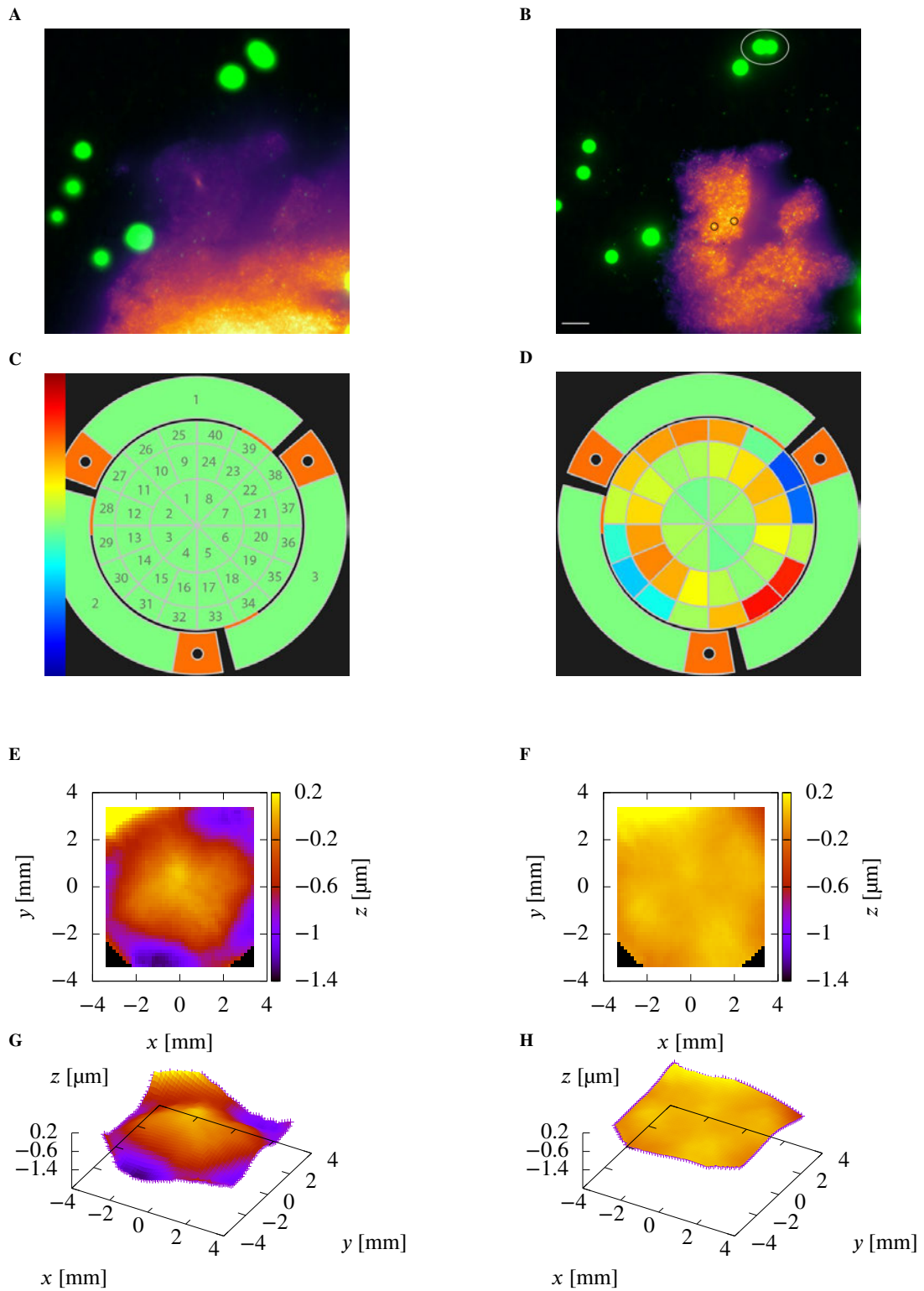
Figure 3.15: Ventral edge of one of the central calyces of the mushroom body from a 80 μm thick honeybee brain slice. Brp was stained with Alexa Fluor 647. The Image was taken at a depth of 80 μm, at the surface opposite to the cover glass. The scale bar is 10 μm. For the Figures Figure 3.15A, C, E, G, no correction was applied, while for Figure 3.15B, D, F, H, the correction was derived from the WFS measurement. The tissue was first illuminated by 640 nm laser and a multi-color LUT was used to enhance details. The large green beads are 4 μm Fluopshere beads, the smaller beads are 0.1 μm TS01 beads, both are illuminated after the tissue was captured at the same position by a 488 nm laser and overplayed in post. The DM pattern is shown below in Figures 3.15C (containing the scale bar) and 3.15D. The scale ranges from 0 V (blue) to 200 V (red). Figures 3.15E - 3.15H show the uncorrected and the corrected wavefronts from a single FS4 bead presented as 2D and 3D projections, each.

Figure 3.15 shows images from the Brp-stained honey bee brain slice at a depth of 80 μm. In contrast to Figure 3.13, no manual correction of the PSF is shown, as it was not possible to improve the point spread function manually by evaluating it by eye. Compared to 3.13, the PSF was more faint and an algorithm would be needed to converge on an improved PSF. In Figure 3.15A, the brightness is strongly increased in post compared to Figure 3.15B to make the image visible. In Figure 3.15A, a Reflex is visible in the center of the image. The reflex is assumed to to be caused by the optical system and could not be removed. It is only visible in Figure 3.15A due to the lower brightness depth of the image. The correction in Figure 3.15B reveals a more detailed view of the edge of the sample and totally shifts the brightness distribution away from the lower border to a more homogeneously illuminated FOV. Also, bead position shifts significantly (example marked in white), especially pronounced at the borders of the image, implicating the importance of a flat wavefront for structural examinations. In contrast to the uncorrected image, bright spots are visible in the tissue sample. Figures 3.15C - 3.15D show screenshots of the DM pattern, which together with the wavefront images from a single Fluopsphere bead reveal the main two aberrations in the image: Spherical aberration is observed by the dome-shaped center and the raised edges in Figure 3.15E, especially pronounced at $x, y = -4, 4$. The astigmatism is not pronounced in the wavefront, but it is visible on the pattern of the DM in Figure 3.15D. Overall, the wavefront is well corrected, only the corner at $x, y = -4, 4$ remains raised, as it probably exceeds the maximum stroke applied on the DM.

In Figure 3.15B, the slice has an irregular edge, probably resulting from damage that occurred by transferring the slice to the microscope slide. Accumulation of Brp is assumed to indicate localization of AZ In the tissue, small spots are visible, where the Brp is accumulated. As an example, two spots are marked with black circles. As lined out in Section 1.8, Brp is selectively part of the AZ, suggesting that accumulations of these spots resemble AZ localizations. The abundance of AZ in the mushroom body calyx is also reported by Ehmann et al. [45]. If the resolution would have been further increased, one could investigate the clustering of the Brp. Ehmann et al. [45] reported a clustering of 26 %. For comparison, Ehmann et al. [45] performed *d*STORM on Brp-labelled neuro-muscular junctions in *Drosophila* to resolve the ultrasturcure of AZs. The group also reports that approximately 26 % of the detected Brp was not grouped into clusters. Gehring et al [46] also showed a high abundance of Brp in the calyx.

A   **B**

Figure 3.16: Gaussian fits over 20 line profiles were performed, taken from the same FOV at imaging depths of 0 μm, 20 μm, 50 μm and 80 μm. The image at 80 μm in its uncorrected and corrected version is shown in Figure 3.15. The fitting routine is discussed in the text (see Equation 3.8). Data is presented as mean ± standard deviation (SD). **A** FWHM of the fitted Gaussian functions. The width increases with increasing depth, smearing out structures. **B** Intensity I of the measured structures, taken from the maximum height of the Gaussian fits.

Fits were performed using `Gnuplot` for the Gaussian function

$$f(x) = \frac{c}{\sigma\sqrt{2\pi}} \exp\left(\frac{-(x-\mu)^2}{2\sigma^2}\right) + b \, , \tag{3.8}$$

having σ, μ, b and c as free variables. Starting values for the fits were set manually for each individual fit and all fits were checked by eye to ensure proper conversion of the fitting routine. The FWHM was then calculated from σ using:

$$\text{FWHM} = 2\sqrt{2\ln 2}\,\sigma \, . \tag{3.9}$$

The maximum intensity I was calculated by:

$$I = \frac{c}{\sigma\sqrt{2\pi}} \, . \tag{3.10}$$

Figure 3.16 shows how the FWHM increases proportional with imaging depth, up to a factor of around 3.5 × at 80 μm. Also, the brightness decreases drastically, leaving nearly no signal at 80 μm depth. At this depth the fitting algorithm was checked carefully and the starting parameters were set as precisely as possible to gather a converging fit. Even though the derived FWHM appears to follow the trend, the values should be taken with caution. As a main result of this thesis, the adaptive optics system established in this work is able to nearly fully restore the parameters, as the intensity reached over 80 % of the intensity observed at the surface of the slice, while the FWHM increase at 80 μm could be reduced from 3.5 × to around 1.2 ×.

Other groups have shown wavefront correction in deep tissue. A good indicator for the strength of the aberration before and after the correction is the rms wavefront error, as described in Section 1.2.2. Azucena et al. [74, 70] imaged fluorescent beads 20 μm deep in drosophila embryos and used active wavefront sensing. However, drosophila

embryos are transparent and induce significantly less aberration. The average rms wavefront error was reported to be 104 nm, compared to 521 nm in Figure 3.13 and 587 nm in Figure 3.15. Also, the group used red fluorescent beads (peak emission at 647 µm), which undergo less aberration as discussed in Section 1.7. The leading aberrations were reported as spherical aberration, coma and astigmatism. Tao et al. [77] were able to correct an rms wavefront error of 151 nm, also in drosophila larvae, using active wavefront sensing of red fluorescent beads. The same group also showed that autofluorescence in the drosophila yolk can be used as a guide star for the WFS, where they reported correction of 387 nm rms wavefront error. [85] Bourgenot et al [22] used backscattered laser light as an alternative guide star to circumvent the need to inject beads. They archieved rms wavefront improvements from 190 µm down to 10 µm. Mlodzianoski et al [76] imaged amyloid plaques in mouse frontal cortex up to a depth of 170 µm using sensorless AO. Unfortunately, no wavefront error is reported. As the tissue sample is comparable in optical properties, a high wavefront error could be possible. Zheng et al. [86] corrected a rms wavefront error of 52 nm at a depth of 100 µm for Rhodamine–phalloidin-stained actin filaments in primary mouse endothelial cells using active sensing of fluorescent beads. In general, one can see that our rms wavefront error in the uncorrected image is large compared to the values reported in literature, indicating that the murine brain slice induces high magnitude optical aberrations. The residual rms wavefront error was found to be still higher than most values reported in literature, especially compared to sensorless approaches. However, authors using sensorless AO consistently used less aberrating samples and showed less rms wavefront error reduction compared to their rms wavefront error starting value. Nevertheless, reducing the high residual wavefront error should be aim of the following work as discussed in the Conclusion.

Ehmann et al. performed *d*STORM imaging on Brp in *Drosophila* neuromuscular junctions and showed an average size of AZ to be around 100 nm, when imaged *en face*. [45] This is in broad accordance to the size of (0.32 ± 0.05) µm and (0.44 ± 0.03) µm determined here for the depth of 0 µm and corrected 80 µm, respectively, accounting for the proximity to the diffraction limit at 243 nm.

Chapter 4

Conclusion and Outlook

The development of the adaptive optics microscope described in the former sections was able to successfully correct specimen induced aberrations in an artificial sample at a depth of 100 μm and in a stained honeybee brain slice up to a depth of 80 μm. The system was shown to nearly recover the width and brightness of an AZ structure at a depth of 80 μm. Nevertheless, several systemic and specific limitations lead to the fact that the corrected rms wavefront error presented in literature [74, 70, 85] could not be reached.

Simultaneous *d*STORM and adaptive optics   The system was developed for single molecule localization using the *d*STORM technique. The reason for the lack of superresolution images in the results of this thesis are manifold: First, the TIRF mode needed to reach the high laser power to induce switching of the fluorophores is only possible at the surface of the sample, as the evanescent wave only penetrates about 100 nm into the sample. The energy density of epi-illumination for a reasonable field of view with the conventional lasers used was not high enough to induce photoswitching. This limitation can, however, be solved, as epi-illumination *d*STORM using flat-head beams has been reported. [87]

Adaptive optics feedback   Next, all correction steps were done by hand by translating the Zernike numbers from the WFS to the Zernike numbers on the DM, as described in Sections 2.2.3, 2.2.4, due to limitation in the proprietary software. The individual factors were derived by manually optimizing and evaluating PSF shapes by eye, a method highly prone to error. Furthermore, the factors are only valid for a given optical configuration, meaning that a readjustment in the emission path creates the necessity to derive a new set of numbers. A solution would be to custom program feedback loop. Many considerations and guides regarding the practical implementation of the control loop system are published [21, 69, 88, 14, 89]. Also, instead of relying on induced astigmatism to encode z-direction, the defocus aberration could be used directly to retrieve the z-localization on out of focus fluorophores. [75]

Hardware considerations   There exists a multitude of different WFS and DM commercially available, differing in the number of lenslets, the photon sensitivity of the camera, or the numbers of actuators, their stroke, etc., respectively. Other DM or WFS could possibly be more targeted towards the correction of specimen-induced aberrations.

Direct vs. indirect wavefront retrieval   Although many other investigators have successfully relied on active wavefront sensing, sensorless or image-based adaptive optics, as briefly mentioned in 1.5, increases image contrast by using a hill-climbing algorithm, although more sophisticated algorithms have been used [89]. This approach is less complex to implement, as no WFS and no feedback loop has to be implemented. Also, the metric is not the wavefront, but the image quality itself, possibly yielding better results. However, image-based approaches require more time for each frame until the algorithm converges, therefore stand-alone image-based wavefront correction is not suitable for switching-based SMLM techniques or fast real-time observations. [90, 91, 24] However, combined approaches are also possible, where the WFS gives very good starting parameters for the image-based algorithm, increasing the converging time drastically. [92]
Also combination of different DMs, either in series to accommodate high-stroke and low-stroke aberrations individually, comparable to a woofer-tweeter arrangement in speakers, or to correct different parts of the image plane, are envisioned to possibly yield higher rms Wavefront reduction. [93]

True 4f system   Despite the fact that the field lens was able to restore the telecentricity of the system, the placement of a lens which is manufacturer-optimized for telecentric placement in the image plane of the system is considered a workaround, not a solution. Building a proper $4f$ system by placing a tube lens further apart from the objective

outside the microscope body would render the field lens obsolete and is expected to reduce overall system aberrations, increase versatility and aid in adapting the system to life-science applications. [69]

All in all, one of the main goals of AO remains: To simplify the technique and develop more robust and versatile setups for life-science applications.

Bibliography

[1] J. W. Goodman. *Introduction to Fourier Optics*. 4th ed. 2017, p. 564. ISBN: 978-1-319-11916-4.

[2] A. Kurz. "Correlative live and fixed cell superresolution microscopy". PhD thesis. 2020.

[3] E. Hering and R. Martin. *Optik für Ingenieure und Naturwissenschaftler: Grundlagen und Anwendungen*. Carl Hanser Verlag GmbH & Company KG, 2017. ISBN: 9783446454521. URL: `https://www.hanser-e library.com/doi/book/10.3139/9783446445093`.

[4] J. A. Kubby, ed. *Adaptive Optics for Biological Imaging*. 1st ed. CRC Press, Apr. 2013, p. 388. ISBN: 978-1-4398-5018-3. DOI: `10.1201/b14898`.

[5] *Pupil Diameter and Beam Spot Diameter of Objective Lens*. Olympus. 2020. URL: `https://www.olympu s-ims.com/en/microscope/terms/luminous_flux/` (visited on 04/02/2020).

[6] *Piezoelectric Deformable Mirror (DMP40) Operation Manual*. Thorlabs GmbH. 2021.

[7] *Shack Hartman Wavefront Sensor Operation Manual*. Thorlabs GmbH. 2020.

[8] *Andor SONA Operation Manual*. Oxford Instruments. 2020.

[9] Ophthalmics. *Optical Aberrations of Eyes*. ANSI Z80.28. American National Standard Institute, 2017.

[10] Y. H. Hsieh et al. "Integral-based parallel algorithm for the fast generation of the Zernike polynomials". In: *Opt. Express* 28.2 (Jan. 2020), pp. 936–947. DOI: `10.1364/OE.380567`. URL: `http://www.opticsexpr ess.org/abstract.cfm?URI=oe-28-2-936`.

[11] V. Lakshminarayanan and A. Fleck. "Zernike polynomials: a guide". In: *Journal of Modern Optics* 58.18 (2011), pp. 1678–1678. DOI: `10.1080/09500340.2011.633763`.

[12] M. Booth et al. "Aberrations and adaptive optics in super-resolution microscopy". In: *Microscopy* 64.4 (June 2015), pp. 251–261. ISSN: 2050-5698. DOI: `10.1093/jmicro/dfv033`. URL: `http://oup.prod.sis.la n/jmicro/article-pdf/64/4/251/26556994/dfv033.pdf`.

[13] A. B. Vasista, D. K. Sharma and G. P. Kumar. "Fourier Plane Optical Microscopy and Spectroscopy". In: *digital Encyclopedia of Applied Physics*. American Cancer Society, 2019, pp. 1–14. ISBN: 9783527600434. DOI: `10.1002/3527600434.eap817`. URL: `https://onlinelibrary.wiley.com/doi/abs/10.1002 /3527600434.eap817`.

[14] D. Wilding et al. "Practical guidelines for implementing adaptive optics in fluorescence microscopy". In: 10502 (2018). Ed. by T. G. Bifano, J. Kubby and S. Gigan, pp. 92–103. DOI: `10.1117/12.2287647`.

[15] B. C. Platt and R. B. Shack. "History and principles of Shack-Hartmann wavefront sensing." In: *Journal of refractive surgery* 17 5 (2001), pp. 573–577.

[16] M. Downing et al. "Review of AO Wavefront Sensing Detectors". In: *unpublished* (Mar. 2016).

[17] R. P. Matital et al. "Review of holographic wavefront sensors". In: (Jan. 2018), pp. 535–538. DOI: `10.1109 /EIConRus.2018.8317153`.

[18] M. E. Khosroshahi. "Study of spatial thermal distribution of gold nanourchins in saline by combined transverse probe beam deflection and beam wavefront sensor: biomedical implications". In: *Applied Physics B* 125.12 (Nov. 2019), p. 229. ISSN: 1432-0649. DOI: `10.1007/s00340-019-7338-1`.

[19] V. J. Doherty and D. Shafer. "Simple Method Of Correcting The Aberrations Of A Beamsplitter In Converging Light". In: *1980 International Lens Design Conference*. Ed. by R. E. Fischer. Vol. 0237. International Society for Optics and Photonics. SPIE, 1980, pp. 195–201. DOI: `10.1117/12.959086`.

[20] J. Pawley, ed. *Handbook of Biological Confocal Microscopy*. 3rd ed. Springer US, 2006, pp. 212–213. ISBN: 978-0-387-45524-2. DOI: `10.1007/978-0-387-45524-2`. URL: `https://onlinelibrary.wiley.com /doi/abs/10.1002/sca.20059`.

[21] B. Dong and M. J. Booth. "Wavefront control in adaptive microscopy using Shack-Hartmann sensors with arbitrarily shaped pupils". In: *Opt. Express* 26.2 (Jan. 2018), pp. 1655–1669. DOI: `10.1364/OE.26.001655`. URL: `http://www.opticsexpress.org/abstract.cfm?URI=oe-26-2-1655`.

[22] C. Bourgenot et al. "Comparison of closed loop and sensorless adaptive optics in widefield optical microscopy". In: *Journal of the European Optical Society - Rapid publications* 8.0 (2013). URL: `https://www.jeos.org/index.php/jeos_rp/article/view/13027`.

[23] D. Burke et al. "Adaptive optics correction of specimen-induced aberrations in single-molecule switching microscopy". In: *Optica* 2.2 (Feb. 2015), pp. 177–185. DOI: `10.1364/OPTICA.2.000177`. URL: `http://www.osapublishing.org/optica/abstract.cfm?URI=optica-2-2-177`.

[24] N. Piro et al. "Improved 3D Superresolution Localization Microscopy Using Adaptive Optics". In: (Jan. 2014). URL: `https://arxiv.org/abs/1401.0879`.

[25] Z. Svindrych. Forum post, url not available any more.

[26] S. Ross. *Microscopy: Disassembling a Nikon Ti Eclipse*. Nikon. URL: `https://www.youtube.com/watch?v=DAV0X1c3s-g#t=30m59s` (visited on 30/12/2020).

[27] ISO/TC 172/SC 5 Microscopes and endoscopes. *Microscopes — Interfacing connection type C*. ISO 10935:2009. International Organization for Standardization, Aug. 2009.

[28] *Infinity Optical Systems*. Nikon Corporation. 2020. URL: `https://www.microscopyu.com/microscopy-basics/infinity-optical-systems` (visited on 04/02/2020).

[29] I. Khaw et al. "Flat-field illumination for quantitative fluorescence imaging". In: *Opt. Express* 26.12 (June 2018), pp. 15276–15288. DOI: `10.1364/OE.26.015276`. URL: `http://www.opticsexpress.org/abstract.cfm?URI=oe-26-12-15276`.

[30] A. Taddeucci et al. "Optical properties of brain tissue". In: *Journal of Biomedical Optics* 1.1 (1996), pp. 117–123. DOI: `10.1117/12.227816`.

[31] P. van der Zee, M. Essenpreis and D. T. Delpy. "Optical properties of brain tissue". In: 1888 (1993). Ed. by B. Chance and R. R. Alfano, pp. 454–465. DOI: `10.1117/12.154665`.

[32] S. C. Gebhart, W. C. Lin and A. Mahadevan-Jansen. "In vitrodetermination of normal and neoplastic human brain tissue optical properties using inverse adding-doubling". In: *Physics in Medicine and Biology* 51.8 (Mar. 2006), pp. 2011–2027. DOI: `10.1088/0031-9155/51/8/004`.

[33] S. Wieneke and C. Gerhard. "Tissue optics and laser–tissue interactions". In: *Lasers in Medical Diagnosis and Therapy*. 2053-2563. IOP Publishing, 2018, 3-1 to 3–42. ISBN: 978-0-7503-1275-2. DOI: `10.1088/978-0-7503-1275-2ch3`. URL: `http://dx.doi.org/10.1088/978-0-7503-1275-2ch3`.

[34] S. L. Jacques. "Optical properties of biological tissues: a review". In: *Physics in Medicine and Biology* 58.11 (May 2013), R37–R61. DOI: `10.1088/0031-9155/58/11/r37`.

[35] J. L. Sandell and T. C. Zhu. "A review of in-vivo optical properties of human tissues and its impact on PDT". In: *Journal of Biophotonics* 4.11-12 (2011), pp. 773–787. DOI: `10.1002/jbio.201100062`. URL: `https://onlinelibrary.wiley.com/doi/abs/10.1002/jbio.201100062`.

[36] A. N. Bashkatov et al. "Measurement of tissue optical properties in the context of tissue optical clearing". In: *Journal of Biomedical Optics* 23.9 (2018), pp. 1–31. DOI: `10.1117/1.JBO.23.9.091416`.

[37] A. N. Yaroslavsky et al. "Optical properties of selected native and coagulated human brain tissues in vitro in the visible and near infrared spectral range". In: *Physics in Medicine and Biology* 47.12 (June 2002), pp. 2059–2073. DOI: `10.1088/0031-9155/47/12/305`.

[38] E. A. Genina et al. "Optical properties of brain tissues at the different stages of glioma development in rats: pilot study". In: *Biomed. Opt. Express* 10.10 (Oct. 2019), pp. 5182–5197. DOI: `10.1364/BOE.10.005182`. URL: `http://www.osapublishing.org/boe/abstract.cfm?URI=boe-10-10-5182`.

[39] W. Gottschalk. "Ein Messverfahren zur Bestimmung der optischen Parameter biologischer Gewebe in vitro". German. Fak. f. Elektrotechnik, Diss. v. 15.12.1992. PhD thesis. 1992.

[40] T. Lister, P. A. Wright and P. H. Chappell. "Optical properties of human skin". In: *Journal of Biomedical Optics* 17.9 (2012), pp. 1–15. DOI: `10.1117/1.JBO.17.9.090901`.

[41] R. C. Smith and K. S. Baker. "Optical properties of the clearest natural waters (200–800 nm)". In: *Appl. Opt.* 20.2 (Jan. 1981), pp. 177–184. DOI: `10.1364/AO.20.000177`. URL: `http://ao.osa.org/abstract.cfm?URI=ao-20-2-177`.

[42] A. Santuy et al. "A Quantitative Study on the Distribution of Mitochondria in the Neuropil of the Juvenile Rat Somatosensory Cortex". In: *Cerebral Cortex* 28.10 (July 2018), pp. 3673–3684. ISSN: 1047-3211. DOI: `10.1093/cercor/bhy159`. URL: `https://academic.oup.com/cercor/article-pdf/28/10/3673/25714397/bhy159.pdf`.

[43] B. Beauvoit, T. Kitai and B. Chance. "Contribution of the mitochondrial compartment to the optical properties of the rat liver: a theoretical and practical approach". In: *Biophysical Journal* 67.6 (1994), pp. 2501–2510. ISSN: 0006-3495. DOI: 10.1016/S0006-3495(94)80740-4. URL: http://www.sciencedirect.com/science/article/pii/S0006349594807404.

[44] J. Emperador-Melero and P. S. Kaeser. "Assembly of the presynaptic active zone". In: *Current Opinion in Neurobiology* 63 (2020). Cellular Neuroscience, pp. 95–103. ISSN: 0959-4388. DOI: 10.1016/j.conb.2020.03.008. URL: http://www.sciencedirect.com/science/article/pii/S0959438820300714.

[45] N. Ehmann et al. "Quantitative super-resolution imaging of Bruchpilot distinguishes active zone states". In: *Nature Communications* 5.1 (Aug. 2014), p. 4650. ISSN: 2041-1723. DOI: 10.1038/ncomms5650.

[46] K. B. Gehring et al. "Age-associated increase of the active zone protein Bruchpilot within the honeybee mushroom body". In: *PLOS ONE* 12.4 (Apr. 2017), pp. 1–19. DOI: 10.1371/journal.pone.0175894.

[47] *Nikon Ti-E inverted Reseach Microscope Operation Manual*. Nikon. 2020.

[48] *Nikon Objectives*. Nikon Corporation. 2020. URL: https://www.microscope.healthcare.nikon.com/de_EU/selectors/objectives (visited on 10/06/2020).

[49] K. M. "Objective's back focal planes". Personal communication with Nikon sales manager for south germany. Wuerzburg, June 2020.

[50] *FocalCheck Microspheres*. ThermoFisher Scientific. 2020. URL: https://www.thermofisher.com/order/catalog/product/F14806#/F14806 (visited on 14/03/2020).

[51] *FluoSpheres Sulfate Microspheres*. ThermoFisher Scientific. 2020. URL: https://www.thermofisher.com/order/catalog/product/F8859#/F8859 (visited on 14/03/2020).

[52] *Crimson Carboxylate-Modified FluoSpheres*. ThermoFisher Scientific. 2020. URL: https://www.thermofisher.com/order/catalog/product/F8816#/F8816 (visited on 14/03/2020).

[53] *TetraSpeck Microspheres*. ThermoFisher Scientific. 2020. URL: https://www.thermofisher.com/order/catalog/product/T7279#/T7279 (visited on 14/03/2020).

[54] C. Gerhard and G. Adams. "Easy-to-use software tools for teaching the basics, design and applications of optical components and systems". In: *Education and Training in Optics and Photonics: ETOP 2015*. Vol. 9793. International Society for Optics and Photonics. SPIE, 2015, pp. 113–119. DOI: 10.1117/12.2223079.

[55] T. Thöniss, G. Adams and C. Gerhard. "Optical System Design Software Tools Cover Envelope Calculations to the Final Engineering Drawings". In: 2009. DOI: 10.1002/OPPH.201190022.

[56] *NIS-Elements*. Nikon. 2020. URL: https://www.nikon.com/products/microscope-solutions/lineup/img_soft/nis-elements/ (visited on 01/01/2021).

[57] *iBeam Smart*. Toptica Photonics. 2020. URL: https://www.toptica.com/products/single-mode-diode-lasers/ibeam-smart/ (visited on 01/01/2021).

[58] *Remote Laser Control*. Laser Quantum. 2020. URL: https://www.laserquantum.com/products/detail.cfm?id=60 (visited on 01/01/2021).

[59] *Deformable Mirror Software*. Thorlabs. 2020. URL: https://www.thorlabs.de/software_pages/ViewSoftwarePage.cfm?Code=DMP40 (visited on 01/01/2021).

[60] *Wavefront Sensor Software*. Thorlabs. 2020. URL: https://www.thorlabs.de/software_pages/ViewSoftwarePage.cfm?Code=WFS (visited on 01/01/2021).

[61] *Sublime Text 3*. Sublime HQ Pty Ltd. 2020. URL: https://www.sublimetext.com/3 (visited on 01/01/2021).

[62] T. Williams and C. Kelley. *Gnuplot 5.0*. 2020. URL: http://www.gnuplot.info/ (visited on 01/01/2021).

[63] J. Schindelin et al. "Fiji: an open-source platform for biological-image analysis". In: *Nature Methods* 9.7 (July 2012), pp. 676–682. ISSN: 1548-7105. DOI: 10.1038/nmeth.2019.

[64] S. Wolter et al. "rapidSTORM: accurate, fast open-source software for localization microscopy". In: *Nature Methods* 9.11 (Nov. 2012), pp. 1040–1041. ISSN: 1548-7105. DOI: 10.1038/nmeth.2224.

[65] [SW] Inkscape Project, *Inkscape* version 0.92.5, 16th Apr. 2020. URL: https://inkscape.org.

[66] F. Neubert. "Markierung postsynaptischer Proteine für die hochauflösende Fluoreszenzmikroskopie". deutsch. PhD thesis. 2019.

[67] A. Schwartz et al. "Quantitating fluorescence intensity from fluorophore: The definition of MESF assignment". In: *Journal of Research of the National Institute of Standards and Technology* 107.1 (Jan. 2002), p. 83. DOI: 10.6028/jres.107.009.

[68] M. J. Booth. "Adaptive optics in microscopy". In: *Philosophical Transactions of the Royal Society A: Mathematical, Physical and Engineering Sciences* 365.1861 (2007), pp. 2829–2843. DOI: 10.1098/rsta.2007.0013. URL: https://royalsocietypublishing.org/doi/abs/10.1098/rsta.2007.0013.

[69] K. M. Hampson et al. *Practical Implementation of Adaptive Optical Microscopes*. 2020. DOI: 10.5281/zenodo.4080673. URL: https://aomicroscopy.org/ (visited on 01/01/2021).

[70] O. Azucena et al. "Wavefront aberration measurements and corrections through thick tissue using fluorescent microsphere reference beacons". In: *Opt. Express* 18.16 (Aug. 2010), pp. 17521–17532. DOI: 10.1364/OE.18.017521. URL: http://www.opticsexpress.org/abstract.cfm?URI=oe-18-16-17521.

[71] Y. Dai et al. "Active compensation of extrinsic polarization errors using adaptive optics". In: *Opt. Express* 27.24 (Nov. 2019), pp. 35797–35810. DOI: 10.1364/OE.27.035797. URL: http://www.opticsexpress.org/abstract.cfm?URI=oe-27-24-35797.

[72] R. Foy and A. Labeyrie. "Feasibility of adaptive telescope with laser probe". In: *Astronomy and Astrophysics* 152.2 (Nov. 1985), pp. L29–L31. URL: https://ui.adsabs.harvard.edu/abs/1985A&A...152L..29F.

[73] R. W. Wilson. "SLODAR: measuring optical turbulence altitude with a Shack–Hartmann wavefront sensor". In: *Monthly Notices of the Royal Astronomical Society* 337.1 (Nov. 2002), pp. 103–108. ISSN: 0035-8711. DOI: 10.1046/j.1365-8711.2002.05847.x. URL: https://academic.oup.com/mnras/article-pdf/337/1/103/18162918/337-1-103.pdf.

[74] O. Azucena et al. "Implementation of adaptive optics in fluorescent microscopy using wavefront sensing and correction". In: *MEMS Adaptive Optics IV*. Ed. by S. S. Olivier, T. G. Bifano and J. A. Kubby. Vol. 7595. International Society for Optics and Photonics. SPIE, Feb. 2010, pp. 131–139. DOI: 10.1117/12.846380.

[75] P. Kner et al. "High-resolution wide-field microscopy with adaptive optics for spherical aberration correction and motionless focusing". In: *Journal of Microscopy* 237.2 (2010), pp. 136–147. DOI: 10.1111/j.1365-2818.2009.03315.x. URL: https://onlinelibrary.wiley.com/doi/abs/10.1111/j.1365-2818.2009.03315.x.

[76] M. J. Mlodzianoski et al. "Active PSF shaping and adaptive optics enable volumetric localization microscopy through brain sections". In: *Nature Methods* 15.8 (2018), pp. 583–586. ISSN: 1548-7105. DOI: 10.1038/s41592-018-0053-8.

[77] X. Tao et al. "Adaptive optics confocal microscopy using direct wavefront sensing". In: *Opt. Lett.* 36.7 (Apr. 2011), pp. 1062–1064. DOI: 10.1364/OL.36.001062. URL: http://ol.osa.org/abstract.cfm?URI=ol-36-7-1062.

[78] O. Azucena et al. "Adaptive optics wide-field microscopy using direct wavefront sensing". In: *Opt. Lett.* 36.6 (Mar. 2011), pp. 825–827. DOI: 10.1364/OL.36.000825. URL: http://ol.osa.org/abstract.cfm?URI=ol-36-6-825.

[79] *Alexa 647*. ThermoFisher Scientific. 2020. URL: https://www.thermofisher.com/de/en/home/life-science/cell-analysis/fluorophores/alexa-fluor-647.html (visited on 09/06/2020).

[80] *T 640 LPXR dichroic filter*. Chroma Technology Corp. 2020. URL: https://www.ahf.de/en/products/spectral-analysis-photonic/optical-filters/dichroic-beamsplitters/beamsplitters-for-epi-fluorescence/standard-beamsplitters/longpass-beamsplitters/2536/beamsplitter-t-640-lpxr (visited on 09/06/2020).

[81] *gem 640*. Laser Quantum. 2020. URL: https://www.laserquantum.com/products/detail.cfm?id=135 (visited on 09/06/2020).

[82] M. J. Booth. "Adaptive optical microscopy: the ongoing quest for a perfect image". In: *Light: Science &Amp; Applications* 3 (Apr. 2014). Review, p. 165. DOI: 10.1038/lsa.2014.46.

[83] M. Siemons et al. "Comparing strategies for deep astigmatism-based single-molecule localization microscopy". In: *Biomed. Opt. Express* 11.2 (Feb. 2020), pp. 735–751. DOI: 10.1364/BOE.382023. URL: http://www.osapublishing.org/boe/abstract.cfm?URI=boe-11-2-735.

[84] R. W. and G. C. "Plasticity of Synaptic Microcircuits in the Mushroom-Body Calyx of the Honey Bee." In: *Honeybee Neurobiology and Behavior*. Ed. by G. C., E. D. and G. M., pp. 141–153. ISBN: 978-94-007-2098-5. DOI: 10.1007/978-94-007-2099-2_12.

[85] X. Tao et al. "Adaptive optical two-photon microscopy using autofluorescent guide stars". In: *Opt. Lett.* 38.23 (Dec. 2013), pp. 5075–5078. DOI: 10.1364/OL.38.005075. URL: http://ol.osa.org/abstract.cfm?URI=ol-38-23-5075.

[86] W. Zheng et al. "Adaptive optics improves multiphoton super-resolution imaging". In: *Nature Methods* 14 (June 2017), p. 869. DOI: 10.1038/nmeth.4337.

[87] C. J. Rowlands et al. "Flat-Field Super-Resolution Localization Microscopy with a Low-Cost Refractive Beam-Shaping Element". In: *Scientific Reports* 8.1 (Apr. 2018), p. 5630. ISSN: 2045-2322. DOI: `10.1038/s41598-018-24052-4`.

[88] N. Hall et al. "Microscope-AOtools: a generalised adaptive optics implementation". In: *Opt. Express* 28.20 (Sept. 2020), pp. 28987–29003. DOI: `10.1364/OE.401117`. URL: `http://www.opticsexpress.org/abstract.cfm?URI=oe-28-20-28987`.

[89] L. Sherman et al. "Adaptive correction of depth-induced aberrations in multiphoton scanning microscopy using a deformable mirror". In: *Journal of Microscopy* 206.1 (2002), pp. 65–71. DOI: `10.1046/j.1365-2818.2002.01004.x`. URL: `https://onlinelibrary.wiley.com/doi/abs/10.1046/j.1365-2818.2002.01004.x`.

[90] D. Champelovier et al. "Image-based adaptive optics for in vivo imaging in the hippocampus". In: *Scientific Reports* 7.1 (Feb. 2017), p. 42924. ISSN: 2045-2322. DOI: `10.1038/srep42924`.

[91] N. Ji. "Adaptive optical fluorescence microscopy". In: *Nature Methods* 14.4 (Apr. 2017), pp. 374–380. ISSN: 1548-7105. DOI: `10.1038/nmeth.4218`.

[92] C. Wu et al. "Hybrid wavefront sensing and image correction algorithm for imaging through turbulent media". In: *Laser Communication and Propagation through the Atmosphere and Oceans VI*. Ed. by J. P. Bos, A. M. J. van Eijk and S. M. Hammel. Vol. 10408. International Society for Optics and Photonics. SPIE, 2017, pp. 256–265. DOI: `10.1117/12.2275735`.

[93] Z. Kam et al. "Modelling the application of adaptive optics to wide-field microscope live imaging". In: *Journal of Microscopy* 226.1 (2007), pp. 33–42. DOI: `10.1111/j.1365-2818.2007.01751.x`.